

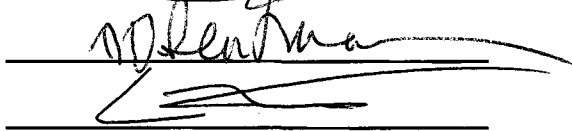
NEURAL NETWORK APPROACH TO
CLASSIFICATION OF INFRASOUND SIGNALS

BY

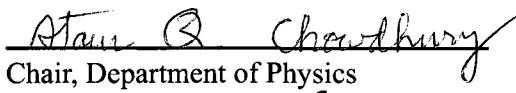
Dong-Chang Lee

RECOMMENDED:



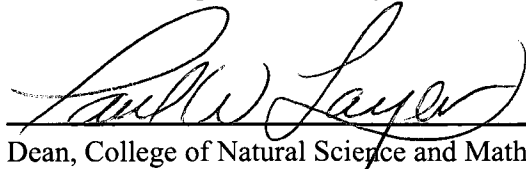


Advisory Committee Chair



Chair, Department of Physics

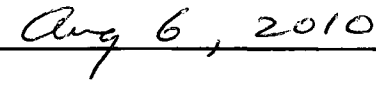
APPROVED:



Dean, College of Natural Science and Mathematics



Dean of the Graduate School



Date

**NEURAL NETWORK APPROACH TO CLASSIFICATION OF
INFRASOUND SIGNALS**

A
THESIS

Presented to the Faculty
of the University of Alaska Fairbanks
in Partial Fulfillment of the Requirements
for the Degree of

DOCTOR OF PHILOSOPHY

By
Dong-Chang Lee, B.Sc., M.Sc.

Fairbanks, Alaska

August 2010

UMI Number: 3436651

All rights reserved

INFORMATION TO ALL USERS

The quality of this reproduction is dependent upon the quality of the copy submitted.

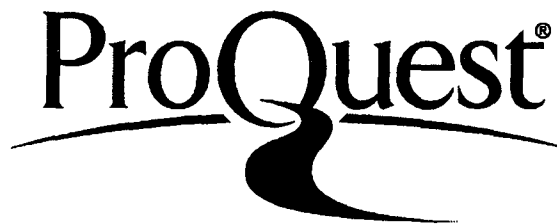
In the unlikely event that the author did not send a complete manuscript and there are missing pages, these will be noted. Also, if material had to be removed, a note will indicate the deletion.



UMI 3436651

Copyright 2011 by ProQuest LLC.

All rights reserved. This edition of the work is protected against unauthorized copying under Title 17, United States Code.



ProQuest LLC
789 East Eisenhower Parkway
P.O. Box 1346
Ann Arbor, MI 48106-1346

Abstract

As part of the International Monitoring Systems of the Preparatory Commissions for the Comprehensive Nuclear-Test-Ban Treaty Organization, the Infrasound Group at the University of Alaska Fairbanks maintains and operates two infrasound stations to monitor global nuclear activity. In addition, the group specializes in detecting and classifying the man-made and naturally produced signals recorded at both stations by computing various characterization parameters (e.g. mean of the cross correlation maxima, trace velocity, direction of arrival, and planarity values) using the in-house developed weighted least-squares algorithm.

Classifying commonly observed low-frequency (0.015-0.1 Hz) signals at our stations, namely mountain associated waves and high trace-velocity signals, using a traditional approach (e.g. analysis of power spectral density) presents a problem. Such signals can be separated statistically by setting a window to estimate the trace velocity for each signal type. The feasibility of such a technique is demonstrated by studying and comparing various summary plots (e.g. universal time, seasonal and azimuthal variations) that are produced by analyzing the Fairbanks and Antarctic data (2004-2007). Such plots with the availability of magnetic activity information (from the College International Geophysical Observatory located at Fairbanks, Alaska) leads to identification of possible physical sources of the two signal types. Throughout this thesis a newly-developed, robust algorithm (sum of squares of variance ratios) with improved detection quality (under low signal to noise ratios) over two well-known detection algorithms (mean of the cross correlation maxima and Fisher Statistics) is investigated for its efficacy as a new detector.

A neural network is examined for its ability to automatically classify the two signals described above against clutter (spurious signals with common characteristics). Four identical perceptron networks are trained and validated (with >92% classification rates) using eight independent datasets; each dataset consists of three-element (each element being a characterization parameter) feature vectors. The validated networks are tested against an expert, Prof. Charles R. Wilson, who has been studying those signals for decades. From the

graphical comparisons, we conclude that such networks are excellent candidate for substituting for the expert. Advantages to such networks include robustness and resistance to errors, and the bias of a human operator.

Table of Contents

Signature Page	i
Title Page	ii
Abstract	iii
Table of Contents	v
List of Figures	vii
List of Tables	x
Acknowledgements	xi
1 Introduction	1
1.1 Abstract	1
1.2 Thesis Organization	2
1.3 Sound	4
1.4 Wave Equation	6
1.5 Instrumentation	16
1.6 Estimation of Parameters	19
1.7 High Trace Velocity Signals	24
2 Signal Review	27
2.1 Abstract	27
2.2 High Frequency Signals	28
2.3 Microbaroms	29
2.4 Low Frequency Signals	38
2.4.1 Mountain Associated Waves	38
2.4.2 High Trace Velocity Signals	42
2.5 Summary	48
3 Analysis of Infrasound Data	53
3.1 Abstract	53
3.2 Detector Statistics: MCCM, F-stat, SSVR1, and SSVR2	54
3.3 Fairbanks Array	64

3.4	Antarctic Array	79
3.5	Summary	88
4	Neural Networks	93
4.1	Overview	93
4.2	Perceptron vs. Perceptron Network	95
4.3	Training and Validation of perceptron networks using Infrasound Data . . .	107
4.4	Summary	110
5	Neural Networks: Comparison	114
5.1	Abstract	114
5.2	Comparison of Perceptron Network Classification against Human Expert Classification	114
5.3	Summary	129
6	Conclusions	130
6.1	Summary	130
6.2	Future Directions	132
	Bibliography	134

List of Figures

1.1 Measured and modelled atmospheric profiles at Fairbanks, Alaska.	11
1.2 Atmospheric absorption rates (dB/Km) of a harmonic wave.	12
1.3 (a) Ray tracings and (b) corresponding sound pressure levels.	15
1.4 Fairbanks array (I53US) configuration.	17
1.5 Noise reducing pipe configuration at I53US.	18
1.6 Uncertainty in trace velocity (V_t) estimation for I53US.	23
1.7 Uncertainty in azimuth (θ) estimation for I53US.	25
2.1 Example of mine blasts observed at I53US on February 24, 2007.	30
2.2 PSD of the mine blasts (in Fig. 2.1).	31
2.3 Example of microbaroms observed at I53US on September 25, 2006.	33
2.4 PSD of the microbaroms (in Fig. 2.3).	34
2.5 Detection summary plot of microbaroms on September 25, 2006 at I53US.	36
2.6 (a) V_t and (b) θ histograms of microbaroms detected at I53US.	37
2.7 Azimuth-trace velocity diagram for MAWs observed at I53US and I55US.	40
2.8 Example of MAWs observed at I53US on November 22, 2006.	41
2.9 PSD of the MAWs (in Fig. 2.8).	43
2.10 Detection summary plot of MAWs at I53US on November 22, 2006.	44
2.11 Example of HTVs observed at I53US on August 19, 2006.	46
2.12 PSD of the HTVs (in Fig. 2.11).	47
2.13 Detection summary plot of HTVs at I53US on August 19, 2006.	49
2.14 Magnetic disturbances recorded at the CIGO on August 19, 2006.	50
3.1 ROC analysis of the mine blasts against the Gaussian white noise.	56
3.2 ROC analysis of the microbaroms against the Gaussian white noise.	57
3.3 ROC analysis of the MAWs against the Gaussian white noise.	58
3.4 ROC analysis of the mine blasts against the pink noise.	60
3.5 ROC analysis of the microbaroms against the pink noise.	61

3.6	ROC analysis of the MAWs against the pink noise.	62
3.7	Robustness of the SSVR2 detector against the MCCM detector.	63
3.8	Histograms of characterization parameters for the Gaussian and pink noise.	65
3.9	Histograms of characterization parameters at I53US (2004-2007).	67
3.10	Variational plots of low-frequency signals detected at I53US.	69
3.11	θ histograms of the MAW and HTV activity at I53US (2004-2007).	70
3.12	θ histograms of the MAW and HTV activity at I53US (2007).	72
3.13	UT variations of the MAW and HTV activity I53US (2004-2007).	73
3.14	Variations of magnetic activity from CIGO as a function of UT.	75
3.15	Quarterly θ histograms of the MAW and HTV activity at I53US.	76
3.16	Quarterly UT variations of the MAW and HTV activity at I53US.	77
3.17	Quarterly UT variations of changes in magnetic activity from CIGO.	78
3.18	Histograms of characterization parameters at I55US (2004-2007).	81
3.19	Variational plots of low-frequency signals detected at I55US.	82
3.20	θ histograms of the MAW and HTV activity at I55US (2004-2007).	84
3.21	θ histograms of the MAW and HTV activity at I55US (2007).	85
3.22	UT variations of the MAW and HTV activity at I55US (2004-2007).	86
3.23	Quarterly θ histograms of the MAW and HTV activity at I55US.	87
3.24	Quarterly UT variations of the MAW and HTV activity at I55US.	89
4.1	Cartoon of a biological neuron.	97
4.2	Neural network flow chart.	99
4.3	A perceptron structure.	101
4.4	A perceptron network.	105
4.5	Graphical representation of XOR function.	106
4.6	Performance error plots of four trained perceptron networks	109
4.7	Decision boundaries of the MCCM-based network for I53US.	111
4.8	Decision boundaries of the SSVR2-based network for I53US.	112

5.1	MAW detection using MCCM- and SSVR2-based networks (case 1).	116
5.2	MAW detection using MCCM- and SSVR2-based networks (case 2).	117
5.3	MAW detection using MCCM- and SSVR2-based networks (case 3).	118
5.4	MAW detection using MCCM- and SSVR2-based networks (case 4).	119
5.5	MAW detection using MCCM- and SSVR2-based networks (case 5).	120
5.6	MAW detection using MCCM- and SSVR2-based networks (case 6).	121
5.7	MAW detection using MCCM- and SSVR2-based networks (case 7).	122
5.8	HTV detection using MCCM- and SSVR2-based networks (case 1).	123
5.9	HTV detection using MCCM- and SSVR2-based networks (case 2).	124
5.10	HTV detection using MCCM- and SSVR2-based networks (case 3).	125
5.11	HTV detection using MCCM- and SSVR2-based networks (case 4).	126
5.12	HTV detection using MCCM- and SSVR2-based networks (case 5).	127
5.13	HTV detection using MCCM- and SSVR2-based networks (case 6).	128

List of Tables

3.1	Parameter selection criteria for the MAWs, HTVs and clutter at I53US. . . .	66
3.2	Parameter selection criteria for the MAWs, HTVs and clutter at I55US. . . .	80
4.1	Performance summary of the perceptron networks for I53US.	108
4.2	Performance summary of the perceptron networks for I55US.	108

Acknowledgements

I am supremely grateful to my supervisors, Prof. Curt A. L. Szuberla and Prof. John V. Olson for their unflagging support, thoughtful encouragement, and discerning counsel throughout my doctoral study at the University of Alaska Fairbanks. Their sense of humor, perpetual energy and enthusiasm in research motivated everyone in our group and made the environment very comfortable and exciting place to work. In addition, they were very generous, kind, accessible and always willing to help.

My committee members Prof. Dave D. Sentman and Prof. Bill Bristow deserve special thanks for their indispensable guidance and continuous support. In particular, I sincerely enjoyed interacting with Prof. Sentman outside as well as inside the classroom. His intellectual curiosity, wisdom, and keen knowledge of life have inspired me to be more optimistic.

I am indebted to Dr. Kenneth Arnoult for his friendship, generosity and help during the past six years. He taught me the basics of investment for retirement, and I genuinely miss the time spent in such discussions. My graduate experience would not have been the same without him. Furthermore, I would like to thank Prof. Charles R. Wilson, Prof. John Craven and members of the Infrasound group for their useful discussion and support. I am particularly fortunate to have taken electrodynamics and classical mechanics from Prof. Channon Price. Although I had suffered from his courses, they were truly rewarding experiences in the end. Thank you.

I owe my deepest gratitude to my family for their endless love and support throughout my life; this dissertation simply would not been possible without them. I am indebted to my father, Kyung-Woo Lee, for his love and care. He worked extremely hard to support the family and devoted his life to provide me with the best possible education. He influenced me in every aspect of my life and inspired me to believe that nothing is impossible. It is his vision that brought me here, and I give him all the credits for my success and accomplishments. He, of course, could not have done this by himself- my mother, Young-Hee Yoon was beside him every step of the way. She has sacrificed so much for the family,

and I thank her for the everlasting love given to me. She is simply a perfect and truly caring person. I remember many sleepless nights she spent with me during midterms, but I especially miss her delicious dishes! I am proud of my sister, Dong-Gum Lee, for her enthusiasm in life. She gave me countless times of laughter, and cheered me up when I was going through difficult times. I love you.

Lastly, I am immensely grateful to all those who have supported me in all the many and varied respects as I strove to complete my doctoral study at the University of Alaska Fairbanks. Thank you all.

"Outstanding people have one thing in common: an absolute sense of mission."

—Zig Ziglar

"Our greatest happiness does not depend on the condition of life in which chance has placed us, but is always the result of a good conscience, good health, occupation, and freedom in all just pursuits."

—Thomas Jefferson

"If money is your hope for independence you will never have it. The only real security that a man will have in this world is a reserve of knowledge, experience, and ability."

—Henry Ford

"Keep your eyes wide open before marriage, half shut afterwards."

—Benjamin Franklin

Chapter 1

Introduction

1.1 Abstract

The Preparatory Commission for the Comprehensive Nuclear-Test-Ban Treaty Organization (CTBTO), an international organization established on 19 November 1996, monitors for nuclear weapons testing, and encourages the disarmament of nuclear weapons. It monitors global nuclear activity by overseeing 321 stations of the International Monitoring System (IMS) that are located throughout the world with four different technologies: seismic, infrasound, hydroacoustic, and radionuclide [1, 2, 3]. A network of 16 radionuclide laboratories also supports the IMS. Each of these stations sends data continuously to the International Data Center (IDC) in Vienna, where these data are analyzed and are made available to countries who have signed the treaty. The IMS is designed to record shock waves generated by nuclear explosions in the air, in the water, and ground. By deploying four different technologies, the CTBTO can reduce the risk of missing nuclear events, decrease false alarms, and therefore, improve the detection and the verification of nuclear activity. There are 55 certified IMS infrasonic stations operating around the world, and the Infrasound Group at the Geophysical Institute of the University of Alaska Fairbanks, operates and maintains two stations; one is located in Fairbanks, Alaska (I53US); the other is positioned at Windless Bight, Antarctica (I55US). Each array consists of eight microphones, developed by Chaparral Physics. A more detailed description of the instruments is given in a later section of this chapter. The Infrasound Group [4] has installed and operated seven different infrasonic arrays in different countries (Alaska, Canada, Sweden, and Antarctica) since 1965. Since then the group has been observing and studying both man-made and naturally produced infrasound signals. One of the tasks of the group is to detect and characterize infrasound signals from the background noise. We have identified the sources of several types of infrasound signals with the help of the ground truth when available.

Identified infrasound signals include mine blasts, aircraft, bolides, microbaroms, moun-

tain associated waves (MAWs), high trace velocity signals (HTVs), auroral infrasound, volcanic eruptions, earthquakes, and landslides, to name a few [5]. These signal types will be described in more detail later. In order to help characterize the signals, several parameters are estimated from the data, including: a weighted least squares algorithm for trace velocity V_t , azimuth θ , and planarity σ_τ and a detection scheme based on the mean of the cross correlation maxima (MCCM). Our group uses those parameters exclusively (with ground truth information when available) to identify the possible sources of infrasound signals detected at our stations (I53US and I55US).

In the atmosphere, a travelling sound wave loses energy by dissipative processes (atmospheric absorption) which depend on the frequency of the sound wave and on temperature, pressure, and humidity. As the frequency of the sound wave increases, the amplitude attenuation of the sound wave with distance also increases. Infrasound, being acoustic waves of the lowest propagating frequencies, can travel long distances with little attenuation, and that allows detection and identification of a distant source signal [6]. The effects of atmospheric absorption on travelling sound waves is discussed in a later section of this chapter.

This dissertation tries to answer basic two questions that are of interest to the infrasound community. Can two common signal types with similar properties, namely mountain associated waves and high trace velocity signals, be separated statistically? Can a neural network be used to automate classification of these signals among clutter (spurious signals with common characteristics)?

1.2 Thesis Organization

In Chapter 1, background information is discussed, such as properties of sound, atmospheric absorption, and the wave equation. Various characterization parameters (MCCM, V_t , θ , and σ_τ) including definitions and derivations are introduced here. This thesis exclusively relies on these parameters to detect and identify infrasound signals. The lower and upper trace velocity limits for ground source signals and the HTVs are determined using

a ray tracing model.

In Chapter 2, we introduce examples of infrasound signals detected at the Fairbanks array (I53US). They are divided into three different frequency groups: low-frequency signals (0.015-0.1 Hz), microbaroms (0.1-0.5 Hz), and high-frequency signals (0.5-10 Hz). We show their waveforms, power spectral densities, and characterization parameters: MCCM, V_t , θ , and σ_τ . The low-frequency signals are largely divided into two groups: MAWs are produced by the interaction of tropospheric wind flow and mountain ranges; HTVs are based on non-ground sources and that have trace velocity greater than 650 m/s. The high-frequency signals include mine blasts.

In Chapter 3, we turn our focus to a statistical study of the low-frequency infrasound signals from the both the Fairbanks and Antarctic arrays. We discuss an empirical comparison of four detection algorithms: the mean of the cross correlation maxima, the Fisher Statistic (F-stat), the sum of the squares of variance ratios (SSVR1 and SSVR2). We then determine the parameters that define MAWs, HTVs, and clutter based on a statistical study. The MAWs are compared with the HTVs by azimuthal, UT, and seasonal variations. We also use magnetometer data from College International Geophysical Observatory (CIGO) to show a similarity between HTVs and magnetic disturbances in the atmosphere.

In Chapter 4, a neural network is used to classify three types of low-frequency signals: MAWs, HTVs, and clutter. We begin by introducing the basic structure and mathematical properties of a perceptron. An exclusive OR (XOR) example is used to illustrate the limitation of the perceptron, and a more powerful perceptron network is introduced. We use four different data sets to train and validate the four perceptron networks: the MCCM- and SSVR2-based networks for the Fairbanks and Antarctic arrays.

In Chapter 5, the trained networks are tested against an expert, Prof. Charles R. Wilson, who has been studying the MAWs and HTVs for decades. He selected seven days with high MAW activity and six days with high HTV activity from the 2008 Fairbanks data. These data sets were never exposed to our networks for training. We then use modified detection summary plots to show expert-identified MAWs and HTVs, and they are com-

pared with the outputs of the MCCM- and SSVR2-based perceptron networks to illustrate the effectiveness of the trained neural networks.

In Chapter 6, we summarize our findings. These include the possible sources of MAWs and HTVs, the advantage of the SSVR2 detection method, and the feasibility of the perceptron networks to perform our classification problem. Finally, we present the significance of this research and suggest possible future directions.

1.3 Sound

Sound is a compression wave that travels through a medium (solid, liquid, or gas). Human hearing is capable of detecting only a limited range of frequencies, so sounds are commonly divided into three groups based on the frequency range: infrasound (0.001-16 Hz), audible (16 Hz-20 kHz), ultrasound (above 20 kHz). The lower and the upper limits of audibility vary depending on the person [7]. People have been studying sound for centuries, but the field of acoustics was not widely accepted by scientific communities until Rayleigh and Reynolds [8] used ray concepts to explain acoustic phenomena in the nineteenth century. Rayleigh and Stokes [9] extensively studied the sound generated by the vibrating strings and organ pipes in the nineteenth century, and they laid the foundation of the field of acoustics.

The Earth's atmosphere has following properties: it is roughly composed of nitrogen (78%), oxygen (21%), argon (1%), and carbon dioxide (0.1%); at sea level, the density of dry air at 20 °C is approximately 1.2 Kg/m³; the sound speed in dry air at 0 °C is roughly 331 m/s. The sound speed is also called the adiabatic speed because sound propagates in the atmosphere with a negligible heat flow [10]. In a stable atmosphere, the sound speed depends only on temperature and humidity of the air. The sound speed tends to increase with the rise in humidity level of the air; however, the correction is usually less than 1.5% [8].

In a liquid or gas, sound waves are longitudinal waves, that travel through a medium with periodic compressions and rarefactions that are in the same direction as the direction

of propagation. A sound wave is characterized by frequency, f , wavelength λ , and amplitude, A . The amplitude of a harmonic wave travelling in the x -direction at time t and position x can be written as,

$$A(x, t) = A_m \cos(kx - \omega t), \quad (1.1)$$

where ω is the angular frequency ($\omega = 2\pi f$), k is the wave number ($k = 2\pi/\lambda$), t is the time in seconds. In acoustics, the amplitude, A_m , is the maximum pressure of the wave, and it is measured in Pa. We can construct any wave form by superimposing a sufficient number of simple harmonic waves with carefully chosen frequencies and amplitudes. This is a basic idea of the Fourier Series, and there are some conditions that have to be met before the Fourier Series representation of an actual wave can exist: the wave has finite number of discontinuities, maxima, and minima in any period; the wave is absolutely integrable in any period [11].

A sound wave carries acoustic energy, including both kinetic and potential energy. The acoustic energy moves at the sound speed in the direction of the wave propagation. The kinetic and potential energies are of equal amplitude for a plane wave [8, 12]. For a harmonic point source in a homogeneous medium, the pressure and the velocity of the sound wave at position \vec{r} and time t can be written as,

$$p(\vec{r}, t) = \text{Re}((p_c)e^{-i\omega t}), \quad (1.2)$$

$$\vec{v}(\vec{r}, t) = \text{Re}((\vec{v}_c)e^{-i\omega t}), \quad (1.3)$$

where $\text{Re}(z)$ is the real part of the complex number z , and p_c and \vec{v}_c are complex pressure and velocity amplitudes, respectively. The complex pressure p_c is the solution to radial component of the wave equation (Eq. 1.15) in spherical coordinates. It is given by

$$p_c(\vec{r}) = S \left(\frac{e^{ikr}}{r} \right), \quad (1.4)$$

where S is a constant. As the wave moves away from the source, the amplitude of complex pressure p_c decreases as $1/r$ (Eq. 1.2). The acoustic intensity of the source is defined as $\vec{I} = p\vec{v}$ and it is a function of time. By writing p_c and \vec{v}_c in terms of real and imaginary parts, the

time-averaged intensity over a harmonic period of the wave, \bar{I}_{avg} can be written as,

$$\bar{I}_{avg} = \frac{1}{2}(p_c^* \bar{v}_c), \quad (1.5)$$

where the superscript asterisk is a complex conjugate. The acoustic power of the source is obtained by integrating the acoustic intensity over an arbitrary surface that encloses the source. For example, the time averaged acoustical power W_{avg} of a point source in a homogeneous medium is obtained by

$$W_{avg} = \int_A \bar{I}_{avg} \cdot \bar{n} dA, \quad (1.6)$$

where \bar{I}_{avg} is the time-averaged intensity of the source, A is the arbitrary surface that encloses the source and \bar{n} is the unit normal vector directed outward at the surface.

Although we can measure pressure amplitude in terms of Pa, it is customary to use the sound pressure level to report the quantity in decibels (dB). The sound pressure level, L_p , is defined by [8],

$$L_p = 10 \log_{10} \frac{(p_s^2)_{avg}}{p_{ref}^2}, \quad (1.7)$$

where $(p_s^2)_{avg}$ is the time average of the squared sound pressure p_s ; p_{ref} is commonly the threshold of human hearing and is usually taken as 2×10^{-5} Pa. For a harmonic sound wave, the time average of the squared pressure over a single period is given by $(p_s^2)_{avg} = |p_c|^2/2$. For example, a jack hammer at one meter away from an observer produces 2 Pa, equivalent to 100 dB; a television set at one meter away from the observer produces 0.02 Pa, equivalent to 60 dB; the threshold of pain for human ear is roughly 63.25 Pa, equivalent to 130 dB. An increase of the sound pressure level by 10 dB corresponds to an increase of $(p_s^2)_{avg}$ by a factor of ten.

1.4 Wave Equation

In the previous section, we discussed the properties and characteristics of sound. In this section we focus on the propagation of a sound wave in the atmosphere. The wave equation and sound speed are derived using the standard linearisation of the continuity and

momentum equations, followed by the effect of atmospheric absorption. Then, a ray-tracing model is used to describe the wave propagation paths of the sound in a stable atmosphere.

We, first, start with two well-known fluid equations to obtain the wave equation: the conservation of mass and the conservation of momentum [13]. The former is also known as the continuity equation where it (without the thermal diffusion and source terms) can be written as

$$\frac{\partial \rho}{\partial t} + \nabla \cdot (\rho \vec{v}) = 0, \quad (1.8)$$

where ρ and \vec{v} are density and velocity of the air. For a gas, the forces exerted by the particle's immediate neighbor overwhelm other types of forces (such as gravity, Coriolis, shear, etc). With that in mind, we can write the momentum equation as,

$$\rho \frac{D\vec{v}}{Dt} = -\nabla p, \quad (1.9)$$

where $D/Dt \equiv (\partial/\partial t + \vec{v} \cdot \nabla)$. For acoustic waves, perturbations in pressure and density are very small compared to average pressure and density of the atmosphere. Assuming the atmosphere is windless and homogeneous, the pressure, density, and wind speed of the atmosphere can be written as

$$p_a = p_{avg} + p, \quad (1.10)$$

$$\rho_a = \rho_{avg} + \rho, \quad (1.11)$$

$$\vec{v}_a = \vec{v}, \quad (1.12)$$

where p_{avg} and ρ_{avg} are the time-averaged pressure and density of the atmosphere. Substituting Eq. 1.12 into Eqs. 1.8 and 1.9, and retaining only linear terms, we obtain

$$\frac{\partial \rho}{\partial t} + \rho_{avg} (\nabla \cdot \vec{v}) = 0, \quad (1.13)$$

$$\rho_{avg} \frac{\partial \vec{v}}{\partial t} = -\nabla p. \quad (1.14)$$

Combining Eq. 1.14 with the relation $p = c^2 \rho$, we finally obtain the wave equation as

$$\nabla^2 p - \frac{1}{c^2} \frac{\partial^2 p}{\partial t^2} = 0, \quad (1.15)$$

where c is the sound speed.

As described above, travelling sound wave in a medium undergoes periodic compressions and rarefactions, but such motions are so rapid that we can simply ignore heat transfer between air molecules in the medium. Such an approximation is known as the adiabatic approximation, and it yields the equation of state, which allows us to write the pressure in terms of the density

$$p_a = K\rho_a^\gamma, \quad (1.16)$$

where K is a constant, $\gamma = c_p/c_v$ is the specific heat ratio, c_p and c_v are the specific heat of air at constant pressure and constant volume, respectively. Writing the pressure and density of the atmosphere in terms of their average values, and applying the first-order Taylor approximation to expand the pressure about the average pressure value, we obtain the relation,

$$p_a(\rho_a + \rho) = p_{avg} + \left(\frac{\partial p_a}{\partial \rho_a}\right)_{avg}\rho, \quad (1.17)$$

where the derivative is evaluated at $\rho_a = \rho_{avg}$. Using Eq. 1.16 and $p_a = p_{avg} + p$, we find

$$c^2 \equiv \left(\frac{\partial p_a}{\partial \rho_a}\right)_{avg} = \gamma \frac{p_{avg}}{\rho_{avg}}. \quad (1.18)$$

From the ideal gas law, $p_{avg} = \rho_{avg}RT$, we obtain the expression for sound speed as

$$c = \sqrt{\gamma RT}, \quad (1.19)$$

where $\gamma \simeq 1.4$ for dry air, $R = 287$ J/kg/K, and T is the temperature in K.

Three well-known physical processes are responsible for the energy loss of a travelling sound wave in the atmosphere [10, 12]: thermal conduction, viscosity of air, and relaxation losses of oxygen and nitrogen molecules in air. As mentioned before, the former (heat transfer) plays negligible role in the energy loss of the travelling wave, however; the other two terms play significant role in that of the travelling wave. Heat is produced as a result of all three processes, and the energy loss is larger at higher frequencies of the travelling wave. There are three physical profiles used to describe the Earth's atmosphere: temperature, pressure, and relative humidity. Such profiles are closely related to the three physical

processes described above. For air, viscosity and thermal conduction are proportional to $T^{3/2}/(T + 110)$ and $T^{3/2}/(245.4e^{-27.6/T})$, where T is temperature of air in K. Primary cause of the relaxation losses occur when O_2 and N_2 molecules collides with H_2O molecules, and so the relative amount of water molecule in air plays important role in determining the amount of energy loss by the relaxation process. As the temperature increases, the relative humidity decreases in the absent of pressure change, and the resulting relaxation losses are decreased. If the pressure gets larger then the relative humidity also increases in the absent of temperature change, and the resulting relaxation losses are increased. Evidently, the viscosity and thermal conduction increase as the pressure increases while the temperature remains constant. The relaxation losses also increases with increasing pressure. It is complicated to compute energy loss of the travelling wave, as the three physical processes are function of the temperature, pressure, and relative humidity.

As described above, the absorption of the sound wave depends on three atmospheric parameters: the atmospheric pressure, the relative humidity, and the temperature. Fig. 1.1 shows three atmospheric parameters measured on December 10, 2007 at Fairbanks by a weather balloon [14] for a height up to about 30 km. These data are invaluable to us because we can compare measured temperature and pressure data against the available models. The NASA developed MSISE-90 model [15] to describe neutral temperature and densities in Earth's atmosphere (up to 600 Km). Such a model is commonly used for temperature modelling in the upper Earth's atmosphere, and is used to model temperature profile in this section in order to estimate atmospheric absorption coefficients and propagation paths of a sound wave. The modelled temperature profile is compared with the measured (by the weather balloon) data (See Fig. 1.1). The pressure model is based on the exponential function $p = p_0e^{-az}$, where p_0 is the pressure at the ground, a is a constant and z is an altitude. There are no available models for relative humidity so, we have to rely on the measured data to estimate the atmospheric absorption. The relative humidity in air has a negligible effect on the atmospheric absorption in the upper atmosphere [16] and so, the relative humidity value are kept at 3% for heights above 31 Km.

The left, center, and right panels in Fig. 1.1 show the absolute temperature, pressure, and relative humidity as functions of altitude. Blue and red lines are physically measured and extrapolated values, respectively. In the temperature profile, there are roughly four regions: the troposphere (8-20 km), the stratosphere (20-45 km), the mesosphere (45-97 km), the thermosphere (above 97 km). The pressure profile is plotted in the logarithmic scale and decreases exponentially with altitude. All three quantities are extrapolated in increments of 500 m. These atmospheric profiles are used in later part of this Section to compute atmospheric absorption rates and propagation paths of a harmonic wave (at various frequencies) as a function of altitude.

International Organization for Standardization (ISO) develops international standards on a variety of subjects and make them available to the public [17]. The ISO 9613-1:1993(E) document provides an analytical method of computing the degree of atmospheric absorption under various meteorological conditions, and such a method is used to calculate the atmospheric absorption rate as a function of altitude. Fig. 1.2 shows atmospheric absorption rate (dB/km) of a harmonic wave for various frequencies as a function of height. The absorption rates for all frequencies increase near the boundary between the troposphere and stratosphere; however, the increase is less noticeable for a frequency of 10 Hz at the boundary. The coefficients remain fairly constant in the stratospheric region, but they increase exponentially above the stratosphere. The figure demonstrates that the absorption rate is lowest for low frequencies, which leads to the conclusion that a low-frequency sound wave in the atmosphere can be detected at farther range than a high-frequency wave can.

Low-frequency infrasound can travel global distances relatively unattenuated, however; such a wave is subject to significant refraction by the vertical temperature gradient and wind profiles of the atmosphere [3, 18]. Georges and Beasley [19] used the best available seasonal wind models to compute the effect of wind on the trace velocity and the azimuth of acoustic propagation; they found variations of 20 percent or more for the trace velocity and deviations of up to 10° for the bearing. Their wind models show seasonal

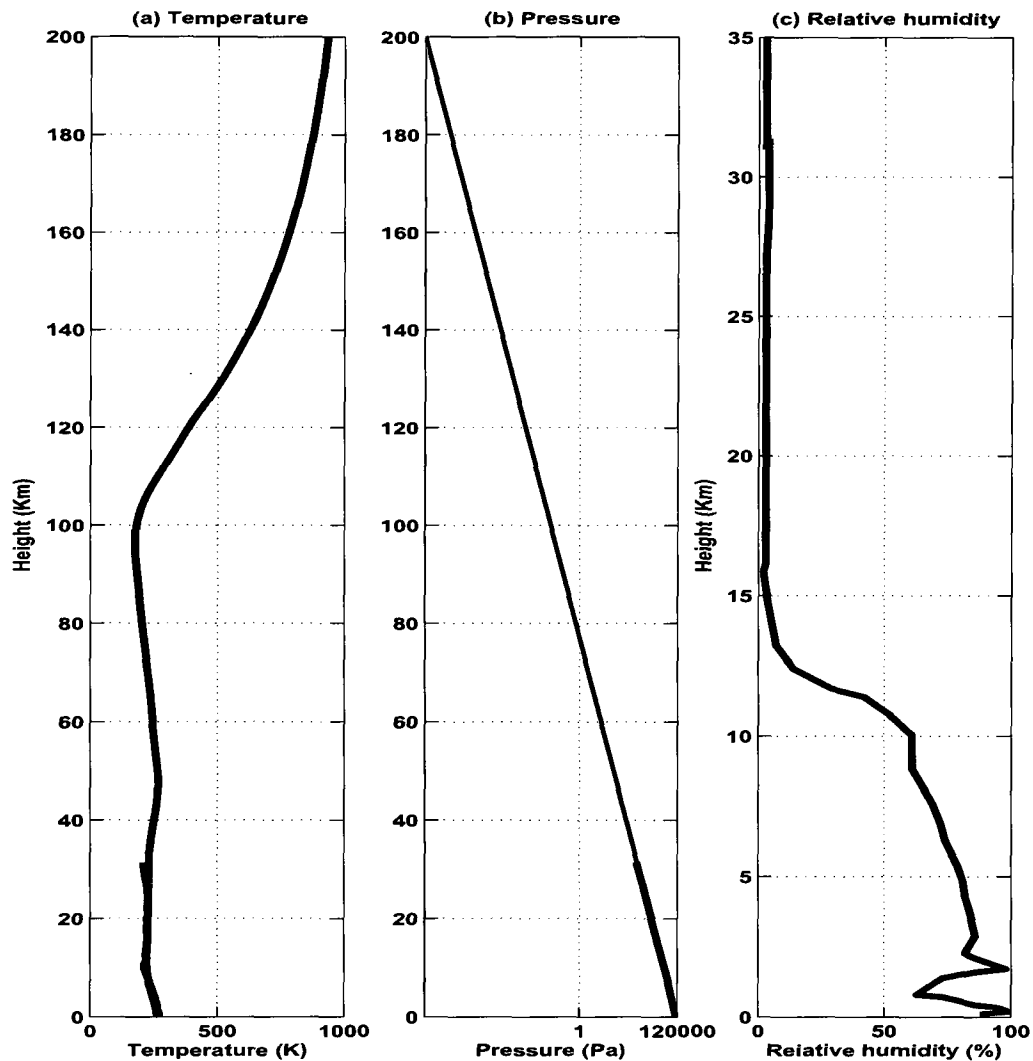


Figure 1.1. Measured and modelled atmospheric profiles at Fairbanks, Alaska. Blue and red curves in each of the profiles are measured (using a weather balloon [14] on December 10, 2007) and modelled quantity, respectively. (a) The MSISE-90 model [15] is used to model temperature profile up to 200 Km, (b) The pressure profile is modelled using an exponential function up to 200 Km and (c) Relative humidity values are kept fixed at 3% for heights above 31 Km (see text for details). These profiles are used in later part of this Section to estimate atmospheric absorption coefficients and propagation paths of a harmonic wave at various frequencies.

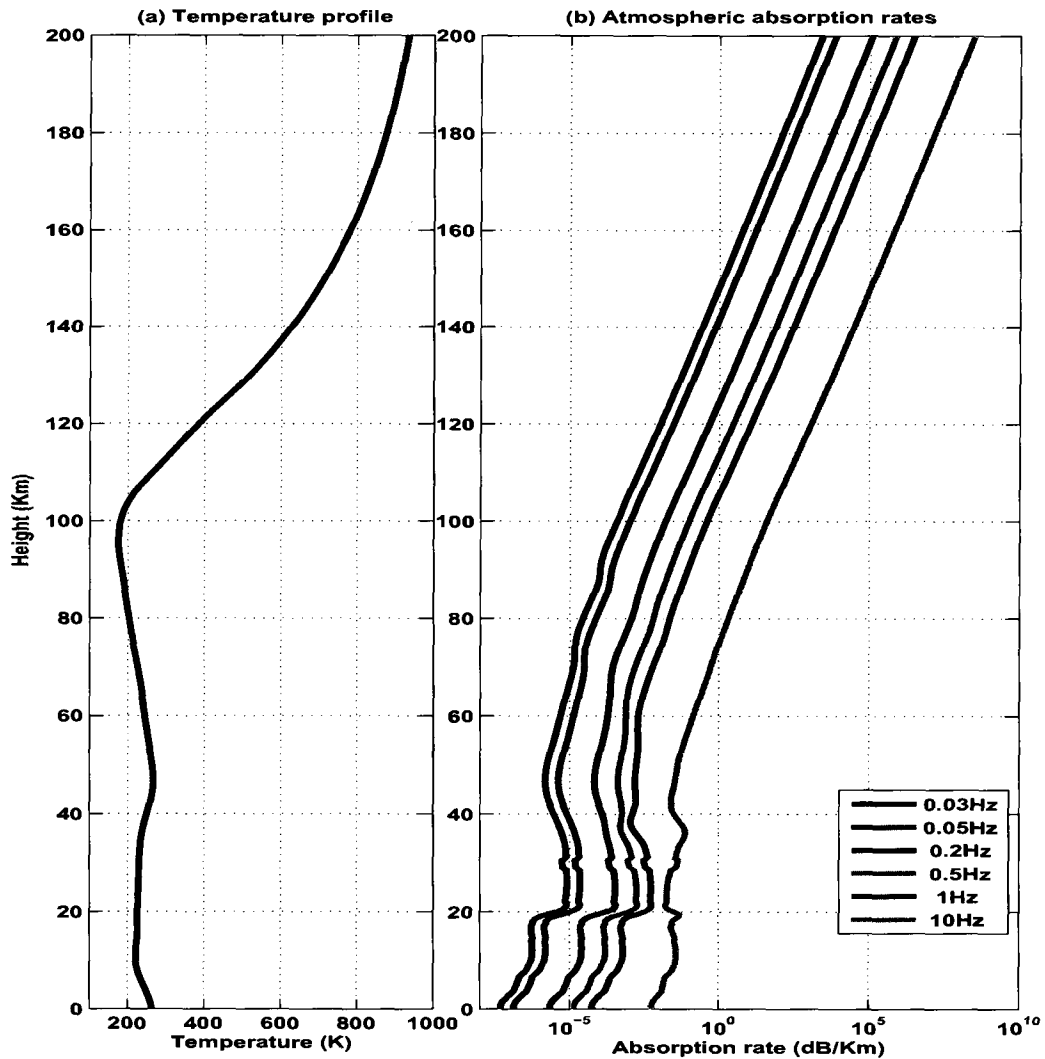


Figure 1.2. Atmospheric absorption rates (dB/Km) of a harmonic wave. (a) Temperature profile and (b) atmospheric absorption coefficients (dB/Km) as a function of frequency and height. The absorption rate increases as the frequency of the wave increases, which leads to the conclusion that a low-frequency wave in the atmosphere can be detected at farther range than a high-frequency wave can.

variations on the speed and the direction of winds in the upper atmosphere (up to 200 km), and variations are much larger in East-West direction than in North-South direction. Elford [20] uses radio observation to describe the behavior of prevailing winds in medium latitudes (80-100 Km), and he finds that the winds being directed toward the East for most of the year with presence of large wind gradient during summer and winter. Gorerke, Young, and Cook [21] provide direct evidence for the wind's effect on variations in the trace velocity and the azimuth estimation for long path, low-frequency sound waves. Most of the low-frequency sources studied in this thesis are less than 1,000 km away. At these ranges, the wind's effect on the propagation of sound waves may become significant. Unfortunately, it is very difficult or nearly impossible to obtain accurate three-dimensional wind and temperature profiles for a large scale studies like the one presented in this thesis. For this reason, we ignore the wind's effect on the propagation of sound waves.

The wave equation (Eq. 1.15) is solved in two dimensions using a ray tracing model, developed by Dr. Doug P. Drob of the Navy Research Laboratory [22, 23]. The model takes four input parameters: temperature, pressure, relative humidity, and wind speed. For the reason mentioned above and simplicity, we solve the wave equation for a stable atmosphere using one-dimensional atmospheric profiles described in Fig. 1.1.

The apparent sound speed (or trace velocity, V_t) of a wave arriving at the array with an elevation angle (ϕ) will be higher than the actual sound speed defined by Eq. 1.19. The elevation angle, ϕ , can be estimated from:

$$\phi = \cos^{-1}\left(\frac{c}{V_t}\right), \quad (1.20)$$

where V_t is a trace velocity. As we shall see soon, the ϕ is a key parameter that differentiates ground source signals from non-ground source signals. The azimuth (or θ) measures direction of arrival in degrees. In the later section, we will discuss the estimation of various characterization parameters and their uncertainties.

Fig. 1.3 shows the wave propagation paths and corresponding sound pressure levels of a harmonic wave with a frequency of 0.03 Hz, typical of what is studied in this thesis. Multiple rays are launched from a source located at the origin with various elevation an-

gles, and a sound speed of 325 m/s. In the top panel, we can see stratospheric (45 km) and thermospheric (120-140 km) returns to the ground. Strong winds can produce such returns [19], however; these returns are indistinguishable from the stratospheric and thermospheric returns. As we mentioned before, the wind's effect is ignored throughout this thesis.

When a sound wave travels through two different isotropic media, two things can happen to the wave: reflection occurs when the incident wave impinges upon the surface of a different medium; refraction occurs as the incident wave travels through the new medium. Good examples for the reflection and refraction are the ground surface and stratospheric returns in Fig. 1.3(a), respectively. In the atmosphere, the media is continuously variable with height, and so we must solve the differential form of the wave equation (Eq. 1.15) to obtain the propagation path of the wave [8, 9]. In 3-dimensional system, the wave equation becomes

$$\frac{\partial^2 u}{\partial t^2} = c(u)^2 \nabla^2 u, \quad (1.21)$$

where the sound speed (c) depends on the position (u), and the operator $\nabla^2 = \frac{\partial^2}{\partial x^2} + \frac{\partial^2}{\partial y^2} + \frac{\partial^2}{\partial z^2}$. The position u is given by

$$u(\vec{r}, t) = A(\vec{r}, t) e^{i(\vec{k}\vec{r} - \omega t)}, \quad (1.22)$$

where A is the amplitude of the wave, \vec{k} is the 3-dimensional wave vector, and ω is the angular frequency of the wave. The wavelength of a harmonic wave with a frequency of 0.03 Hz is approximately 10 km, which is larger than the scale height of the atmosphere (0.5 km) used in our ray tracing program. Therefore, the propagation paths of the wave shown in Fig. 1.3(a) are rough estimates; however, such a practice is widely used as a first approach in computing the wave propagation path [24].

Fig. 1.3(b) shows the amplitude attenuation of the harmonic waves. Such attenuation is caused by atmospheric absorption and the geometric spreading of the wave. For simplicity, we assume that the power of the sound wave has an isotropic distribution, then the attenuation of the sound wave [10] by spherical spreading is then given by

$$L_p = L_w - 10 \log(4\pi r^2) - \alpha r, \quad (1.23)$$

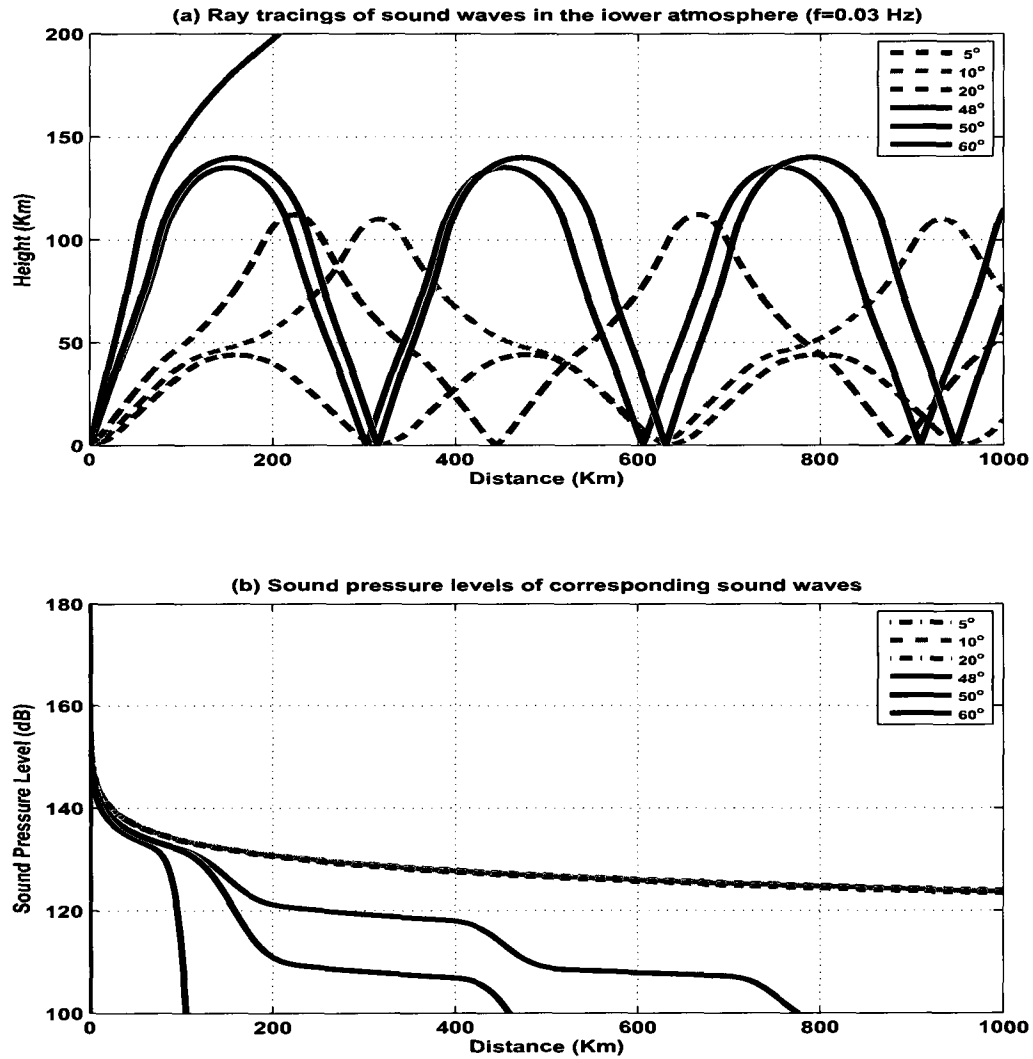


Figure 1.3. (a) Ray tracings and (b) corresponding sound pressure levels. All harmonic waves have a frequency value of 0.03 Hz, typical of what is studied in this thesis. Multiple rays are launched from the origin with various elevation angles, and the sound speed of 325 m/s. In (a), stratospheric (45 km) and thermospheric (120-140 km) returns can be seen. In (b), attenuation of the waves due to the spherical spreading dominates over the atmospheric absorption for the first a few kilometers. Notice that the attenuation is lowest for the low-elevation-angle rays.

where L_p is the sound pressure level in dB, L_w is the sound power level in dB, α is the atmospheric absorption coefficient (dB/m), and r is the radial distance in m. We arbitrarily chose a sound power level L_w to be 180 dB, which is a rough estimate of 1883 Krakatoa eruption, 161 Km from the source. The attenuation of a sound wave is dominated by the spherical spreading for the first a few kilometers of the propagation. The atmospheric absorption increases very rapidly, as the harmonic wave approaches the thermosphere. For example, a ray launched at 60° (blue curve) does not return to the ground and quickly gets absorbed by the thermosphere. On the other hand, a ray launched at 50° (black curve) returns to the ground, but with a significant power loss (70 dB). Notice that the difference in power loss (10 dB) of the waves between the two launch angles (48° and 50°) when the wave first returns to the ground. A harmonic wave with an elevation angle greater than 50° will have significantly higher power loss. Thus, we estimate the upper limit of the elevation angle (ϕ) to be 50° for the ground source signals. Since we cannot measure the amount of power loss in a signal, this does not determine whether we can detect the signal.

1.5 Instrumentation

A microphone is a device that converts acoustical energy into electrical energy, and the most common microphone design uses a thin membrane that vibrates in response to the pressure fluctuations in the atmosphere [25]. The microphones developed by Chaparral Physics are designed to operate in the frequency range between 0.01 and 200 Hz [4]. The Fairbanks (I53US) and Antarctic (I55US) arrays consist of eight Model 5 Chaparral microphone sensors [26, 27]. Fig. 1.4 shows the configuration of the Fairbanks array (located at Fairbanks, Alaska). Five microphones are placed at the vertices of a rough pentagon, with three microphones lying inside the pentagon in a triangular arrangement. The aperture of the array is approximately 1,700 meters and the inner three sensors are roughly 170 meters apart. Similar array configuration is used for the Antarctic array (located at Windless Bight, Antarctica). The array is designed to handle both long and short period signals.

Such an array design significantly reduces spatial and temporal aliasing for infrasound signals of interest to the CTBTO [4].

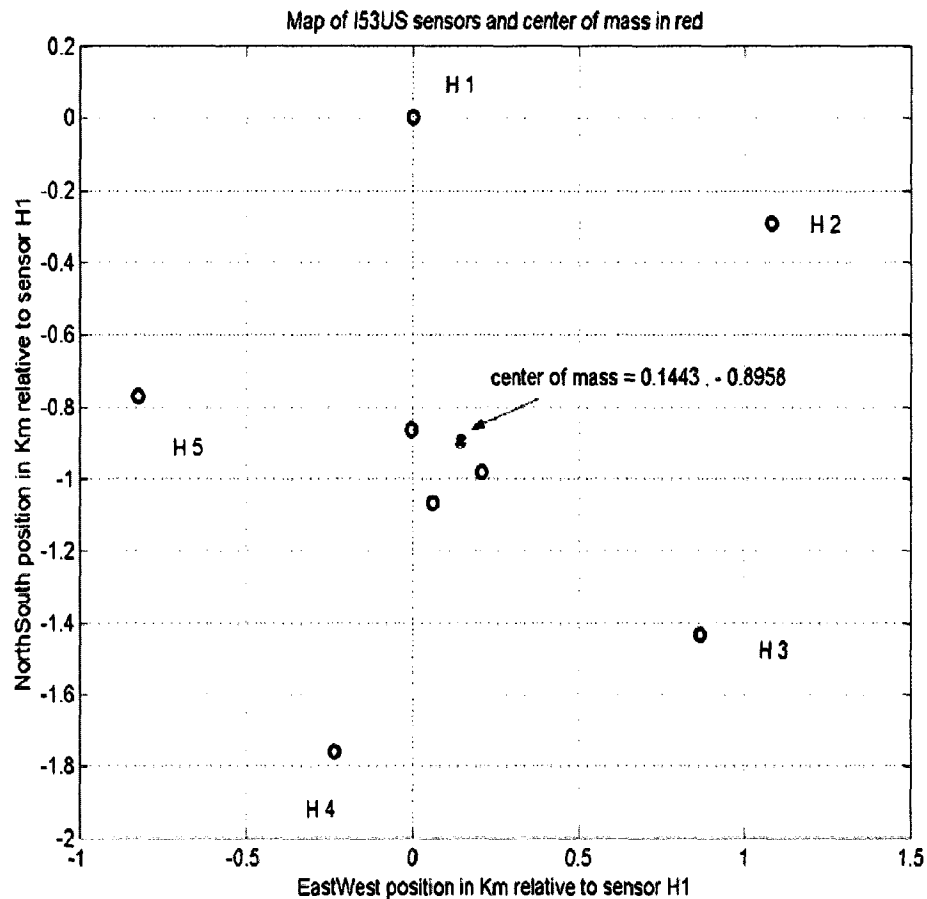


Figure 1.4. Fairbanks array (I53US) configuration. Geographic north and east are directed toward the positive y- and x-axes (measured in Km), respectively. Blue circles indicate microphone locations and the center of mass of the array is marked by red circle. Such an array design handles both long- and short-period signals while significantly reducing spatial and temporal aliasing for infrasound signals of interest to the CTBTO.

Each microphone is equipped with a four sets of noise reducers to minimize wind noise effects [2, 18]. Each noise reducer, or rosette, contains 28 low-impedance, vented

pipes arranged radially. Fig. 1.5 shows a noise reducing pipe system for one element of the Fairbanks array.

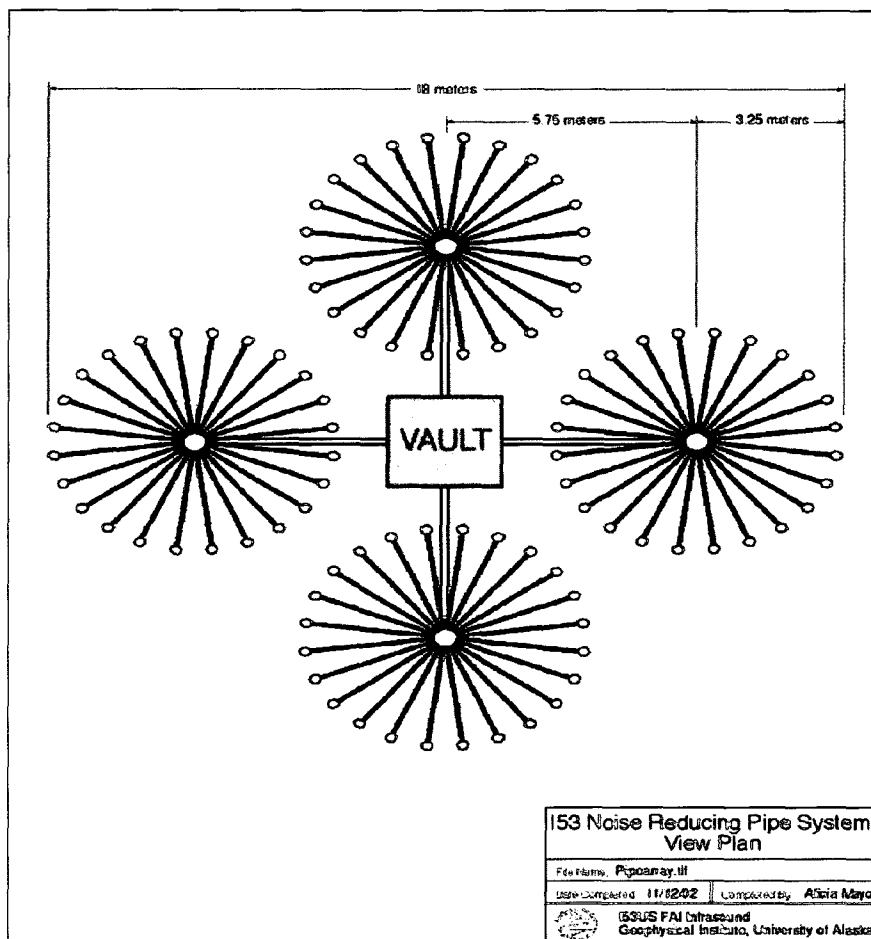


Figure 1.5. Noise reducing pipe configuration at I53US. The vault houses a Model 5 Chapparral Physics microphone sensor, Geotech digitizer and power supply. Each rosette contains 28 low-impedance, vented pipes arranged radially. Each vent is indicated by a small circle at the end of each pipe segment. The pipes all connect to a central summing manifold, indicated by the four large circles.

1.6 Estimation of Parameters

We estimate several parameters to characterize infrasound signals: the mean of the cross correlation maxima, Fisher statistic, trace velocity, azimuth, and planarity. The angle θ is measured clockwise from the geographic north. MCCM is a signal detection algorithm developed by Prof. John Olson of the Infrasound Group at the University of Alaska Fairbanks for infrasound signals recorded on an array. It is obtained by first computing cross correlations from all possible combinations of non-redundant sensor pairings to find the maximum correlation values and then taking the mean of all those cross correlation maxima.

There are two other signal detection algorithms examined in this thesis: the Fisher F statistic (F-stat) and the sum of the squares of variance ratios (SSVR). The former, which measures the ratio of signal to noise power, is used by some other infrasound groups to detect coherent signals across an array. The latter, which is developed for this thesis, is introduced and defined at the beginning of Chapter 3. In brief description, the SSVR detector utilizes principle component analysis [28] and covariance matrix [29, 30] of the power spectral densities to find correlated signals. Such detectors are computationally efficient and perform exceptionally well under the low signal to noise ratios. Detailed discussion of the three detection algorithms and their relative performance using receiver operating characteristics (ROC) curves are included in Chapter 3.

We borrow the notation of Olson and Szuberla [31] to derive equations used to estimate signal parameters and their uncertainties. Consider an array consisting of N sensors that lie in the plane at (x_i, y_i) , where $i = 1, \dots, N$. The standard bra-ket notation of Dirac [32] is used. Each sensor registers a different time of arrival as a plane wave passes through the array. A time delay vector $|\tau\rangle$ is computed by finding time delays that maximize the cross correlations from all possible combinations of non-redundant sensor pairings. For an array with eight sensors, time delay vector $|\tau\rangle$ may be written in the following matrix form

$$|\tau\rangle = \mathbf{X}|f\rangle, \quad (1.24)$$

where

$$|\tau\rangle = \begin{bmatrix} \tau_{12} \\ \tau_{13} \\ \vdots \\ \tau_{78} \end{bmatrix}, \quad \mathbf{X} = \begin{bmatrix} x_1 - x_2 & y_1 - y_2 \\ x_1 - x_3 & y_1 - y_3 \\ \vdots & \vdots \\ x_7 - x_8 & y_7 - y_8 \end{bmatrix}, \quad |f\rangle = \begin{bmatrix} \frac{\cos\theta}{v} \\ \frac{\sin\theta}{v} \end{bmatrix}.$$

Eq. 1.24 can be solved in the least squares sense to obtain estimates for the slowness vector ($|f\rangle$). For a perfectly plane wave in a noise free environment (with an infinite sampling rate), $|f\rangle$ is an exact solution to Eq. 1.24. This is, of course, not the case for real signals and we represent the time delay vector ($|f\rangle$) by adding a time error vector ($|\epsilon\rangle$)

$$|\tau\rangle = \mathbf{X}|f\rangle + |\epsilon\rangle. \quad (1.25)$$

Time measurement errors come from many sources, including: finite sampling, non-planar arrivals (from atmospheric turbulence or near-field sources), multiple arrivals from various azimuths, and wind noise. The presence of noise in a signal contributes to the non-planar wave arrival. Each element of the error vector is assumed to have a normal distribution with a zero mean and the same variance σ^2 .

The goal is then to find an estimate (\hat{f}) that minimizes the sum squared error $E = \langle \epsilon | \epsilon \rangle$ or,

$$E = \langle \tau - \mathbf{X}f | \tau - \mathbf{X}f \rangle, \quad (1.26)$$

We differentiate Eq. 1.26 with respect to the slowness vector ($|f\rangle$), set the equation to zero, and solve for the slowness vector ($|f\rangle$) [33]. The solution is given by

$$|\hat{f}\rangle = (\mathbf{X}^T \mathbf{X})^{-1} \mathbf{X}^T |\tau\rangle. \quad (1.27)$$

The estimate (\hat{f}) is an unbiased estimator and we can verify that simply by computing the expectation of Eq. 1.27 with a substitution of $|\tau\rangle$ from Eq. 1.25.

We define a residual error R_0^2 by substituting Eq. 1.27 into Eq. 1.26,

$$R_0^2 = \langle \tau | \mathbf{I} - \mathbf{R} | \tau \rangle, \quad (1.28)$$

where $\mathbf{R} = \mathbf{X}(\mathbf{X}^T\mathbf{X})^{-1}\mathbf{X}^T$ is an idempotent matrix. The expectation [33, 34] of Eq. 1.28 can be written as

$$R_0^2 = \hat{\sigma}^2 \text{Tr}(\mathbf{I} - \mathbf{R}), \quad (1.29)$$

$$\hat{\sigma}^2 = \frac{R_0^2}{M - r}, \quad (1.30)$$

$$M = \frac{N(N - 1)}{2}, \quad (1.31)$$

where r is the rank of the idempotent matrix \mathbf{R} and N is the total number of sensors in the array. The planarity (σ_τ) is measured in seconds and is obtained by taking a square root of $\hat{\sigma}^2$. The planarity measures how well the model (Eq. 1.24) fits the data, and it depends on the propagation distance, the propagation path, and the wavelength of the signal.

The trace velocity is defined as projection of true velocity in the plane of an array of microphones. The trace velocity and the azimuth of the plane wave crossing an array are given by

$$\hat{V}_t = \frac{1}{\sqrt{\hat{f}_1^2 + \hat{f}_2^2}}, \quad (1.32)$$

$$\hat{\theta} = \tan^{-1}\left(\frac{\hat{f}_1}{\hat{f}_2}\right), \quad (1.33)$$

where \hat{f}_1 and \hat{f}_2 are elements of the estimator $|\hat{f}\rangle$. The uncertainty of the slowness vector depends on σ_τ and V_t estimates.

From the distributions of $|\tau\rangle$ and Eq. 1.27, we can infer the distributions of the slowness vector $|\hat{f}\rangle$. Since the slowness vector follows χ^2 distribution, it is a natural choice to use constant chi square boundaries as confidence limits. Szuberla and Olson [35, 36] describe χ^2 method for computing uncertainty in the slowness vector estimate at confidence level p . They utilize the covariance matrix of the inter-station separations (\mathbf{X}) to describe the probability distribution of the slowness vector $Pr[|f\rangle]$

$$Pr[|f\rangle] = \kappa e^{-(1/2\sigma_\tau^2)\langle\tilde{f}|\mathbf{D}|\tilde{f}\rangle}, \quad (1.34)$$

where \mathbf{D} is the [2,2] diagonal matrix of eigenvalues of the covariance matrix $(\mathbf{X}^T\mathbf{X})$, $|\tilde{f}\rangle$ is projection of the residuals of the slowness vector into the principle axes of the covariance

matrix, and κ is some normalization constant. Then, constant probability surfaces (2-D ellipses) of the $|f\rangle$ are obtained by setting the exponent of the Eq. 1.34 to various constants. The uncertainty in the slowness vector estimate for q degrees of freedom and at p confidence level, for example, is given by

$$\chi_{q|p}^2 = \sum_{i=1}^2 \frac{\tilde{f}_i^2}{\sigma_{\tilde{f}_i}^2}, \quad (1.35)$$

$$\sigma_{\tilde{f}_i}^2 = \sqrt{\frac{\sigma_\tau^2}{D_{ii}}}. \quad (1.36)$$

Eq. 1.35 is an equation of ellipse, with semi-major and -minor axes given by \tilde{f}_i^2 . A fraction p of the ensemble of $|f\rangle$ estimates is then bounded by the ellipse.

Fig. 1.6 shows the uncertainty in trace velocity (δV_t) estimation as a function of V_t (green line) for the Fairbanks array. The artificial wave used to generate this plot has a center frequency of 0.03 Hz and an azimuth of 100° . The error bars are produced for two planarity values with a 90% confidence level. A MATLABTM algorithm called eventSig, developed by Prof. Curt A. L. Szuberla at the Geophysical Institute of the University of Alaska Fairbanks, is used to produce error bars. Blue and red curves show lower and upper limits of the trace-velocity estimate. Solid and dotted curves are produced with $\sigma_\tau = 0.5$ seconds and $\sigma_\tau = 0.3$ seconds, respectively. The error bars increase with larger V_t and σ_τ . For example, the uncertainty for $\sigma_\tau = 0.3$ seconds at $V_t = 1.0$ Km/s is roughly 0.3 Km/s; whereas, the uncertainty for $\sigma_\tau = 0.5$ seconds at $V_t = 1.0$ Km/s is approximately 0.5 Km/s. We ignore signals with the V_t greater than 1.5 Km/s due to their exceedingly high uncertainties. For $\sigma_\tau = 0.5$ seconds, the lower and the upper limits on V_t of 1.5 Km/s are 0.95 Km/s and 2.05 Km/s, respectively. We conclude that the uncertainty in V_t decreases (or the accuracy of the V_t estimate improves) with smaller V_t and σ_τ values.

Fig. 1.7 illustrates the uncertainty in azimuth ($\delta\theta$) estimation as a function of V_t for the Fairbanks array. The artificial wave used to generate this plot has a center frequency of 0.03 Hz and an azimuth of 100° . The error bars are produced for two planarity values with a 90% confidence level. The same MATLABTM algorithm (EventSig) is used to compute the error bars. Blue and red curves indicate the lower and upper limits of the azimuth

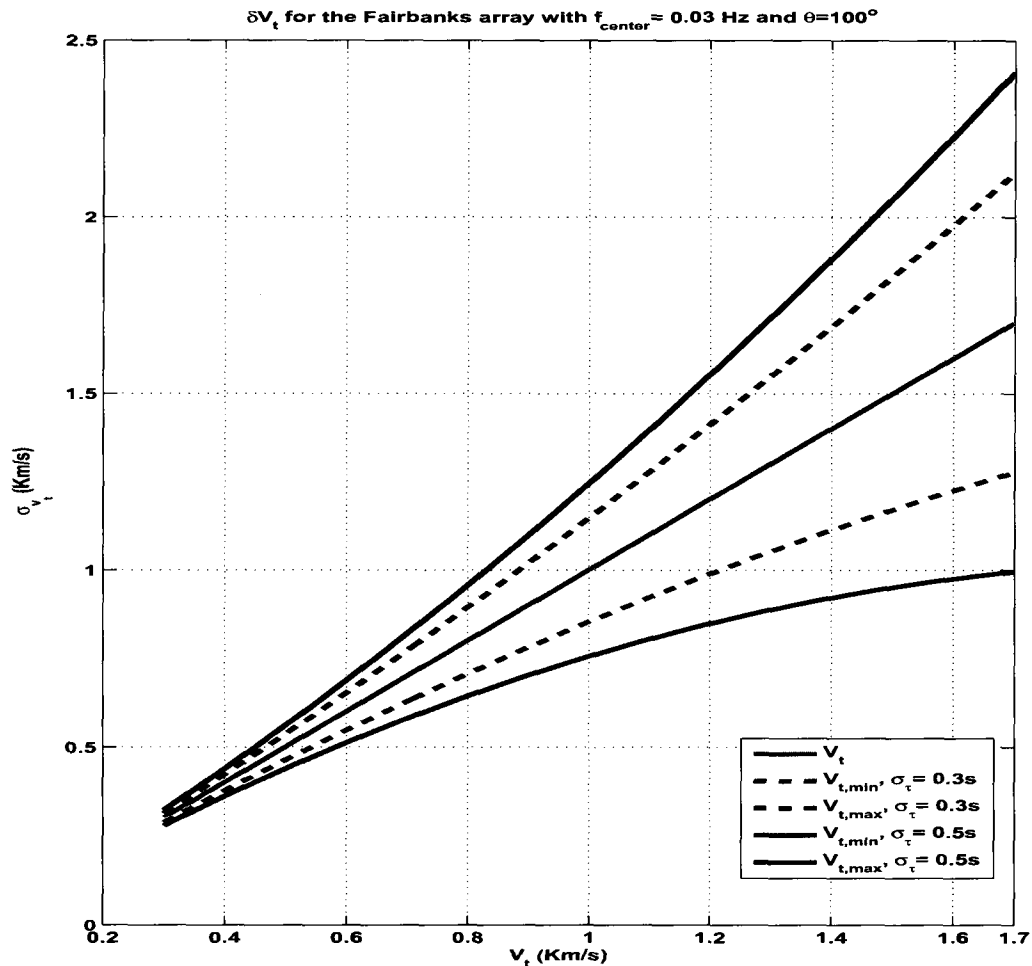


Figure 1.6. Uncertainty in trace velocity (V_t) estimation for I53US. The artificial wave used to generate this plot has a center frequency of 0.03 Hz and an azimuth of 100° . The error bars for the V_t (green line) are produced for two planarity values with a 90% confidence level. We conclude that the uncertainty in V_t decreases (or the accuracy of the V_t estimate improves) with smaller V_t and σ_τ values.

estimate. Solid and dotted curves are produced with $\sigma_\tau = 0.5$ seconds and $\sigma_\tau = 0.3$ seconds, respectively. The error bars increase with larger V_t and σ_τ values. For example, the uncertainty for $\sigma_\tau = 0.3$ seconds at $V_t = 1.0$ Km/s is roughly 17° ; whereas, the uncertainty for $\sigma_\tau = 0.5$ seconds at $V_t = 1.0$ Km/s is roughly 30° . Comparing with Fig. 1.6, we find that the δV_t

increases at a proportionally faster rate than $\delta\theta$ as the value of V_t estimate increases. We can conclude that the uncertainty in θ decreases (or the accuracy of θ estimate enhances) with smaller V_t and σ_r values. It is important to be aware of those error bars when we encounter V_t and θ estimates. Similar error bars (δV_t and $\delta\theta$) are expected for the Antarctic array.

1.7 High Trace Velocity Signals

On both the Fairbanks and Antarctic arrays, high trace velocity signals (HTVs) are defined as low-frequency infrasound signals with the V_t greater than 650 m/s. We are interested in HTVs because we suspect that a primary source mechanism is a strong magnetic disturbance in the Earth's ionosphere. It is a well-known observational fact that active auroras are accompanied by strong magnetic disturbances in the ionosphere. Wilson identified two types of aurora-related signals: one is generated by the lateral supersonic motion of auroral electro-jet currents [37, 38, 39, 40] and the other one is produced by pulsating auroras [41, 42, 40]. Wilson and Olson [42] confirmed the detection of pulsating auroral infrasound at the Fairbanks array using pulsating auroral images from the all-sky cameras.

Most of all-sky camera images become unavailable during the winter months because of cloudy sky. Unfortunately, active auroras are observed during the same period and so, we need a new method to study the relation between auroras and the HTVs. Fortunately, we have College International Geophysical Observatory (CIGO), which is located near Fairbanks, Alaska to measure local magnetic variation in the atmosphere [43]. In Chapter 3, time variations of local magnetic disturbances (from CIGO) are compared with those of HTVs to demonstrate a similarity (or correlation) between auroras and the HTVs.

As we shall see, the HTVs are quiet in the second and third quarters of the year and active in the first and fourth quarters of the year for the Fairbanks and Antarctic arrays (Figs. 3.10 and 3.19). The average temperature of the first and fourth quarters of the year at Fairbanks is roughly 19 °F, and the average sound speed during these quarters is approximately 327 m/s. Based on Eq. 1.20 and upper limit of the elevation angle ($\phi = 50^\circ$)

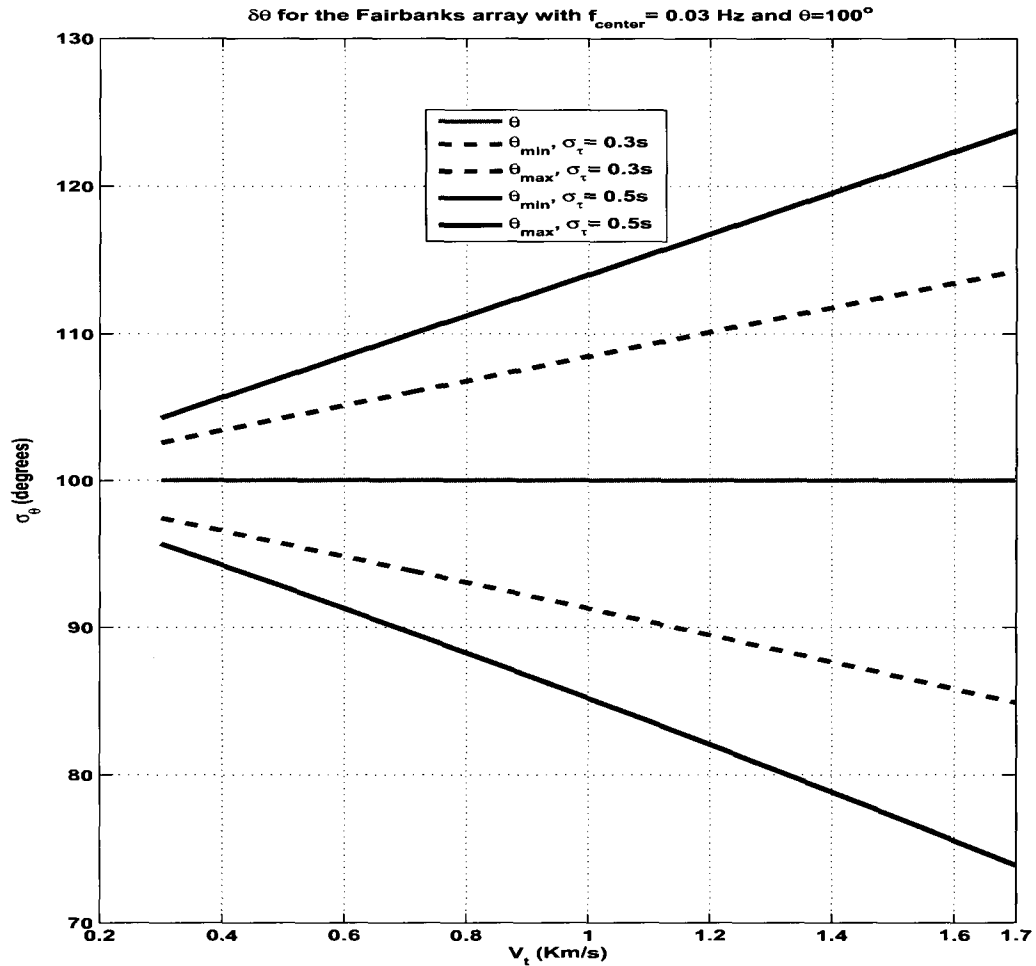


Figure 1.7. Uncertainty in azimuth (θ) estimation for I53US. The artificial wave used to generate this plot has a center frequency of 0.03 Hz and an azimuth of 100° . The error bars for the θ (green line) are generated for two planarity values with a 90% confidence level. We can conclude that the uncertainty in θ decreases (or the accuracy of θ estimate enhances) with smaller V_t and σ_τ values.

determined earlier for the ground source signals, we estimate the upper V_t limit for these signals to be approximately 600 m/s, including the uncertainty (refer to Fig. 1.6). The lower limit of the trace velocity for the HTVs is chosen to be 650 m/s (rather than 600 m/s) to minimize possible overlapping between the HTVs and ground source signals. The av-

erage temperature of the second and third quarters at Antarctic is roughly 10 °F, so we will keep trace velocity limits the same for the Antarctic array as well.

The MAWs, generated by the interaction of tropospheric wind flow over mountain ranges, can dominate ground source signals [44]. Analysis of the Fairbanks data shows that MAWs predominantly come from three mountain ranges in Alaska: the Saint Elias Range, the Alaska and Aleutian Ranges, and possibly the Seward and Chukotsk Peninsulas. Analysis of the Antarctic data shows that principle source of MAWs is the Alps Range of South Island, New Zealand. Both MAWs and HTVs have irregular waveforms, and their power spectrum density show almost no distinction from one to another. Therefore, the trace velocity is exclusively used to discriminate HTVs from the MAWs.

Chapter 2

Signal Review

2.1 Abstract

Our group's main responsibility is to detect and classify infrasound waves commonly observed at Fairbanks and Antarctic arrays. Examples of such waves include mine blasts, microbaroms, mountain associated waves (MAWs), and high trace velocity signals (HTVs). It is therefore vital for our group to identify these four signals from other unknown coherent signals detected at our stations. From our experience the detection quality of such signals degrades as the signal to noise ratios (SNRs) decrease, and to improve the detection quality, a new detection algorithm (sum of squares of variance ratios: SSVR) is developed in this thesis (refer to Chapter 3). Since the SSVR algorithm is based on temporal and frequency characteristics of the signals, large portion of this chapter is devoted to the waveforms and power spectrum of the four commonly observed signals at our arrays. As for completion, we add detection summary plots to illustrate temporal trend of various characterization parameters associate with each signal type. In Chapter 3, the performance of the SSVR detector is compared with the two well known detectors (MCCM and Fisher F-stat) using the receiver operating characteristics curves.

Each section in this chapter covers a different frequency group for signals of interests to our group: high frequency signals (0.5-10 Hz), microbaroms (0.1-0.5 Hz), and low frequency signals (0.015-0.1 Hz). We characterize the signals by computing various parameters: the mean of the cross correlation maxima (MCCM), trace velocity V_t , azimuth θ , and planarity σ_τ . The sampling rate of our digitizer for both the Fairbanks and Antarctic arrays is 20 Hz, and the data (collected by both arrays) are bandpass filtered accordingly (based on the frequency) before analysis. Our group uses a detection summary plot, which summarize computed characterization parameters (F-stat, MCCM, V_t , θ and σ_τ) based on frequency group (and window size) over 24-hour period, to search coherent infrasound signals. Fig. 2.5 shows an example of detection summary plot for microbaroms (0.1-0.5 Hz). To visualize the waveform of the signal, we use DataScan, which is a MATLABTM based

program developed by the Infrasound Group at the University of Alaska Fairbanks. Using the summary plot, DataScan, and other available information, we can detect, characterize, and identify the majority of infrasound signals received at the Fairbanks and Antarctic arrays.

2.2 High Frequency Signals

High frequency signals consist of both man-made and naturally produced infrasound signals. Over the years, we have identified various sources of high-frequency signals at the Fairbanks array: avalanches [45], bolides [46], convective storms [47], aircraft, house fires, explosions, lightning, etc. Most of the high-frequency signals do not propagate over long distances (>250 Km) due to high atmospheric absorption rates (refer to Fig. 1.2), however; they can take multiple propagation paths to get to the array [48]. Arnoult et al. [45] show an example of possible multiple ray-paths using infrasound data produced by an avalanche of Mt. Stellar.

We have also been observing mine blasts from two nearby mines (True North and Fort Knox) at the Fairbanks array. They are approximately 30 km from the array at 30° and 60° (measured clockwise from the geographic north). Fig. 2.1 shows an example of a mine blast recorded at the Fairbanks array around 0:00 UT on February 24, 2007. The data were bandpass filtered from 0.5 to 10 Hz to remove microbaroms and low-frequency signals. The top eight panels show the waveform received by each sensor of the array, and the last panel shows a phase aligned overlay of all waveforms. It has a typical N-shaped waveform of an explosion and lasts for nearly 4 seconds, with an approximate rise time of 0.5 seconds. The MCCM value of 0.977 indicates that this mine blast was highly correlated across the array. The V_t , θ , and σ_τ values of the mine blast are 316.5 m/s, 59.1° , and 0.02 seconds. The average temperature on that day was -13°F and the sound speed was approximately 316 m/s (based on Eq. 1.20). The planarity (σ_τ) is a frequency dependent quantity, and based on our experience, a high-frequency signal is considered to be planar if its σ_τ is less than 0.05 seconds for the Fairbanks and Antarctic arrays. The planarity value suggests that

a plane wave propagated through the array, and the sound speed implies that the wave front is parallel to the plane of our array. The mine blast has a peak-to-peak pressure value of 1.3 Pa at the array.

In the signal processing, it is very important to understand the effect of sharp edges (or discontinuities) in the data when computing the Fourier transform because these sharp edges introduce artificially high frequency components [49, 11]. There are various types of windows we can use to minimize such effect by applying a taper to the data. Throughout this chapter we use the L-point symmetric Hamming window [50, 51], given by

$$w(n) = 0.54 - 0.46\cos\left(2\pi\frac{n}{L-1}\right), \quad (2.1)$$

where $0 \leq n \leq L - 1$.

Fig. 2.2 depicts the mean power spectral density (green curve) of the mine blasts (shown in Fig. 2.1) and its error bars (blue and red curves) in log-log scale. All PSDs shown in this chapter are estimated using the Hamming window and Periodogram [52] function available from the MATLABTM signal processing toolbox [53]. The error bars are computed by assuming each point in the spectrum follows χ^2 distribution with 2 degrees of freedom. Then, the total number of degrees of freedom used to estimate uncertainties for the mean PSD is 16. The upper and lower limits of the mean PSD are based on a 90% confidence level. Notice an abrupt drop at 0.5 Hz due to the band-pass filter (0.5-10 Hz) and a broadband peak near 2 Hz, which is a characteristic of mine blasts.

2.3 Microbaroms

Microbaroms are atmospheric acoustic waves generated by the non-linear interaction of counter-propagating ocean waves [54, 55]. They are characterized by nearly sinusoidal waveforms with a period of approximately 5 seconds (0.2 Hz) and can persist for tens of hours. Olson and Szuberla [56] have shown that microbaroms can be decomposed into multiple wave packets by applying the Hilbert transform to the signal. The distribution function of wave packet length remains roughly the same, regardless of the data size, and the most probable packet length is 5 seconds. Observed microbaroms are often spatially

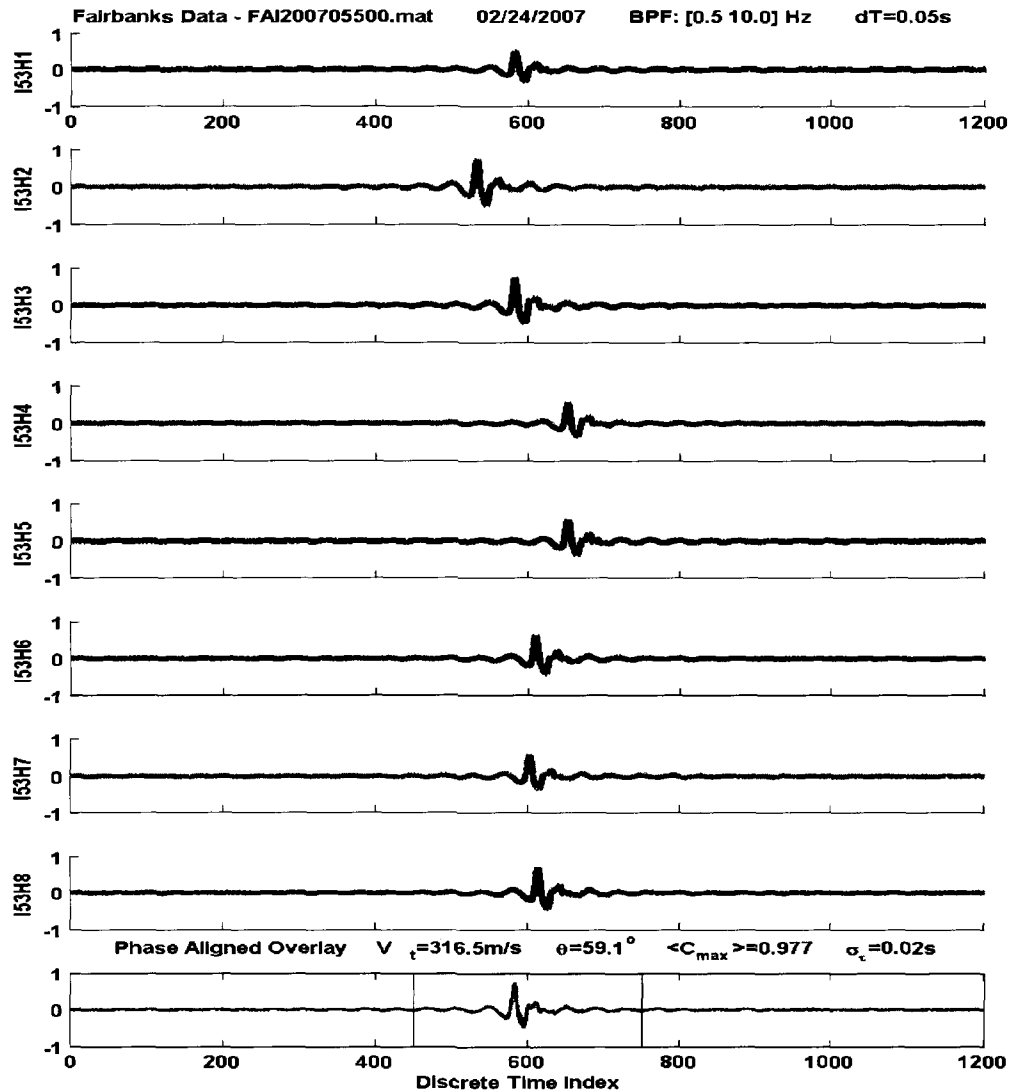


Figure 2.1. Example of mine blasts observed at I53US on February 24, 2007. The data are bandpass filtered from 0.5 to 10 Hz to remove microbaroms and low-frequency signals. The top eight panels show pressure fluctuations (in Pa) recorded at eight microphones as a function of time (in seconds), and the last panel shows a phase-aligned overlay of the waveforms from all eight sensors. Based on the estimated parameters, highly correlated plane wave propagated through the array, roughly parallel to the ground. See text for details.

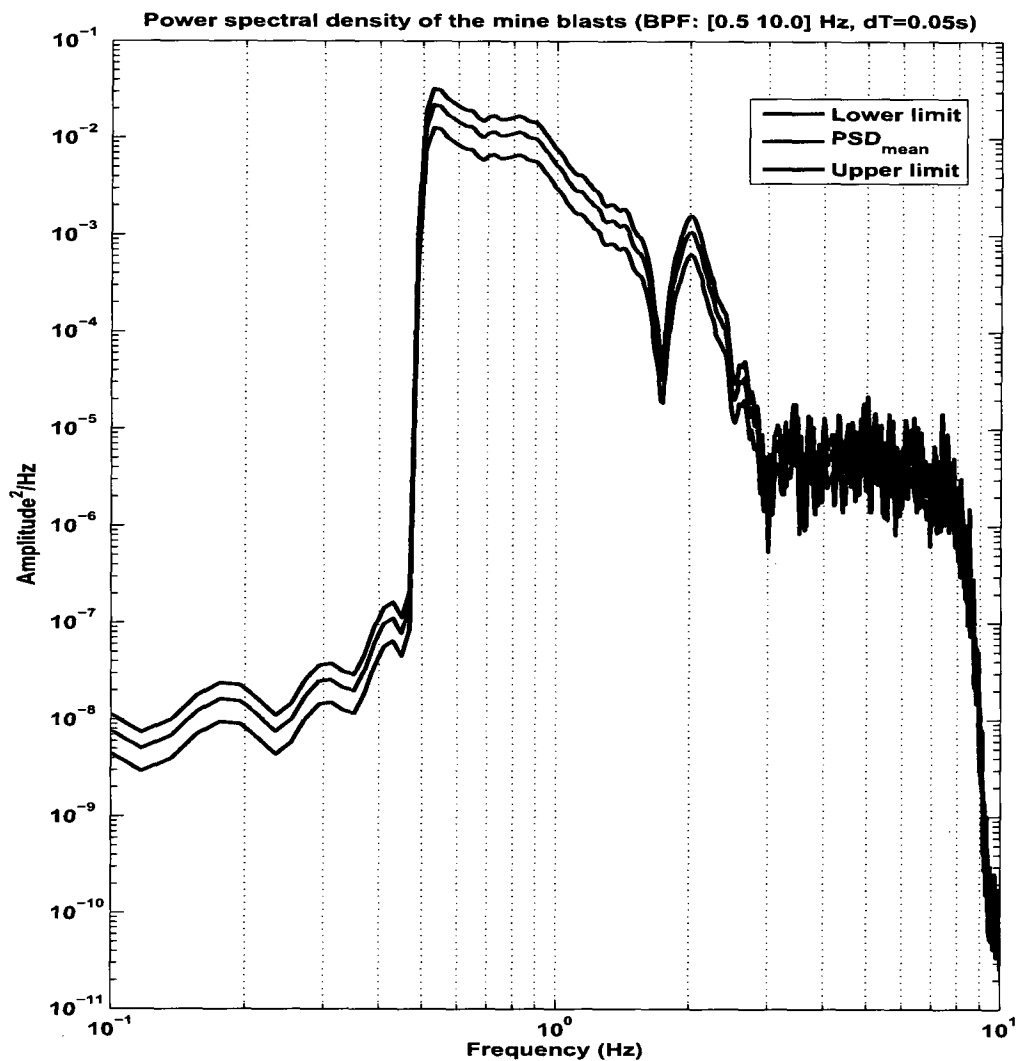


Figure 2.2. PSD of the mine blasts (in Fig. 2.1). The mean PSD (green curve) is estimated using the Periodogram method [52] with a Hamming window. The error bar for each point in the spectrum is computed with 16 degrees of freedom at a 90% confidence level. Notice an abrupt drop at 0.5 Hz due to the band-pass filter (0.5-10 Hz) and a broadband peak near 2 Hz, which is a characteristic of mine blasts.

incoherent across distance of order 2 km as shown by Olson and Szuberla. The effect of spatial incoherence can be seen by computing the MCCM of the observed microbaroms using only the inner three sensors of the Fairbanks array, and comparing with the MCCM of those calculated with all eight sensors of the array.

Fig. 2.3 shows an example of microbaroms observed at the Fairbanks array around 7:00 UT on September 25, 2006. The data are bandpass filtered from 0.1 to 0.5 Hz to remove low- and high-frequency signals. The figure is as for Fig. 2.1 The waveforms have a train of nearly sinusoidal wave packets. Low MCCM value (0.598) is expected because they are spatially incoherent signals. The V_t , θ , and σ_τ values of the microbaroms are 309.3 m/s, 249.2°, and 1.014 seconds. From our experience, microbaroms are considered to be planar if its σ_τ is less than 0.5 seconds. Clearly, these estimations are invalid because our solution model is based on the plane wave approximation. To minimize the spatial incoherence of the signal across the array, we only use four nearby sensors (H4, H6, H7, and H8) and recompute the characterization parameters: MCCM=0.85, V_t =337.6 m/s, θ =235°, and σ_τ =0.013 seconds. The V_t and σ_τ values suggest that a plane wave packet propagated through the array, parallel to the ground. The observed signal has a peak-to-peak pressure variation of 0.1 Pa.

Fig. 2.4 shows the mean PSD (green curve) of the microbaroms shown in Fig. 2.3 and its error bars at a 90% confidence level (blue and red curves) in log-log scale. The PSD and its uncertainties are computed same way, as in Fig. 2.2. Notice a broadband peak near 0.2 Hz, typical of microbaroms and the natural width of the spectrum is a few tenth of a hertz wide. Reduced frequency range (0.005-1.0 Hz) is used to show details of the spectrum.

Fig. 2.5 is a detection summary plot of microbaroms at the Fairbanks array on September 25, 2006. This type of summary plot is commonly used in our analysis and is generated by taking the following steps: first, gather a day's worth of array data; second, apply a bandpass filter from 0.1 to 0.5 Hz in order to remove low- and high- frequency signals; third, estimate parameters for a sliding window (in time) that is 1200 points (60 seconds) long with 50 percent overlap. The parameters include the F-stat, MCCM, V_t , θ , and σ_τ .

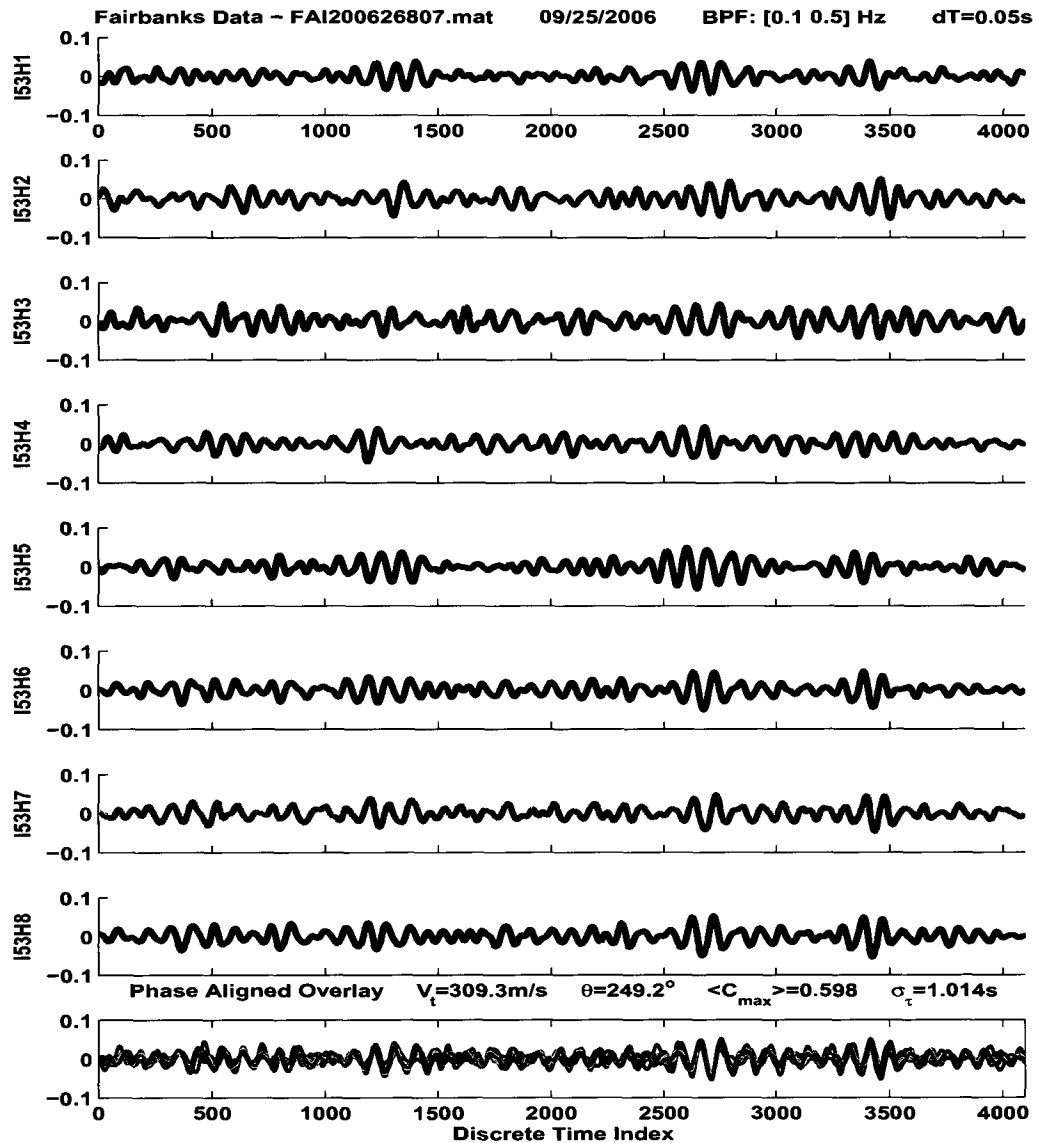


Figure 2.3. Example of microbaroms observed at I53US on September 25, 2006. The data are bandpass filtered from 0.1 to 0.5 Hz to remove low- and high-frequency signals. The figure is as for Fig. 2.1. Notice a train of nearly sinusoidal wave packets and low MCCM value that are characteristics of microbaroms.

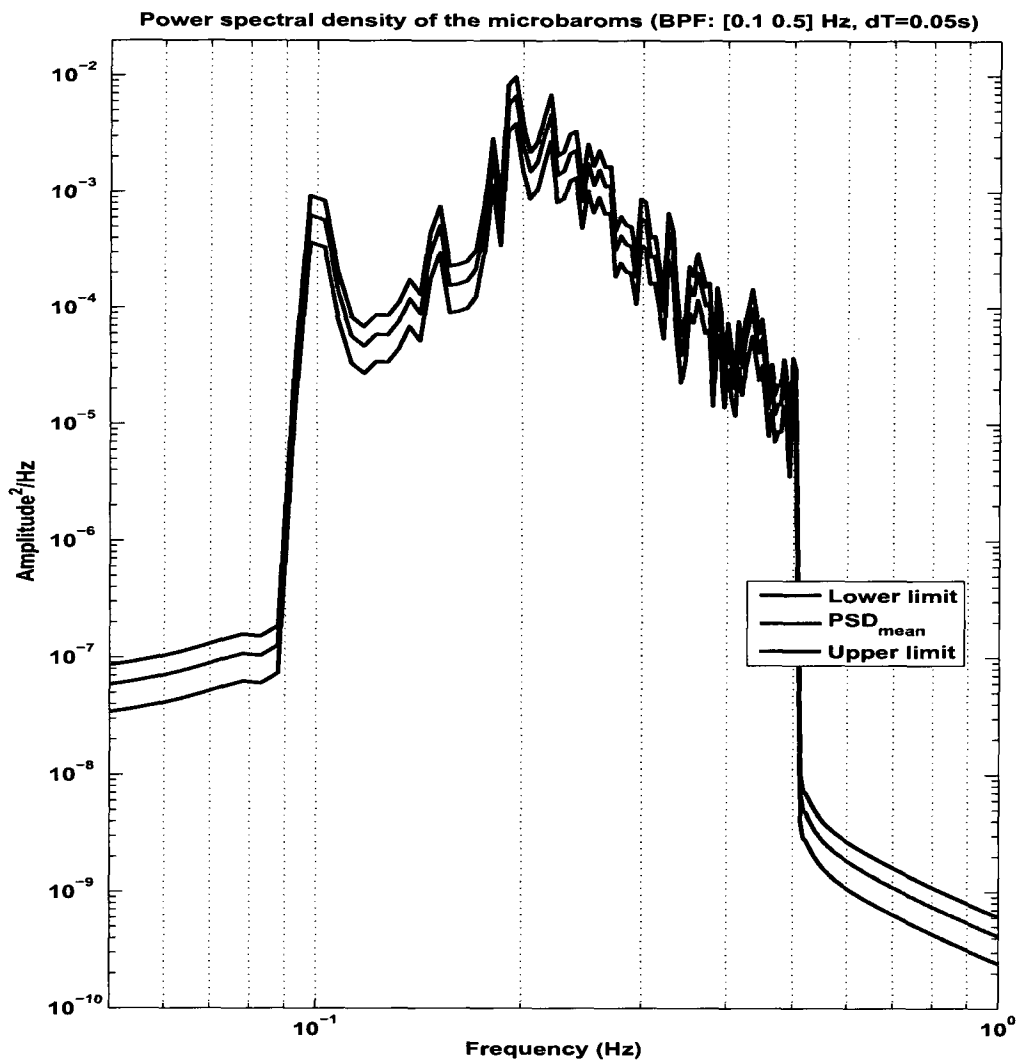


Figure 2.4. PSD of the microbaroms (in Fig. 2.3). The PSD and its error bars are computed same way, as in Fig. 2.2. Notice a broadband peak near 0.2 Hz, typical of microbaroms and the natural width of the spectrum is a few tenth of a hertz wide. Reduced frequency range (0.005-1.0 Hz) is used to show details of the spectrum.

The top two sub-plots of the figure show histograms of the MCCM and F-stat values, with thresholds indicated by red stripes. Thresholds for the F-stat and MCCM values are determined empirically (refer to Section 3.3), and they are found to be 5 and 0.75, respectively. The bottom five panels show the values for F-stat, MCCM, V_t , θ , and σ_τ as a function of time. In each of the five panels a blue "x" represents a computed value for each window (spaced 60 seconds apart). In the F-stat plot, events with an F-stat value greater than the threshold are enclosed by green "o". In the next three plots, events with an MCCM value larger than the threshold are enclosed by red "o". The last panel shows plane wave events (with $\sigma_\tau < 0.15$ seconds). We observe strong microbarom activity from 3:00 to 7:00 UT, with an azimuth directed toward the Bering Sea.

Fig. 2.6 shows probability density functions of the V_t and θ for microbaroms observed at the Fairbanks array for the period 2004-2007. Both plots are generated with Gaussian kernel width (2% of the data span), and the area under each curve is normalized to one. The red and blue curves represent V_t and θ variations, respectively. Microbaroms are selected by taking the following steps: first, create a three-hour long data set by appending the hour before and after an hour of interest; second, apply a bandpass filter from 0.1 to 0.5 Hz in order to remove low- and high-frequency signals, and select the middle hour of data; third, estimate parameters for the hour-long data by sliding a window size of 1200 points (60 seconds) with 50 percent overlap; finally, select microbaroms that satisfy the following selection criteria: $MCCM > 0.5$ and $\sigma_\tau < 0.5$ seconds. We observe that microbaroms have an average trace velocity of 345 m/s ($\phi \simeq 19^\circ$ based on Eqs. 1.19 and 1.20 with average winter Temperature of 19 °F) and originate from an azimuth between 230° and 270° , which is directed toward the Bering Sea. Observed microbaroms at the Fairbanks array are most frequent during the winter months, and most of active marine storms generated in the Bering Sea are also produced during the winter months.

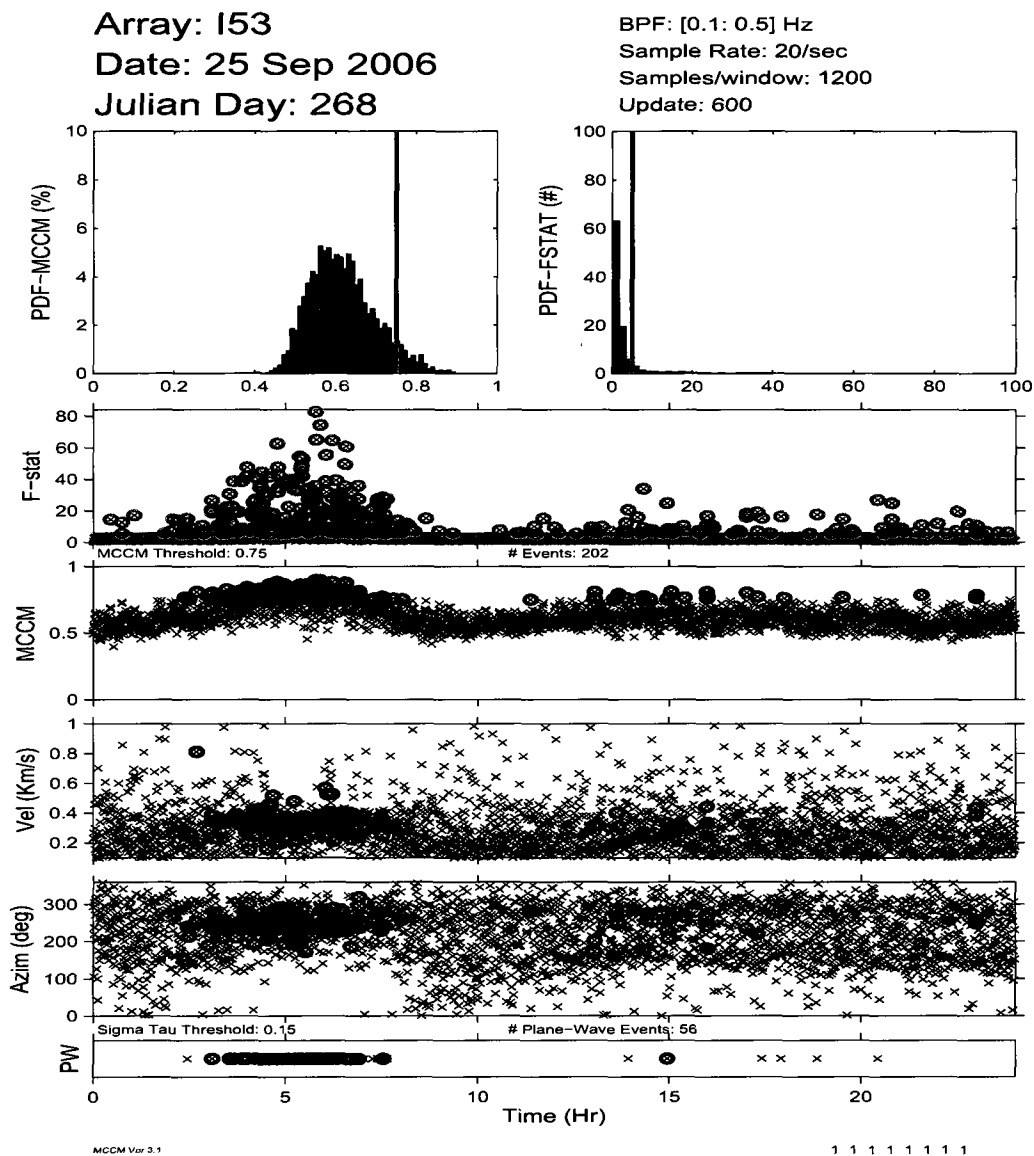


Figure 2.5. Detection summary plot of microbaroms on September 25, 2006 at I53US. The top two sub-plots show histograms of the MCCM and F-stat values, with thresholds (0.75 and 5) indicated by red stripes. The bottom five panels show the values for F-stat, MCCM, V_t , θ , and σ_τ as a function of time. In each of the five panels a blue “x” represents a computed value for each window (spaced 60 seconds apart). Notice that the microbarom activity lasts for a few hours. See text for details.

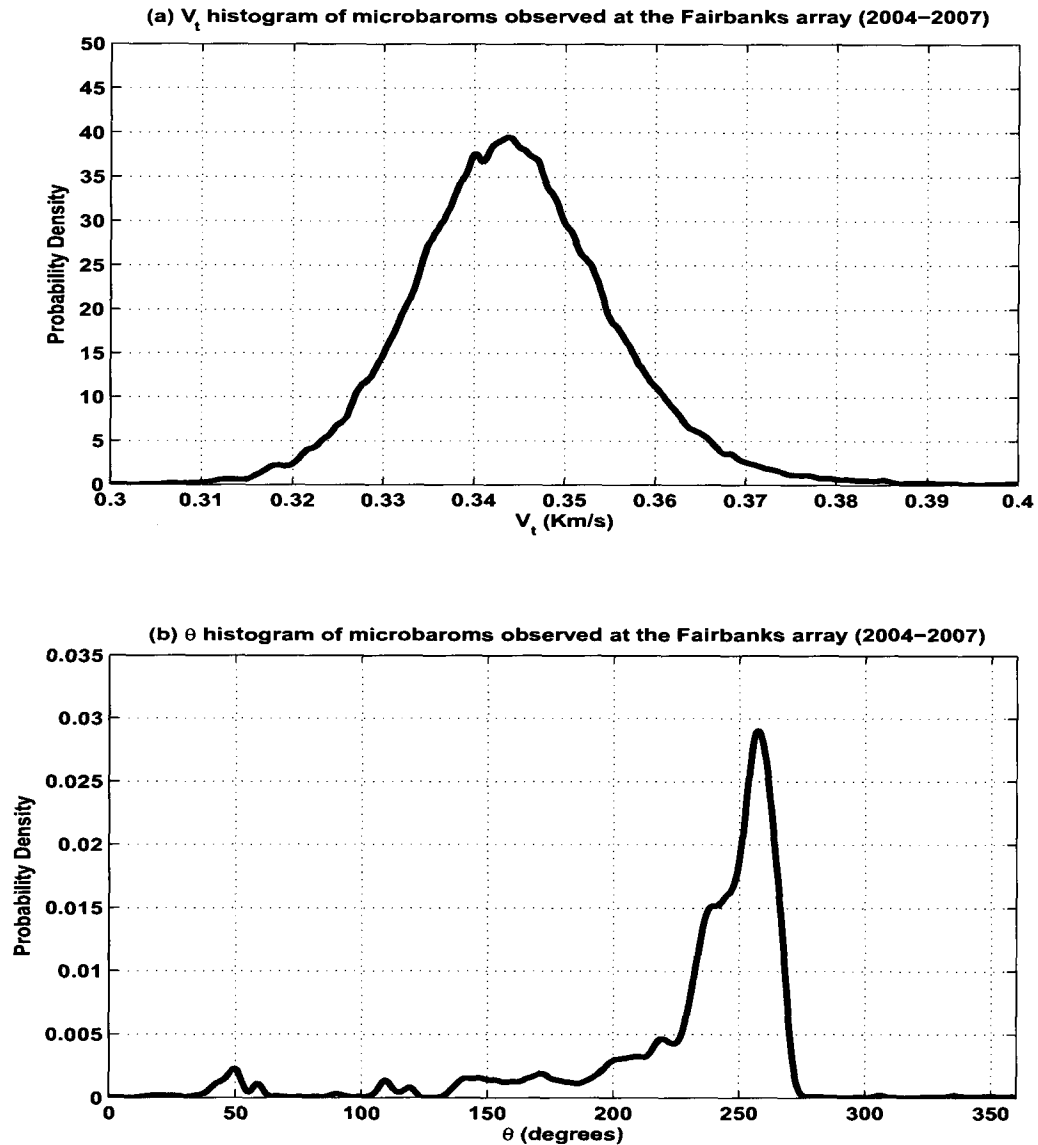


Figure 2.6. (a) V_t and θ histograms of microbaroms detected at I53US. The red and blue curves indicate V_t and θ histograms, respectively. Selected microbarom events (for the period 2004-2007) have $MCCM > 0.5$ and $\sigma_\tau < 0.5$ seconds. They have an average trace velocity of 345 m/s and originate from an azimuth between 230° and 270° , which is directed toward the Bering Sea.

2.4 Low Frequency Signals

Several geophysical infrasound signals fall into the low-frequency category, including: gravity waves [57] (although these do not propagate in the atmosphere), earthquakes [58, 59, 60], hurricanes [55], volcanic eruptions [61, 62, 63], mountain associated waves [44, 64], meteor [65], and aurora-related signals [38, 39, 41, 42, 64]. For example, high-amplitude infrasound waves are generated by two very large Alaska earthquakes occurred on October 23 and November 3, 2002. Wilson [58] analyzed the infrasound data from these events and detected the two earthquakes (M7.9 and M6.9), confirming their origin near the Denali Fault, about 90 miles to the south of Fairbanks. Each event consists of a Rayleigh (or seismic) wave followed by an acoustic wave. As described before, the two dominant low-frequency signals we observe (at I53US and I55US) are MAWs and HTVs. The sources of MAWs are mountain ranges, and we suspect that the sources of HTVs are magnetic disturbances in the upper atmosphere. In Chapter 3, we will apply V_t limits (derived in Section 1.7) to discriminate MAWs from HTVs.

2.4.1 Mountain Associated Waves

Mountain associated waves stem from atmospheric turbulence generated by the interactions between tropospheric wind flow and mountain ranges [44]. They are long-period signals with periods in the range 20 to 70 seconds (roughly 0.015-0.05 Hz) and have very irregular waveforms. MAWs have trace velocities typically less than 600 m/s. Atmospheric absorption rates for low-frequency signals are very low, and they can propagate thousands of kilometers with a very little attenuation (refer to Fig. 1.2).

Wilson and Olson [44] provide an overview of the MAW events from both the Fairbanks and Antarctic arrays. Fig. 2.7 illustrates azimuth-trace velocity diagram of observed MAW events at Fairbanks and Antarctic arrays in general. In each of the polar plots, red "*" indicates MAW event and blue concentric circles denote trace velocity values from 200 to 600 m/s. The direction of arrival is measured clockwise from geographic north (0°). For the Fairbanks array, selected MAW events have $MCCM > 0.9$, $\sigma_\tau < 0.3$ seconds, and

$0.3 < V_t < 0.6$ Km/s. Two known sources of the MAW events for the Fairbanks array are the Saint Elias Range (110° - 150°) and Alaska and Aleutian Ranges (170° - 230°). We suspect the third cluster of MAW events (275° - 300°) is from Seward and Chukotsk Peninsulas. For the Antarctic array, selected MAW events have $MCCM > 0.8$, $\sigma_\tau < 0.5$ seconds, and $0.3 < V_t < 0.6$ Km/s. A primary source of MAW events is the Alps Range of South Island, New Zealand (340° - 10°). It is worthwhile to note that the mountain range is not a point source, and one must keep in mind of uncertainties in the V_t and θ estimates when analyzing such diagrams (refer to Figs. 1.6 and 1.7). In Chapter 3, we will show these directional dependences coincide with our findings by analyzing four years worth of the Fairbanks and Antarctic data. Unlike other low-frequency signals, MAWs have a persistence in the azimuth and can last for hours or even days [44].

Fig. 2.8 shows examples of MAWs (from Alaska and Aleutian Ranges) observed around 9:00 UT at the Fairbanks array on November 22, 2006. The data are bandpass filtered from 0.015 to 0.1 Hz to remove microbaroms and high-frequency signals. The figure is as for Fig. 2.1. Notice the irregular waveform, which is a characteristic of the MAW. The $MCCM$ value of 0.91 indicates that the MAWs are highly correlated across the array. The V_t , θ , and σ_τ values are 419.3 m/s, 202.5° , and 0.26 seconds. From our experience, a low-frequency signal is considered to be planar if σ_τ is less than about 0.5 seconds. The V_t and σ_τ values (from Eqs. 1.19 and 1.20) suggest that the plane wave arrived at the array at an elevated angle (ϕ) with respect to the plane of our array. The MAWs have a peak-to-peak pressure value of 0.16 Pa.

Fig. 2.9 shows the mean PSD (green curve) of the MAWs shown in Fig. 2.8 and its error bars at a 90% confidence level (blue and red curves) in log-log scale. The PSD and its uncertainties are computed as for Fig. 2.2, and reduced frequency range (0.005-1.0 Hz) is used to show details of the spectrum. It is evident that isolating unique frequencies responsible for local peaks is a difficult task due to uncertainties in the spectrum. For example, the first local peak in the spectrum can be roughly anywhere between 0.015 to 0.1 Hz. Similar situation applies for other local peaks in the spectrum. In addition, shapes

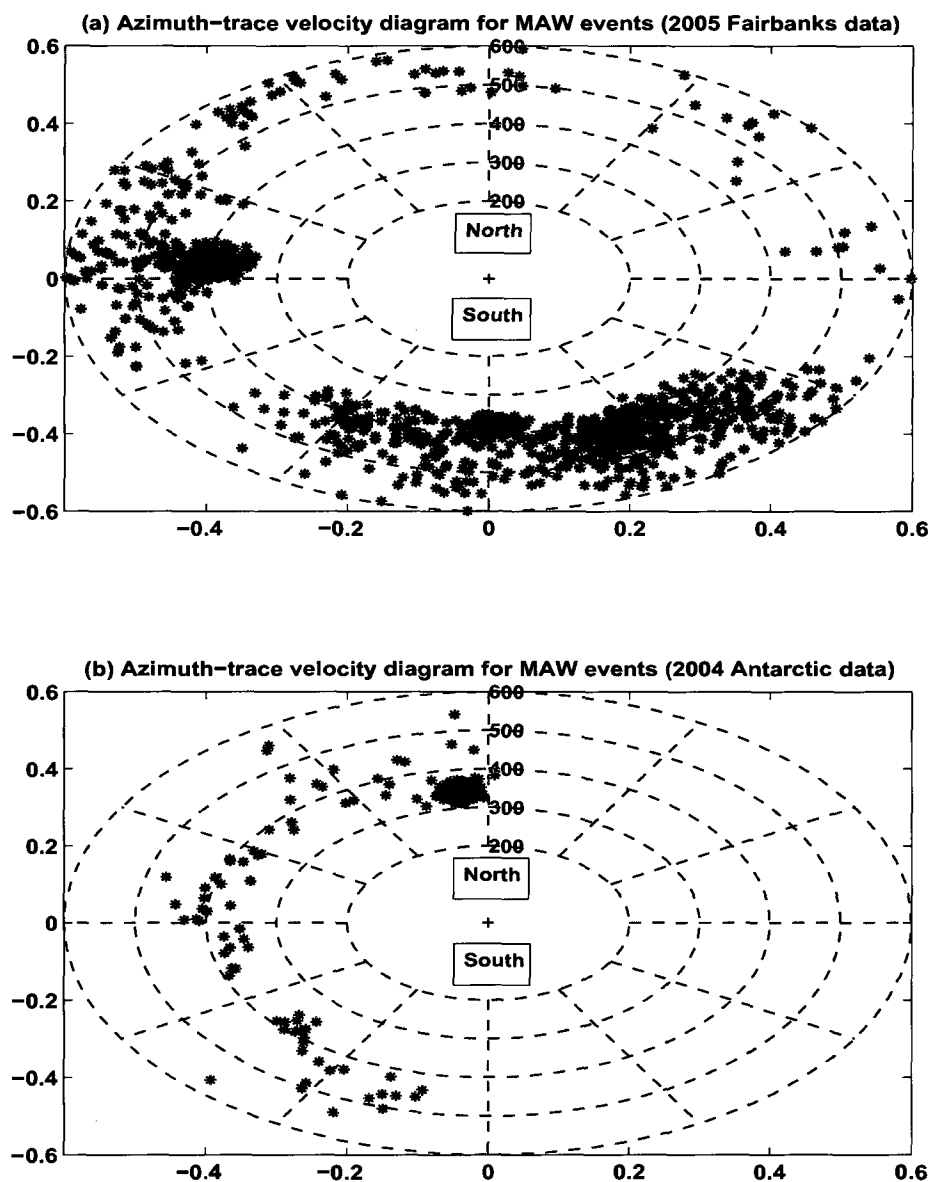


Figure 2.7. Azimuth-trace velocity diagram for MAWs observed at I53US and I55US. (a) Fairbanks data (year 2005) and (b) Antarctic data (year 2004). In (a) and (b), red “*” indicates MAW event and blue concentric circles denote trace velocity values from 200 to 600 m/s. The direction of arrival is measured clockwise from the geographic north (0°). Notice that the mountain range is not a point source, and one must keep in mind of uncertainties in the V_t and θ estimates when analyzing such diagrams. See text for details.

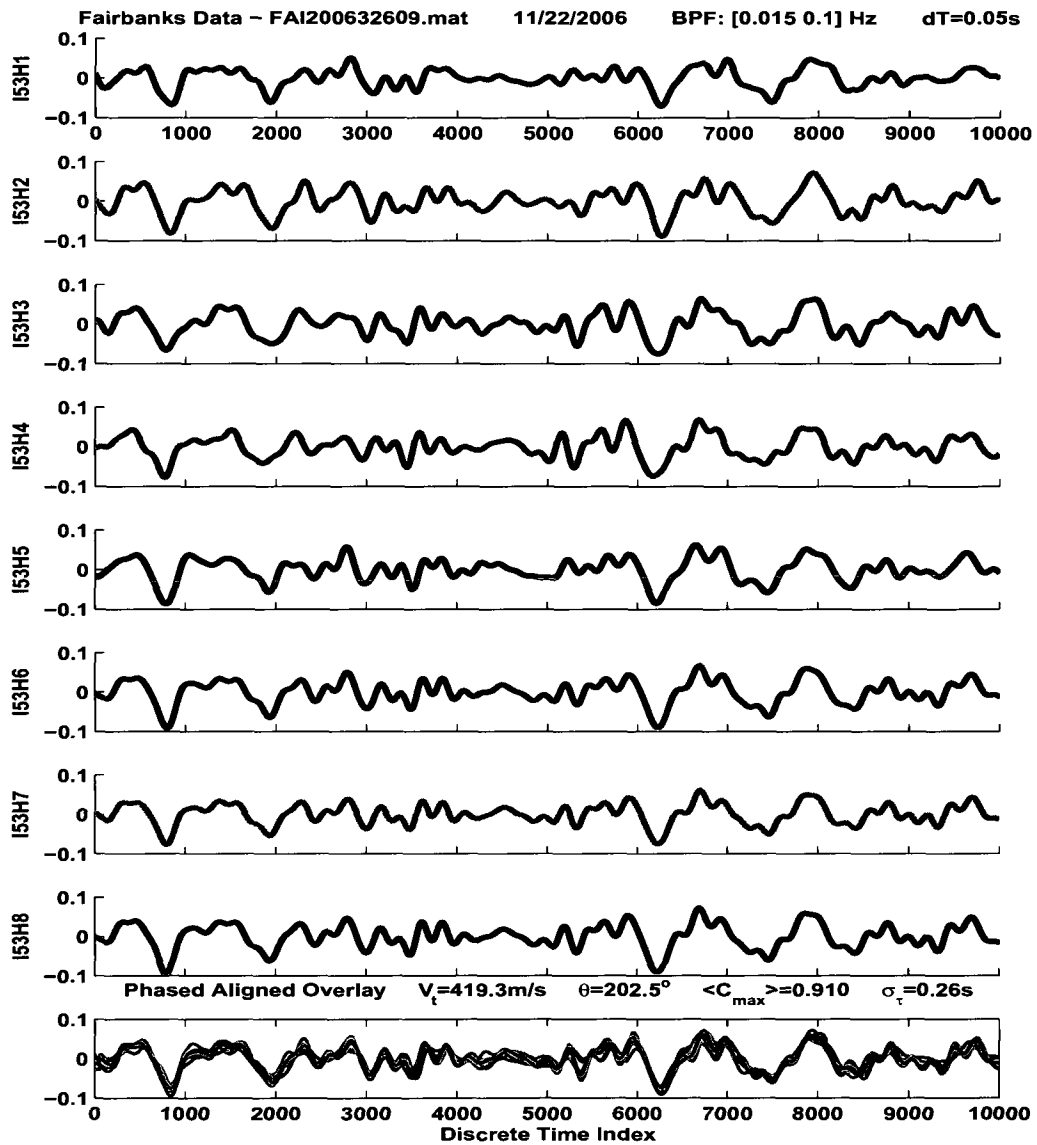


Figure 2.8. Example of MAWs observed at I53US on November 22, 2006. The data are bandpass filtered from 0.015 to 0.1 Hz to remove microbaroms and high-frequency signals. The figure is as for Fig. 2.1. Notice the irregular waveform, which is a characteristic of the MAWs.

of the power spectrum vary among the MAWs (from our experience). If we could identify unique frequencies in the spectrum and such frequencies are distinctly different from those in the spectrum of the HTVs, it would be trivial to separate the two types of signal. Unfortunately, this is not the case and we need a different technique to classify the MAWs from HTVs.

Fig. 2.10 is a detection summary plot of the MAWs at the Fairbanks array on November 22, 2006. The summary plot is as for Fig. 2.5 except the threshold of σ_r . The data are band-pass filtered from 0.015 to 0.1 Hz, in order to remove microbaroms and high-frequency signals. Thresholds for the F-stat and the MCCM are 5 and 0.6, respectively (refer to Section 3.3). The figure format is as for Fig. 2.5. Strong MAW activity is observed from 4:00 to 18:00 UT with an azimuth directed toward the Alaska and Aleutian Ranges. Notice the persistence in the V_i and θ that are characteristics of the MAWs.

2.4.2 High Trace Velocity Signals

As previously defined, high trace velocity signals are a subgroup of low-frequency signals with trace velocities higher than 650 m/s. We suspect that the HTVs originate from non-ground sources often with a source mechanism of auroral activity. Wilson [37, 38, 39] has shown that the lateral supersonic motion of auroral electro-jet currents can produce auroral infrasonic wave (AIW), and the auroral electro-jet motion can be traced by analyzing the associated infrasound signals. Pulsating aurora is named after repetitive intensity modulation in aurora luminosity, and it is known to generate pulsating auroral infrasonic wave (PAIW) which is classified as another type of the HTVs. The frequency coherence study (using pulsating aurora images from the all sky camera and infrasound data taken near the same period) by Wilson and Olson [41, 42] suggests that the pulsating auroras can produce PAIW.

Fig. 2.11 shows an example of high trace velocity signals observed around 16:00 UT at the Fairbanks array on August 19, 2006. The data are band-pass filtered from 0.015 to 0.1 Hz to remove microbaroms and high-frequency signals. The figure is as for Fig. 2.1, and

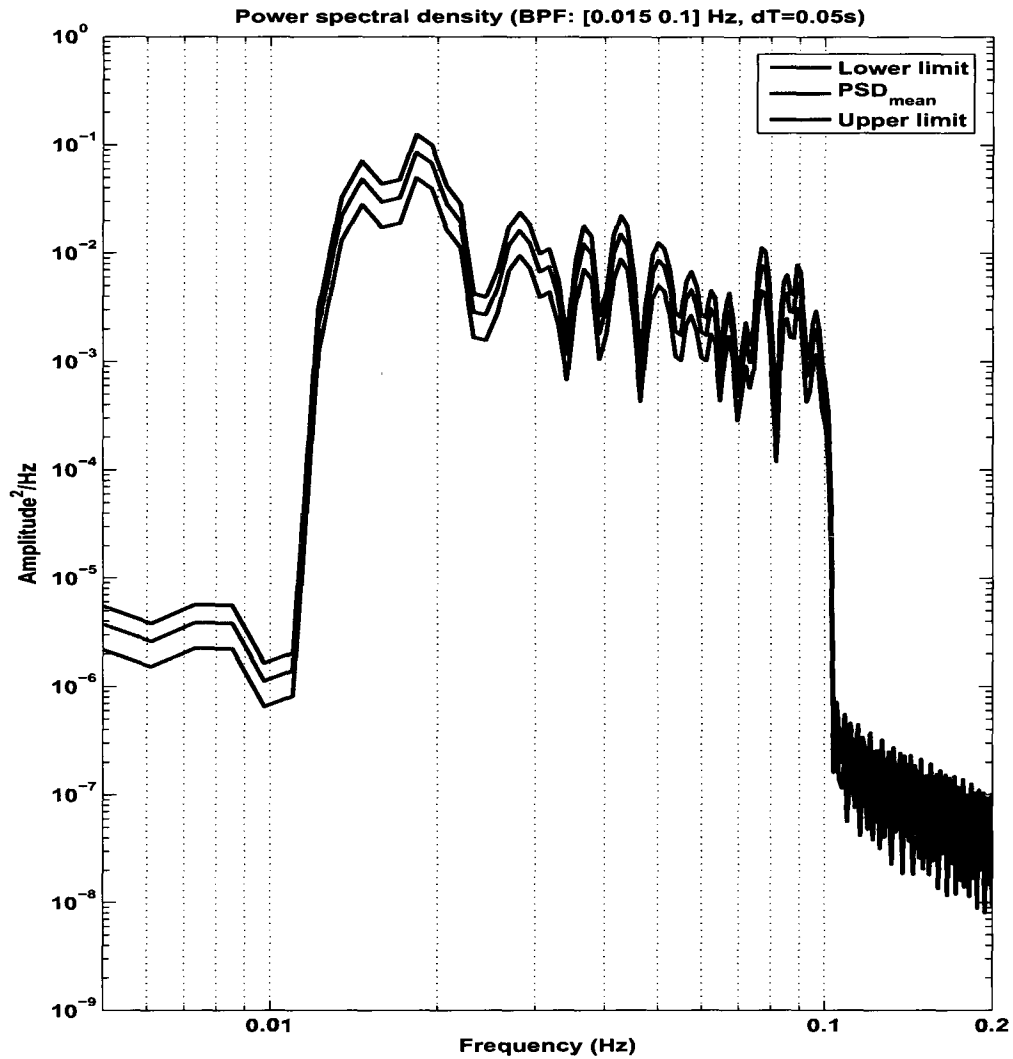


Figure 2.9. PSD of the MAWs (in Fig. 2.8). The PSD and its error bars are computed same way, as in Fig. 2.2. Reduced frequency range (0.005-1.0 Hz) is used to show details of the spectrum. It is evident that isolating unique frequencies responsible for local peaks is a difficult task due to uncertainties in the spectrum. See text for details.

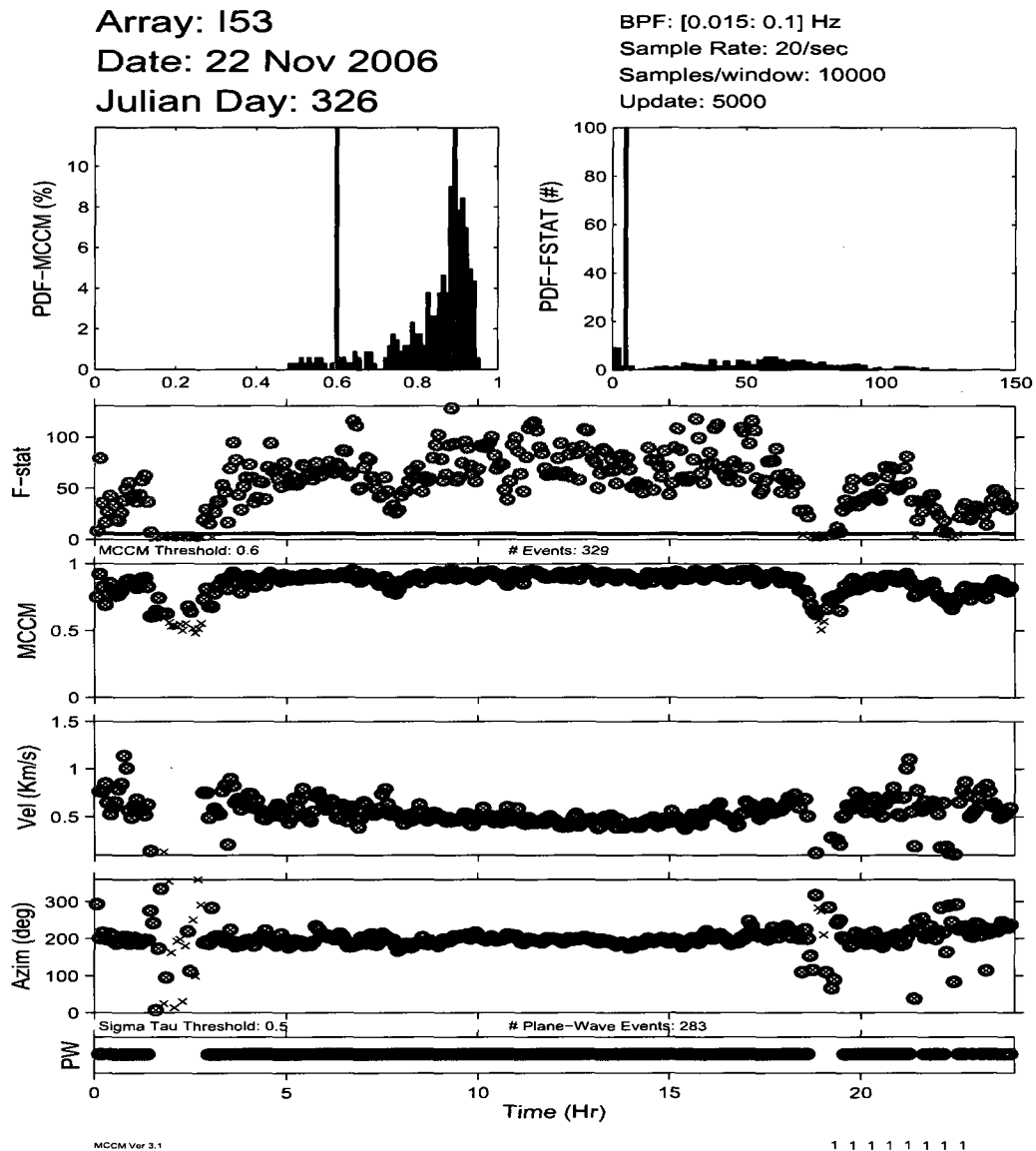


Figure 2.10. Detection summary plot of MAWs at I53US on November 22, 2006. The summary plot is as for Fig. 2.5 except the data are bandpass filtered from 0.015 to 0.1 Hz, in order to remove microbaroms and high-frequency signals. Thresholds for the F-stat and the MCCM are 5 and 0.6, respectively (refer to Section 3.3). Strong MAW activity is observed from 4:00 to 18:00 UT with an azimuth directed towards the Alaska and Aleutian Ranges. Notice the persistence in the V_t and θ that are characteristics of the MAWs.

the waveforms are impulsive and irregular. From our experience, typical AIW is impulsive in waveform and its modulated amplitude is nearly sinusoidal. Notice that the maximum peak-to-peak amplitude (0.7 Pa) in this figure is approximately seven times larger than that (0.1 Pa) in Fig. 2.8. The MCCM value of 0.959 indicates that the HTVs are highly correlated across the array. The V_t , θ , and σ_τ values of the HTVs are 718.8 m/s, 314.9°, and 0.4 seconds. The V_t and σ_τ values (with Eqs. 1.19 and 1.20) suggest that the plane wave arrived at the array at an elevated angle (ϕ) with respect to the plane of microphones. The possible source of the signal might be the lateral supersonic motion of the electro-jet current or pulsating auroras.

Fig. 2.12 shows the mean PSD (green curve) of the HTVs shown in Fig. 2.11 and its error bars at a 90% confidence level (blue and red curves) in log-log scale. The PSD and its uncertainties are as for Fig. 2.9. The overall shape of the spectrum is slightly different from that given in Fig. 2.9. The power at frequencies between 0.015 and 0.1 Hz roughly decreases exponentially with increasing frequency. Notice that the power at lower frequencies (roughly < 0.3 Hz) in Fig. 2.12 is significantly higher than that of the MAW spectrum described in Fig. 2.9. The first local peak in the spectrum is near 0.017 Hz and the uncertainty in the peak approximately runs between 1 and 20. For other local peaks in the spectrum, it is quite difficult to extract unique frequencies responsible for them due to large error bars. From our experience, power distribution and shapes of the spectrum can vary significantly from one to another. Therefore, it is not reliable to use the power spectrum to classify the HTVs from MAWs. That is the main reason why we use the trace velocity to discriminate the MAW events from HTV events (refer to Section 1.7).

As discussed before, a primary sources of the HTVs are auroras and we have used images from the all-sky camera to study the correlation between auroras and the HTVs. Unfortunately, most of those images become useless during winter months when auroras become active (due to cloudy sky). It is well-known observational fact that auroral activity is followed by magnetic disturbance in the Earth's atmosphere. Fortunately, College International Geophysical Observatory (CIGO), which is located near Fairbanks, Alaska

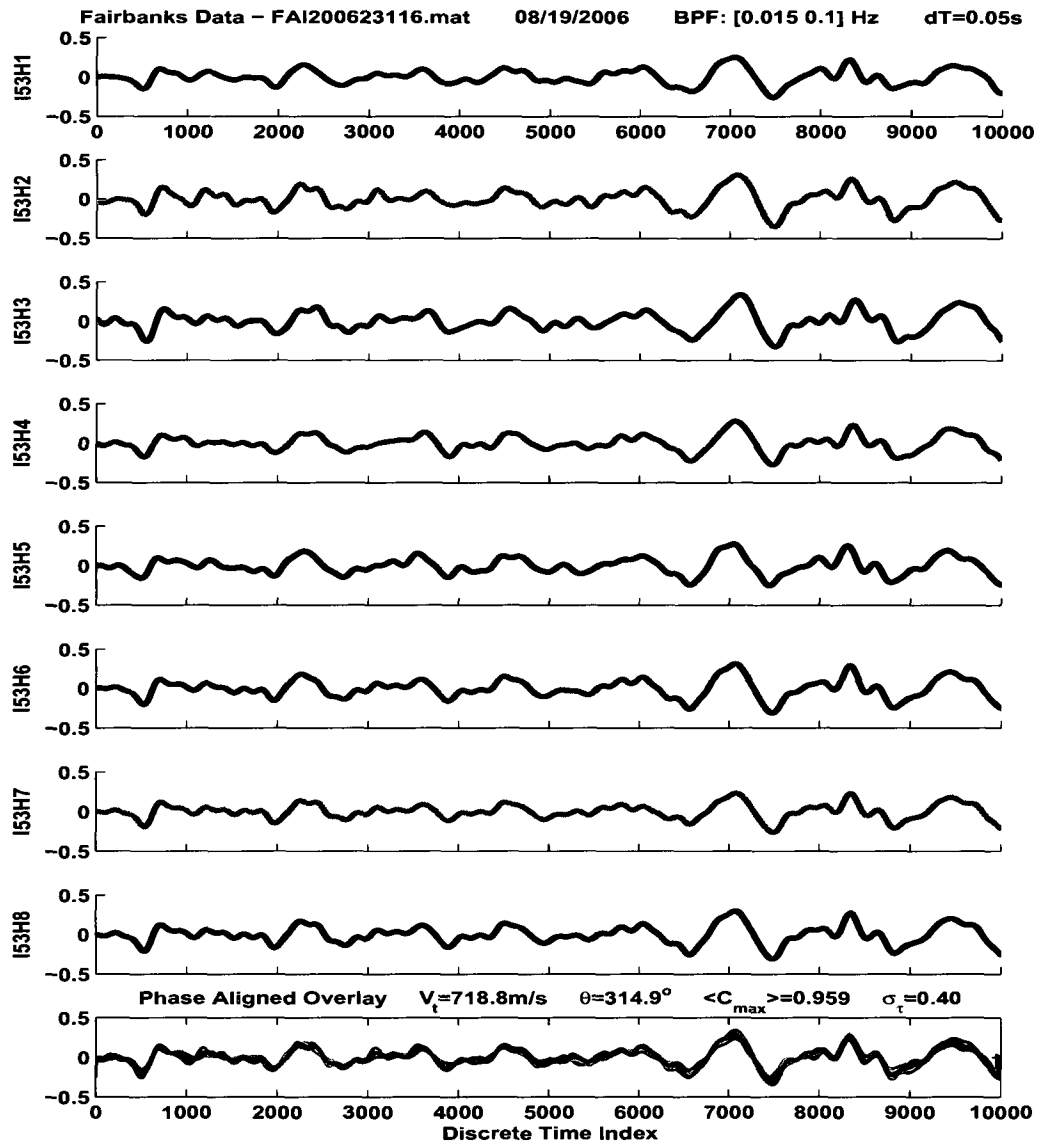


Figure 2.11. Example of HTVs observed at I53US on August 19, 2006. The data are band-pass filtered from 0.015 to 0.1 Hz to remove microbaroms and high-frequency signals. The figure is as for Fig. 2.8. Notice the impulsive and irregular waveforms, which are characteristics of the HTVs. From our experience, typical AIW is impulsive in waveform and its modulated amplitude is nearly sinusoidal. The possible source of the signal might be the lateral supersonic motion of the electro-jet current or pulsating auroras. See text for details.

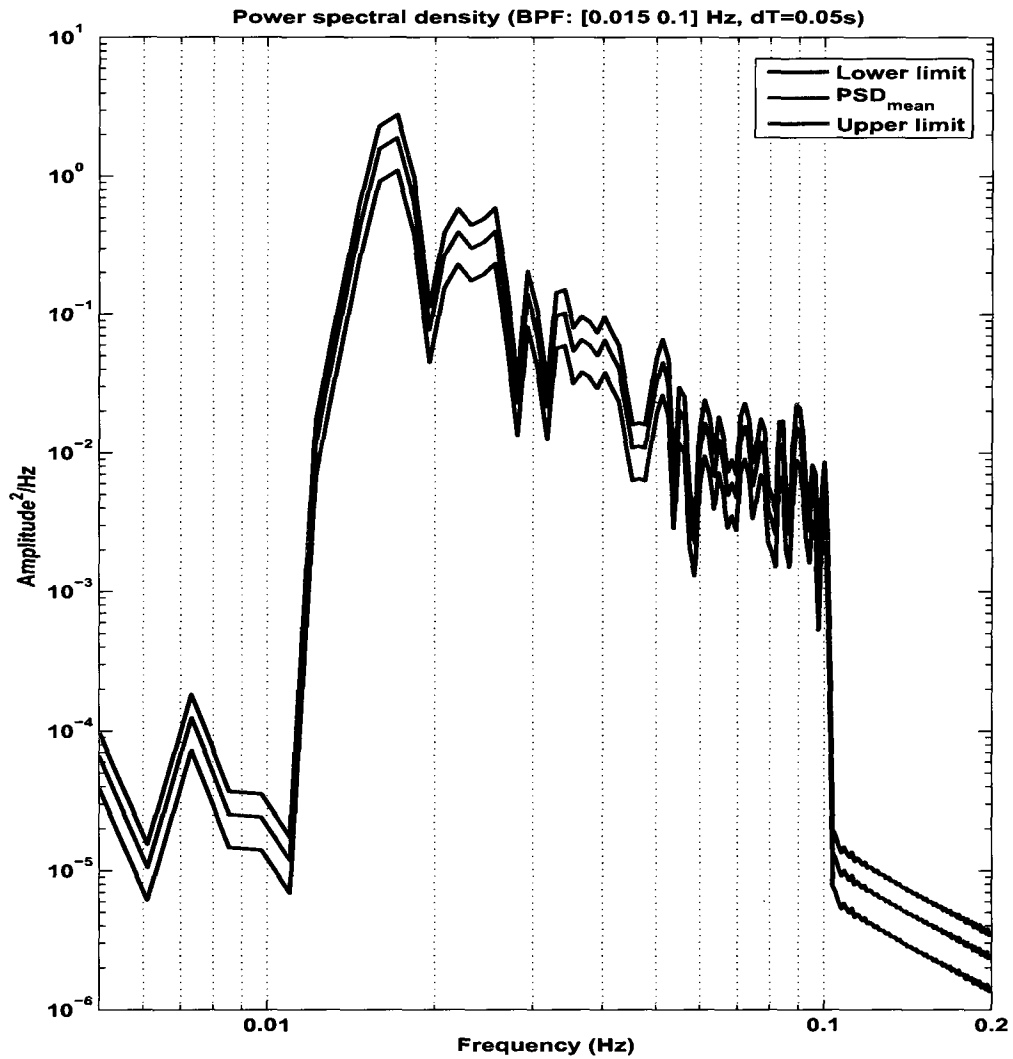


Figure 2.12. PSD of the HTVs (in Fig. 2.11). The PSD and its error bars are computed same way, as in Fig. 2.9. Reduced frequency range (0.005-1.0 Hz) is used to show details of the spectrum. It is evident that isolating unique frequencies responsible for local peaks is a difficult task due to uncertainties in the spectrum. See text for details.

to measure local magnetic variation in the atmosphere [43]. We can use such variation to identify possible sources of the HTVs detected by the detection summary plot. Fig. 2.13 is a detection summary of the HTVs observed at the Fairbanks array on August 19, 2006. The summary plot is as for Fig. 2.10, and highly correlated HTVs are observed from 12:00 to 18:00 and 20:00 to 22:00 UT. They are recorded as plane waves, have two nearly persisting azimuths, and their V_t values are distributed sporadically between 600 to 1,500 m/s. Fig. 2.14 shows magnetic variations recorded at the CIGO on the same day. Each component is measured in nT, and the mean of each component is subtracted from each time series to show details. We observe strong magnetic disturbances during the same period (from 12:00 to 22:00 UT). Such a comparison is used by our group to infer the relationship between the observed HTVs and auroral activity. Notice that the sporadic distribution of V_t which is a characteristic of the HTVs.

2.5 Summary

In this chapter we introduced four types of infrasound signals (including waveforms and PSDs) commonly observed at the Fairbanks and Antarctic arrays: mine blasts (0.5-10 Hz), microbaroms (0.1-0.5 Hz), MAWs, and HTVs (0.015-0.1 Hz). As we mentioned before, the detection and classification of those four signals are main responsibility of our group. Conventional detection methods (e.g. MCCM and F-Stat) suffer greatly in detection quality as the SNR decreases, and a new detection scheme (based on temporal and frequency characteristics of the signal) is introduced to ease such difficulty. In Chapter 3, three of four signals (one from each frequency group) mentioned in this chapter are used for studying detection performance under various SNRs among four detection algorithms: MCCM, F-Stat, SSVR1, and SSVR2. The comparison among four detectors is made using receiver operating characteristic (ROC) curves, and the SSVR2 detector is tested against the MCCM detector using the Fairbanks and Antarctic data in Chapter 3.

There are two nearby mines (30° and 60° measured clockwise from the geographic north) and located approximately 30 km away from the Fairbanks array. The observed

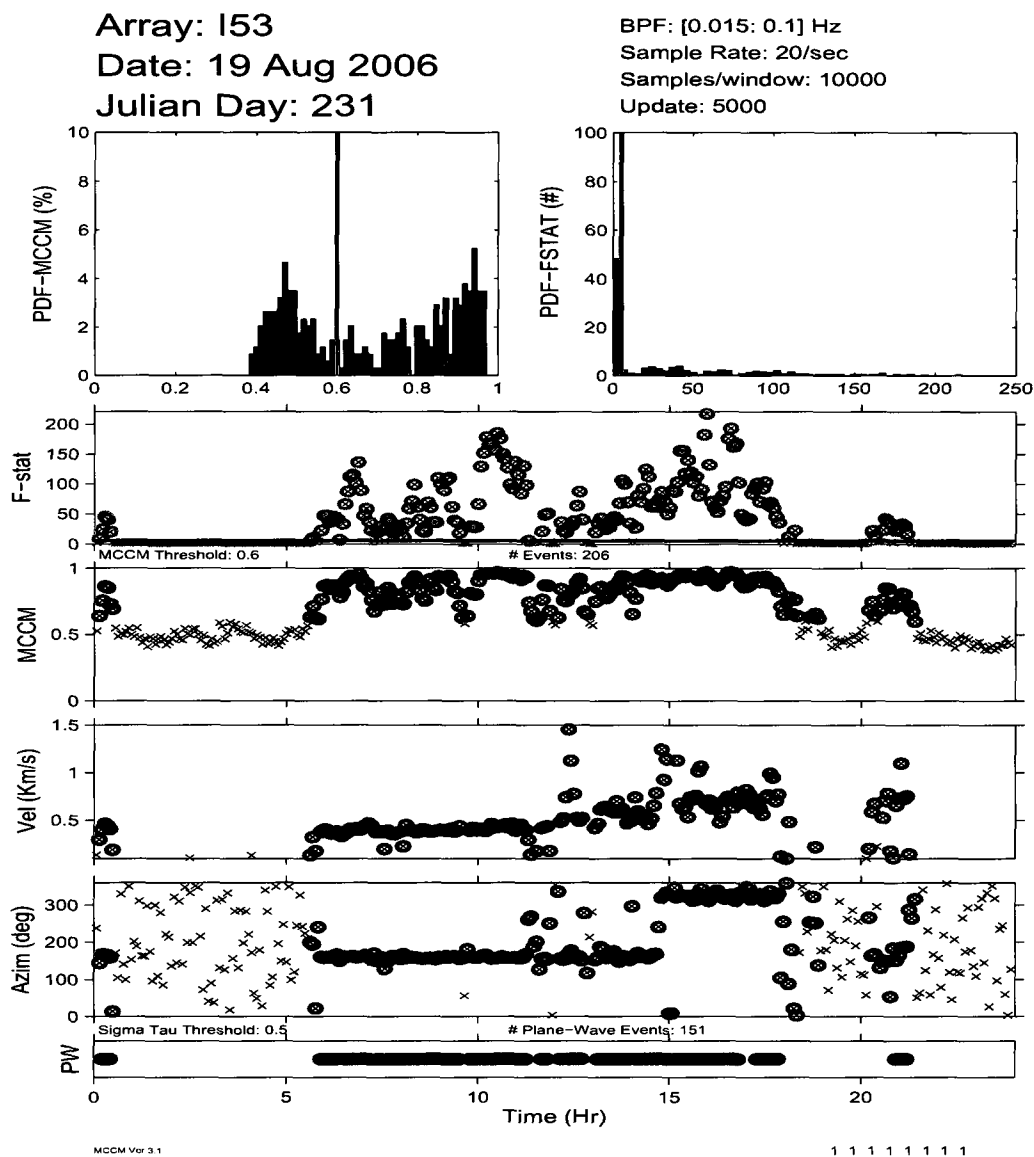


Figure 2.13. Detection summary plot of HTVs at I53US on August 19, 2006. The summary plot is as for Fig. 2.10. Thresholds for the F-stat and the MCCM are 5 and 0.6, respectively (refer to Section 3.3). Highly correlated HTV activity is observed from 12:00 to 18:00 and 20:00 to 22:00 UT. They are recorded as plane waves, have two nearly persisting azimuths, and their V_t values are distributed sporadically between 600 to 1,500 m/s. Notice the sporadic distribution of V_t , which is a characteristic of the HTVs.

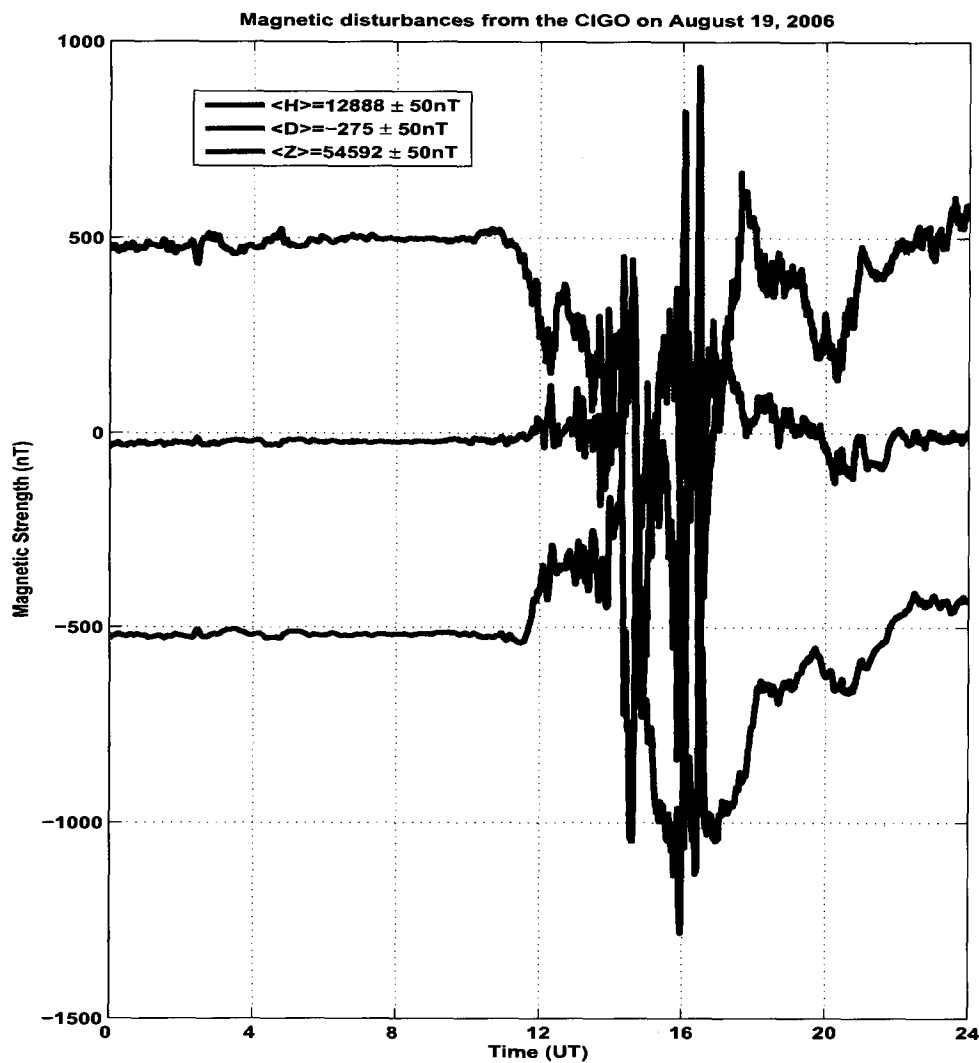


Figure 2.14. Magnetic disturbances recorded at the CIGO on August 19, 2006. Each component is measured in nT, and the mean of each component is subtracted from the time series to show details of each component. Notice a strong magnetic disturbance from 12:00 to 22:00 UT. This information can be used in conjunction with the detection summary plot to identify the possible source of the HTVs. See text for details.

signals are impulsive, and the waveforms have an "N" shape, which is a characteristic of the mine blasts. They have a broad peak near 2 Hz in the power spectrum.

The microbaroms are spatially incoherent signals produced by marine storms and characterized by nearly sinusoidal waveform packets with a period of approximately 5 seconds. There is a broad peak near 0.2 Hz and the natural width of the spectrum is a few tenths of Hz wide. The microbaroms can last for several hours. The analysis of Fairbanks array data from 2004-2007 indicates that most microbaroms come from an azimuth between 230° and 270°, which is directed toward the Bering Sea (although microbaroms originating from the Gulf of Alaska are also observed). The most active marine storms from the Bering Sea are produced during the winter months, and the microbarom activity is also highest during the same period.

In the low-frequency band, the two dominant signals are the MAWs and HTVs. The MAWs are produced by the interaction between tropospheric wind flow and mountain ranges. For the Fairbanks array, we observe the MAWs from three mountain ranges: the Saint Elias Range (110°-150°), Alaska and Aleutian Ranges (170°-230°), Seward and Chukotsk Peninsulas (275°-300°). Our group is confident with the first two mountain ranges but not certain about the third one. For the Antarctic array, principle source of MAWs is the Alps Range of South Island, New Zealand (340°-10°). The MAWs, in general, have a persistence in the azimuth, have a trace velocity less than 600 m/s, and can last for hours or even days. As described before, we have identified two types of auroral infrasound that are part of the HTVs; one is produced by the lateral supersonic motion of auroral electro-jet current and the other one is generated by pulsating auroras. The HTVs have a trace velocity greater than 650 m/s, and can have occasional persistence in the azimuth. They often have sporadic distributions in the trace velocity estimate, which is a characteristic of the HTVs. In Chapter 3, we analyze magnetic disturbance data (2004-2007) from the CIGO to identify the possible sources of the HTVs. Both the MAWs and HTVs have irregular waveforms, and their PSDs (with uncertainties at 90% confidence level) are not distinct enough from one type from another. We will therefore use trace

velocity exclusively to separate the MAWs from HTVs (refer to Section 3.3 and 3.4).

Chapter 3

Analysis of Infrasound Data

3.1 Abstract

At the beginning of this chapter we show an empirical comparison of four detectors using receiver operating characteristics (ROC) curves [66]. The four detectors include MCCM, F-stat, and the sum of squares of variance ratios (SSVR1 and SSVR2). Each detection method is applied to infrasound signals from each of the three frequency groups with varying signal to noise ratios (SNRs). We use signals described in Chapter 2 (e.g. mine blasts, microbaroms and MAWs) with two different types of noise: Gaussian white noise and pink ($1/f$) noise. Comparison of robustness (speed of execution) between the three detectors (MCCM, F-stat and SSVR2) are also included. The rest of the chapter consists of statistical studies of the MAWs and HTVs detected at the Fairbanks and Antarctic arrays for a period of four years (2004-2007). We first perform statistical analysis on various characterization parameters (MCCM, V_t , σ_τ , and SSVR2) in the low-frequency band, and determine detection thresholds for these parameters for the low-frequency signals. We then further classify the signals into two subgroups (MAWs and HTVs) based on their trace velocities (refer to Section 1.7). Different types of variational plots (azimuthal, UT, and seasonal variations) are generated to compare the MAWs with the HTVs. Some of these plots are also used to identify possible sources of the MAWs and HTVs. The UT variations of the magnetic disturbances from the CIGO are compared with those of the HTVs in order to show the correlation between the two data sets. Throughout this chapter, the SSVR2 detector is tested against the MCCM detector whenever graphically possible. Based on the selection criteria, we divide the low-frequency signals observed at the Fairbanks and Antarctic arrays into three subgroups: MAWs, HTVs, and clutter (defined here to be other than MAWs or HTVs). We will use these signals to train and validate simple neural networks in Chapter 4.

3.2 Detector Statistics: MCCM, F-stat, SSVR1, and SSVR2

The performance of a detector is a vital part of processing infrasound signals, and MCCM and F-stat are two popular detectors used by the infrasound community. The MCCM value is obtained by first computing cross correlations from all possible combinations of non-redundant sensor pairings to find the maximum correlation values and then taking the mean of all the cross correlation maxima. The Infrasound Group at the University of Alaska Fairbanks uses the MCCM to search for correlated infrasound signals across the array. The F-stat value is computed by taking the ratio of signal to noise power [67], and used by other infrasound groups. The sum of squares of variance ratios (SSVR) is a new detection method, developed for this thesis, that uses principle component analysis and covariance matrix of the power spectrum to find correlated signals. It has two versions based on the frequency range of the signal: SSVR1 for signals with frequency ranging between 1 and 10 Hz (i.e. mine blasts); SSVR2 for signals with frequency ranging between 0.015 and 0.5 Hz (e.g. microbaroms, MAWs and HTVs).

Suppose an array has N sensors and each sensor records M data points. A data matrix, \mathbf{D} , can be constructed with M rows and N columns. The SSVR1 value is obtained by taking the following steps: apply a Hamming window to each column of \mathbf{D} and compute the power spectral density (PSD); set the standard deviation of each PSD to one, and compute the covariance matrix, \mathbf{C} ($N \times N$ in size); apply eigenvalue analysis to the covariance matrix, and compute $SSVR1 = \sum_{i=1}^N (\lambda_i / \lambda_{max})^2$ where λ_i and λ_{max} are the i^{th} and largest eigenvalues of the \mathbf{C} , respectively. Unlike the MCCM and F-stat, SSVR1 operates in the frequency domain, and is equal to one for a perfectly correlated signal. Its value increases as the signal to noise ratio (SNR) decreases.

In practice, the noise PSD for infrasound follows a $1/f$ shape, and a major problem arises when applying SSVR1 to signals with frequency ranging between 0.015 and 0.5 Hz. At these low frequencies, the SSVR1 detector is more sensitive to the noise than the total signal power. For example, SSVR1 value is approximately equal to one for $1/f$ (pink) noise. The SSVR2, which is a modified version of the SSVR1, is also developed to resolve this

problem, and its value is computed by performing extra steps in addition to the SSVR1 value: set standard deviation of each column of \mathbf{D} to one, and compute the covariance matrix, \mathbf{C} ($N \times N$ in size); apply eigenvalue analysis to the covariance matrix, and compute $SSVR2 = \sum_{i=1}^N (\lambda_i / \lambda_{max})^2 + SSVR1$ where λ_i and λ_{max} are the i^{th} and largest eigenvalues of the \mathbf{C} , respectively. Unlike the SSVR1, SSVR2 uses both time and frequency information, and is equal to two for a perfectly correlated signal. As the SNR decreases, the value of SSVR2 increases.

Fig. 3.1, 3.2 and 3.3 show the performance comparison of our four detection methods against the Gaussian white noise using three well-known infrasound signals. Each figure contains four sub-figures corresponding to our four detection methods, and four detectors are compared with each other using receiver operating characteristic (ROC) curves [66]. TP and FP denote true positive and false positive signal detections (in %), respectively. Each curve is generated with 50,000 examples, and various SNRs (-3, -5, -7, -9, and -11 dB) are used. Both signal and noise are bandpass filtered according to the frequency group they belong to before computing the SNRs. In the ROC analysis, the performance depends on the shape of a curve, and the performance increases with higher TP and lower FP. For example, the MCCM detection method with SNR = -5dB (refer to Fig. 3.1) approximately gives us 20% FP and 90% TP. For the same SNR and FP values, the F-stat, SSVR1, and SSVR2 detection methods yield 20% TP, 100% TP, and 97%, respectively. We find that the SSVR1 detector outperforms (reaches to 100% TP much faster as a function of FP) the other three detectors for all SNRs. For microbaroms and low-frequency signals (See Figs. 3.2 and 3.3), the SSVR2 detector outperforms the other three detectors. For all three types of signals, the performance of F-stat detector is quite poor in comparison to the other three detectors.

Fig. 3.4, 3.5 and 3.6 show the performance comparison of our four detection methods against pink ($1/f$) noise using the three well-known infrasound signals. The pink noise closely resembles geophysical noise we receive at our infrasound stations. All three figures are as for Fig. 3.1. With the same arguments as above, the SSVR1 detector performs better

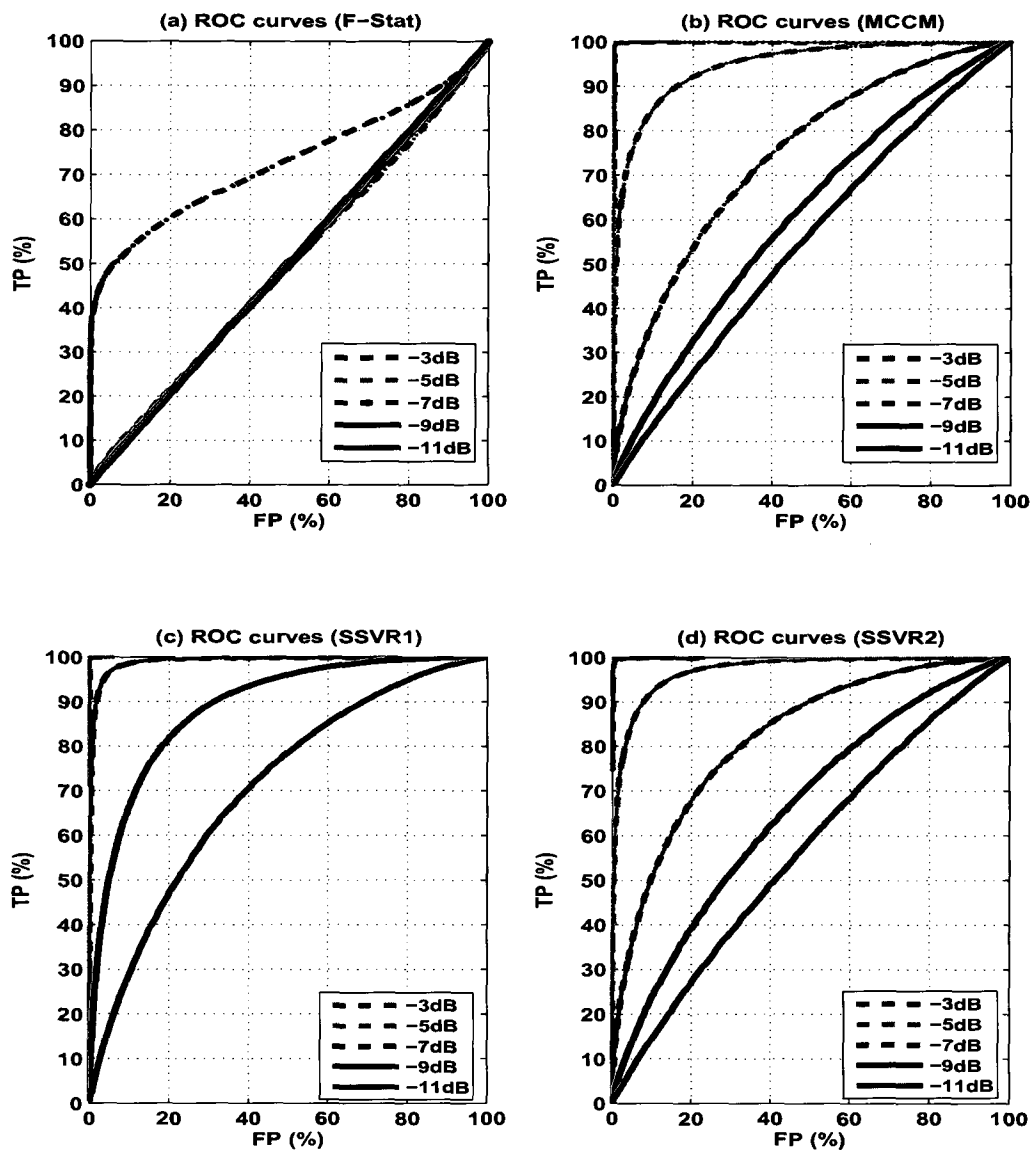


Figure 3.1. ROC analysis of the mine blasts against the Gaussian white noise. (a) F-stat detector, (b) MCCM detector, (c) SSVR1 detector and (d) SSVR2 detector. TP and FP denote true positive and false positive of signal detections (in %), respectively. In (a)-(d), each curve is generated with 50,000 examples, and various SNRs (-3, -5, -7, -9, and -11 dB) are indicated by different colors (red, green, blue, black, and magenta). Notice the performance of the SSVR1 detector over that of the other three detectors.

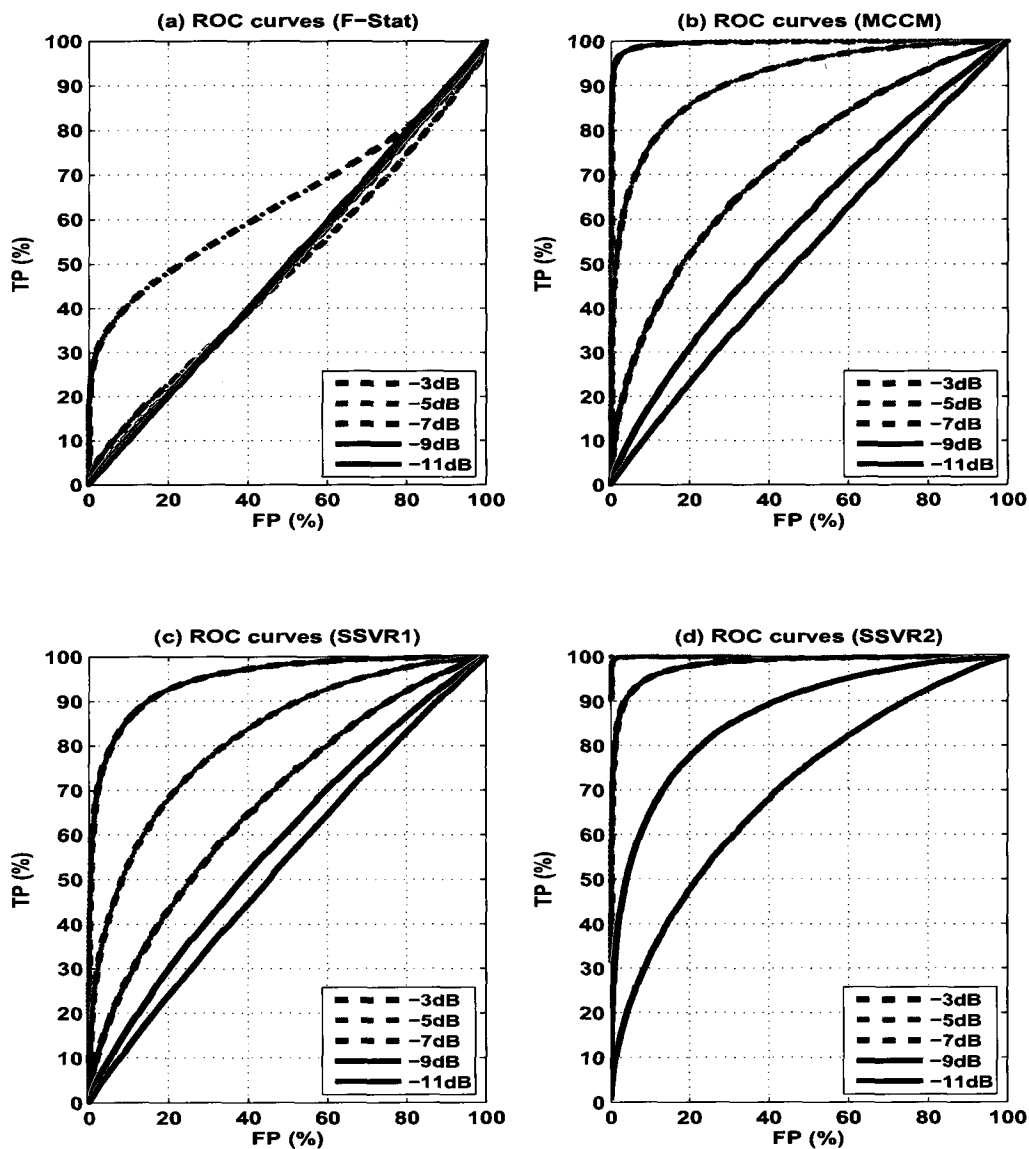


Figure 3.2. ROC analysis of the microbaroms against the Gaussian white noise. The figure is as for Fig. 3.1. Notice the performance of the SSVR2 detector over that of the other three detectors.

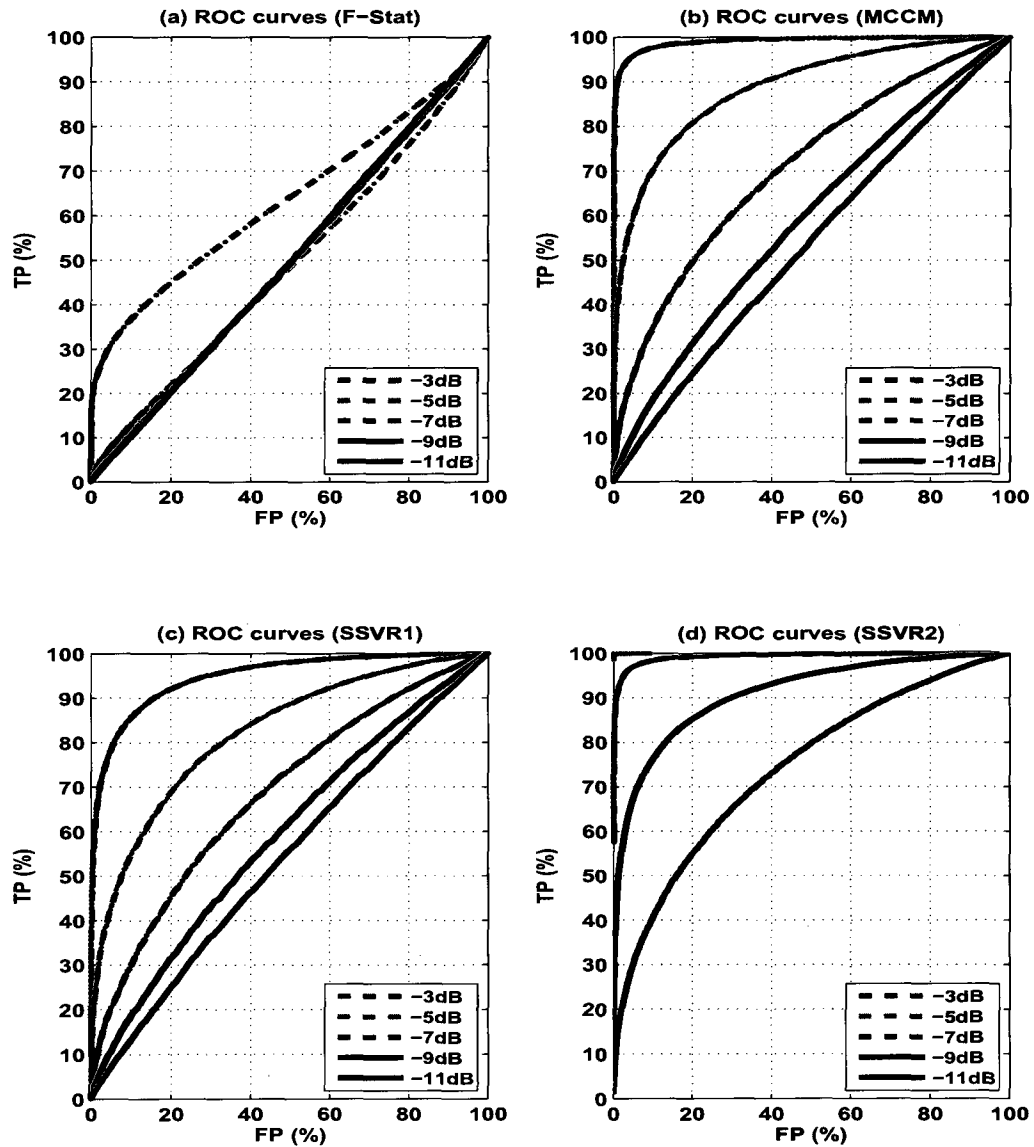


Figure 3.3. ROC analysis of the MAWs against the Gaussian white noise. The figure is as for Fig. 3.1. Notice the performance of the SSVR2 detector over that of the other three detectors.

than the other three detectors for the mine blasts, and the SSVR2 detector outperforms the other three detectors for the microbaroms and MAWs. The performance of F-stat detector is again quite poor in comparison to the other three detectors for all three types of signals. The performance of all four detectors is worse against the pink noise than the Gaussian white noise.

The real advantage of SSVR based detectors is their execution speed. Fig. 3.7 illustrates the ratios of computational times between the three detectors (MCCM Vs. SSVR2 and F-stat Vs. SSVR2), as a function of number of sensors. The computational time of the SSVR2 detector is slightly longer (roughly by a factor of 1.2) than that of the SSVR1 detector. Various colors indicate signals with different window sizes, and the computation time for the SSVR2 detector is much faster than that of the MCCM. For example, execution speed roughly increases by a factor of 20 for a signal in a window size of 1000 points (for an array with 11 sensors). The speed improvement of the SSVR2 detector is nearly exponential compared to the MCCM detector, as the number of sensors increases. The computational time of the SSVR2 detector is slower (by a factor of 3 to 7) than that of the F-stat detector. For example, an execution speed roughly decreases by a factor of 3 for a signal in a window size of 1000 points (for an array with 11 sensors). Notice that the ratio of execution times between the F-stat and SSVR2 detectors does not depend on the number of sensors.

The SSVR1 and SSVR2 detectors are very robust and efficient in detecting correlated signals; however, the MCCM must be computed in order to estimate characterization parameters (refer to Section 1.6) for correlated signals. These detectors will be invaluable for arrays with large number of sensors or infrasound stations in remote locations with a limited bandwidth (since estimated parameters, rather than data, may have to be transmitted from the site) and at low SNRs. In the following sections, we will use both the SSVR2 and MCCM detectors to analyze infrasound data sets, and show that they provide us with similar results.

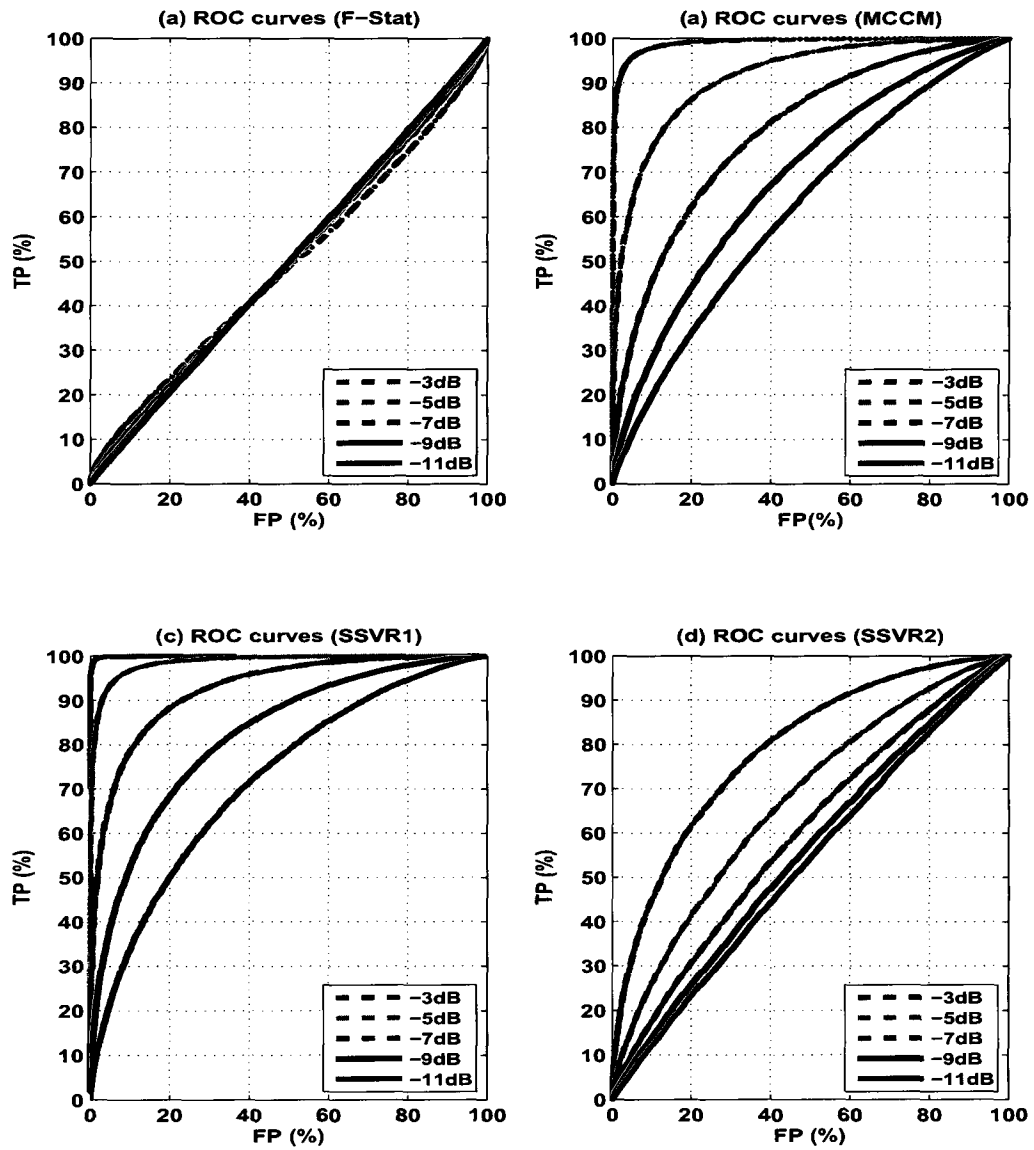


Figure 3.4. ROC analysis of the mine blasts against the pink noise. The figure is as for Fig. 3.1. Notice the performance of the SSVR1 detector over that of the other three detectors.

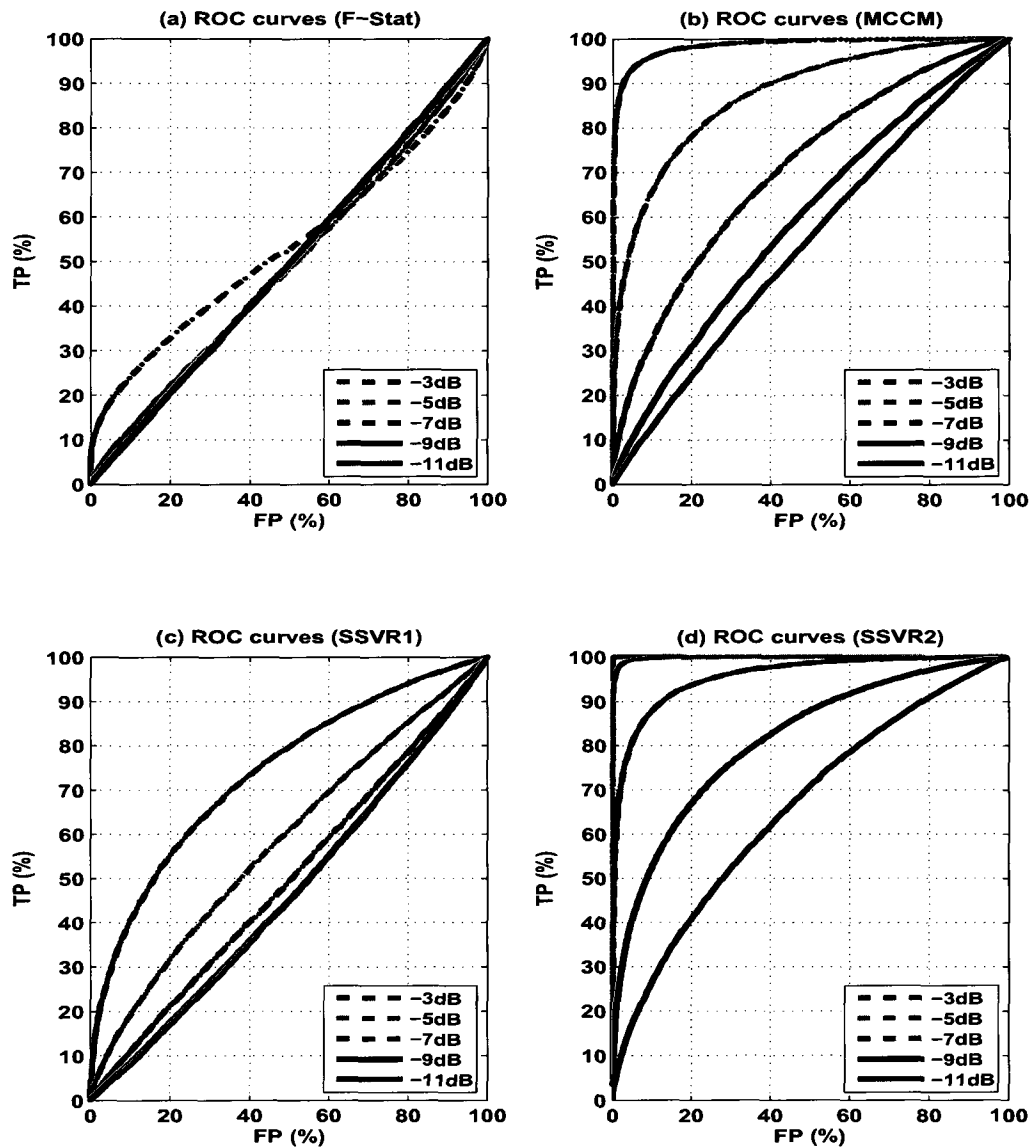


Figure 3.5. ROC analysis of the microbaroms against the pink noise. The figure is as for Fig. 3.1. Notice the performance of the SSVR2 detector over that of the other three detectors.

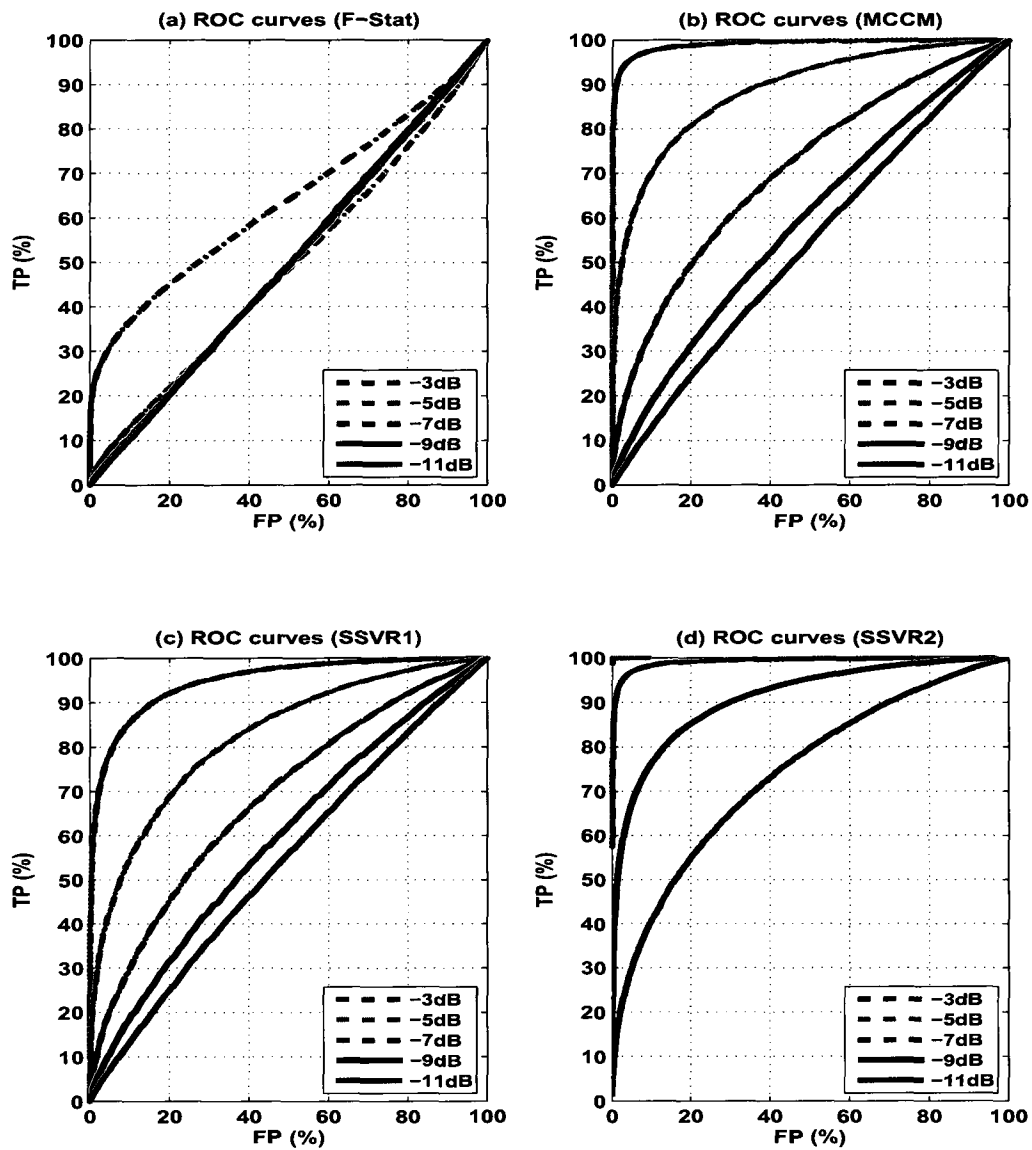


Figure 3.6. ROC analysis of the MAWs against the pink noise. The figure is as for Fig. 3.1. Notice the performance of the SSVR2 detector over that of the other three detectors.

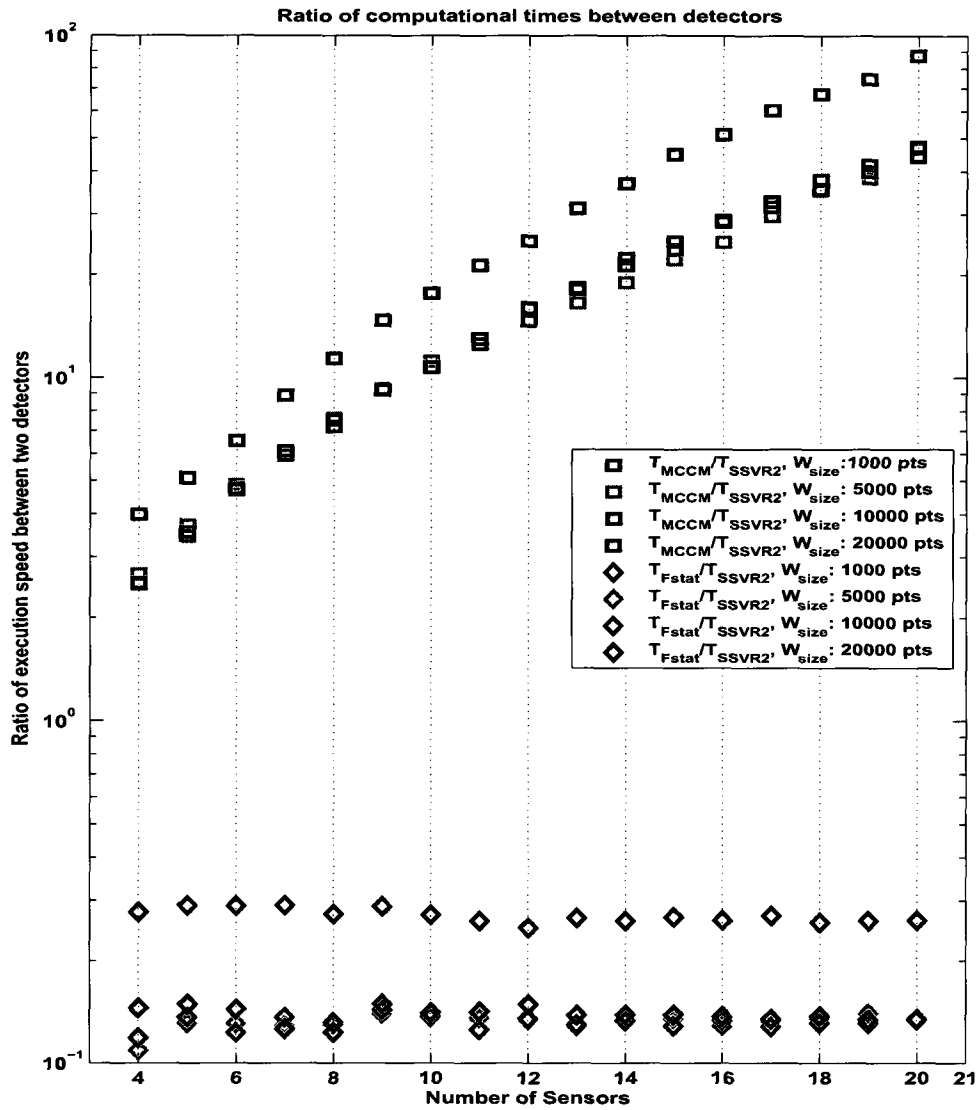


Figure 3.7. Robustness of the SSVR2 detector against the MCCM detector. Semi-log scale is used for y-axis and x-axis represents the number of sensors in an array. Various colors indicate signals with different window sizes and two different shapes represent the ratios of computational times between the three detectors. The speed improvement of the SSVR2 detector is nearly exponential compared to the MCCM detector, as the number of sensors increases. Notice that the ratio of execution times between the F-stat and SSVR2 detectors does not depend on the number of sensors.

3.3 Fairbanks Array

In this section we will first determine detection thresholds for various characterization parameters for MAWs and HTVs observed at the Fairbanks array (I53US) using a period of four years of infrasound data (2004-2007). We then generate variational plots (azimuthal, UT, and seasonal variations) for the MAWs and HTVs, and such plots are used to identify possible sources of the MAWs and HTVs.

The quality of detection and classification of infrasound signals heavily depends on the threshold values and thus estimation of thresholds for the characterization parameters (MCCM, SSVR2, V_t , and σ_τ) is a critical part of the detection and classification of infrasound signal. Based on computer simulations, distributions of the four characterization parameters for both white and pink noise (band pass filtered from 0.015 to 0.1 Hz) roughly follow Gaussian shape (refer to Fig. 3.8), but we note that V_t is skewed positive. As you can see from the figure, values for each of the three parameters (MCCM, V_t , and σ_τ) are clustered roughly around the same mean value for both white and pink noise. The SSVR2 is more sensitive to the pink noise than white noise. For perfectly correlated signals, we expect values of the MCCM, SSVR2, and σ_τ to be one, two, and zero. As a result, each of the three parameters for the correlated signals and noise would be clustered around different mean values. If we assume that there are two distribution curves (for correlated signals and noise) in the data set, the thresholds can be estimated by finding a region of zero slope between the two distribution curves to minimize overlap of the two curves in each of the parameter histograms. The lower and upper limits of the V_t are set at 0.3 and 1.5 Km/s, respectively (refer to Section 1.6).

Fig. 3.9 shows histograms of estimated parameters (MCCM, SSVR2, V_t , and σ_τ) for all available infrasound data between January, 2004 and December, 2007 from the Fairbanks array. Each parameter is estimated by taking the following steps: first, concatenate hour long data sets to form a three hour long data set by appending the hour before and the hour after to the hour of interest; second, apply a bandpass filter from 0.015 to 0.1 Hz in order to remove microbaroms and high-frequency signals; third, select the middle hour

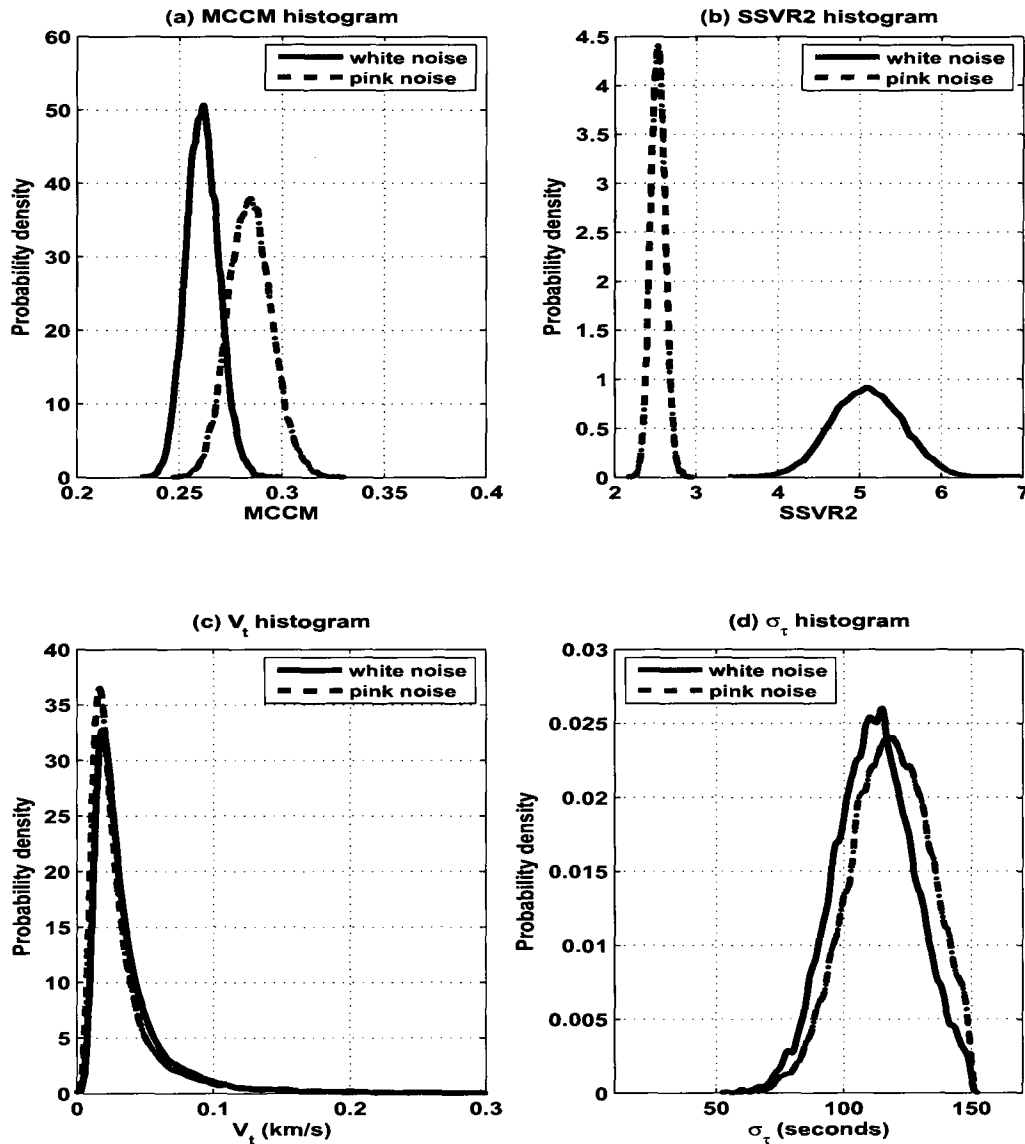


Figure 3.8. Histogram of characterization parameters for the Gaussian and pink noise. Both types of noise are band-pass filtered from 0.015 to 0.1 Hz prior to computing the parameters. (a) MCCM histogram, (b) SSVR2 histogram, (c) V_t histogram and (d) σ_τ histogram. Except (c), other parameters display roughly normal distribution. In (b), the SSVR2 parameter is more sensitive to the pink noise than white noise. For perfectly correlated signals, we expect values of the MCCM, SSVR2, and σ_τ to be one, two, and zero. The lower and upper limits of the V_t are set at 0.3 and 1.5 Km/s, respectively (refer to Section 1.7).

Table 3.1. Parameter selection criteria for MAWs, HTVs and clutter at I53US.

MAWs	HTVs	clutter
MCCM > 0.7	MCCM > 0.7	MCCM < 0.7
SSVR2 < 2.7	SSVR2 < 2.7	SSVR2 > 2.7
$\sigma_\tau < 3.5$ s	$\sigma_\tau < 3.5$ s	$\sigma_\tau > 3.5$ s
$0.3 < V_t < 0.6$ Km/s	$0.65 < V_t < 1.5$ Km/s	$0 < V_t < 1.5$ Km/s

section to avoid ringing at the edges and estimate the characterization parameters for a sliding window that is 10,000 points (or 500 seconds) long with 50% overlap. The top left plot of the figure is the probability density of the MCCM detector, and the threshold for the signal detection is set at 0.7, since that is the value between the assumed signal and non-signal distributions where the curve has zero slope. The top right panel of the figure shows the probability density of the SSVR2 detector, and the threshold for the signal detection is set at 2.7. The second panel from the bottom to top of the figure depicts the probability density of the V_t , and the lower and upper limits of the V_t are set at 300 and 1500 m/s. The bottom plot of the figure depicts the probability density of the σ_τ , and the threshold for a plane wave arrival is set at 3.5 seconds. In each of the histograms, shaded area displays the region of signal detection, and areas under all histograms in this chapter are normalized to one. In the σ_τ histogram, there is a small distribution curve ($3.5 < \sigma_\tau < 15$ seconds). These unknown signals are correlated (MCCM value is clustered around 0.75) but they travel at sub-acoustic speed (clustered around 160 m/s). Since we do not know the source of these signals we ignore them in this thesis. From the MCCM and SSVR2 histograms, we see that only a small fraction of the received signals are highly correlated across the array. We summarize the parameter selection criteria for the Fairbanks array in Table 3.1.

Detected signals are classified into three groups (MAWs, HTVs, and clutter) based on their parameter values (see Table 3.1). For the signals of interest (MAWs and HTVs), signals should be highly correlated (MCCM > 0.7 or SSVR2 < 2.7) and have acoustic speed

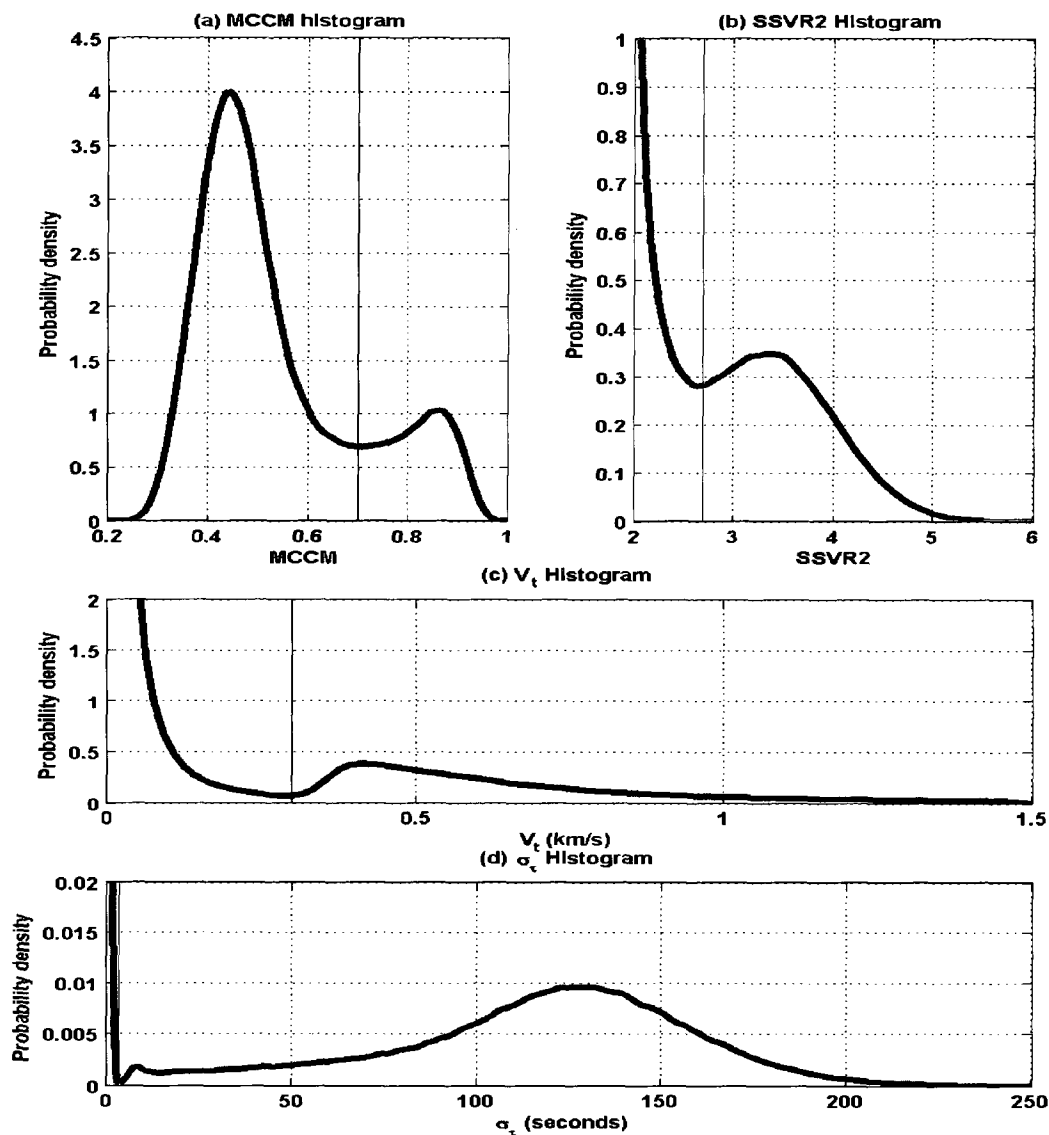


Figure 3.9. Histograms of characterization parameters at I53US (2004-2007). (a) MCCM histogram, (b) SSVR2 histogram, (c) V_t histogram and (d) σ_τ histogram. The shaded area represents the region of signal detection. From the MCCM and SSVR2 histograms, we see that only small fraction of received signals are highly correlated across the array. See text for details.

($0.3 < V_t < 1.5$ Km/s). They should also propagate the array as a plane wave parallel to the ground ($\sigma_\tau < 3.5$ seconds). The MAWs and HTVs are separated based on their trace velocity values (refer to Section 1.7). The clutter includes noise as well as unknown signals, and generally have low correlation values ($MCCM < 0.7$ or $SSVR2 > 2.7$) and propagate the array as non-plane waves ($\sigma_\tau > 3.5$ seconds). Their lower and upper V_t limits are 0 and 1.5 km/s, respectively. To illustrate the effectiveness of the SSVR2 detector, its performance is compared with the performance of the well-known MCCM detector throughout this chapter.

We now search for events with parameters that exceed their thresholds from the Fairbanks data (for the period 2004-2007) and construct a total of six histograms: azimuthal, UT, and seasonal variations based on the two detection algorithms. Plots in the left column of Fig. 3.10 are generated with $MCCM > 0.7$, $\sigma_\tau < 3.5$ seconds, and $0.3 < V_t < 1.5$ Km/s. Plots in the right column of the figure are produced with $SSVR2 < 2.7$, $\sigma_\tau < 3.5$ seconds, and $0.3 < V_t < 1.5$ Km/s. Based on the selection criteria, we expect to detect both MAWs and HTVs. The azimuthal variations roughly show three directional bands: 120° - 160° , 170° - 240° , and 250° - 300° . There is a global peak around 15:00 UT in the UT variations, and the seasonal variations show that both MAWs and HTVs are active from October to March and quiet from April to September. Both MCCM and SSVR2 detectors produce similar results.

We use the trace velocity to separate the HTVs from MAWs (see Fig. 3.11). The azimuthal (θ) histogram of Fig. 3.10 (top left plot) is divided into MAW and HTV groups based on the V_t estimate. The red curve indicates MAWs, which coincide with the three mountain ranges in Alaska: the first two peaks correspond to the Saint Elias Range (110° - 150°) and Alaska and Aleutian Ranges (170° - 230°); we suspect that is from the Seward and Chukotsk Peninsulas (275° - 300°). The blue curve represents HTVs, which show negligible directional dependence, but there is some leakage in that it is possible that some detections are masquerading as the HTVs.

We find that the azimuthal variations of MAWs have similar directional dependences

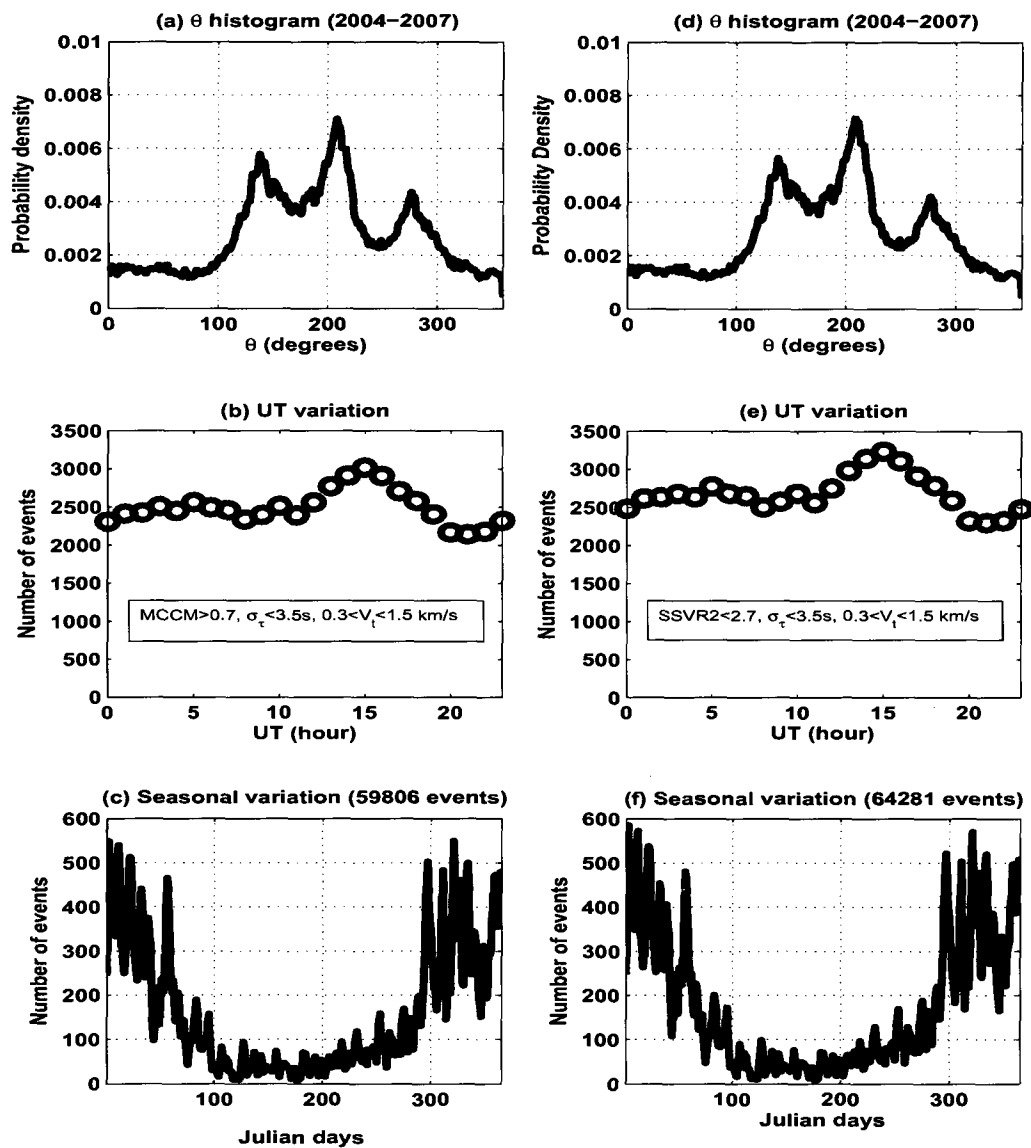


Figure 3.10. Variational plots of low-frequency signals detected at I53US. (a) θ histogram, (b) UT variation, (c) seasonal variation, (d) θ histogram, (e) UT variation and (f) seasonal variation. (a)-(c) are based on the MCCM detector and (d)-(f) are based on the SSVR2 detector. Notice that both MCCM and SSVR2 detectors produce similar results. The MAWs and HTVs are active from October to March and quiet from April to September. See text for details.

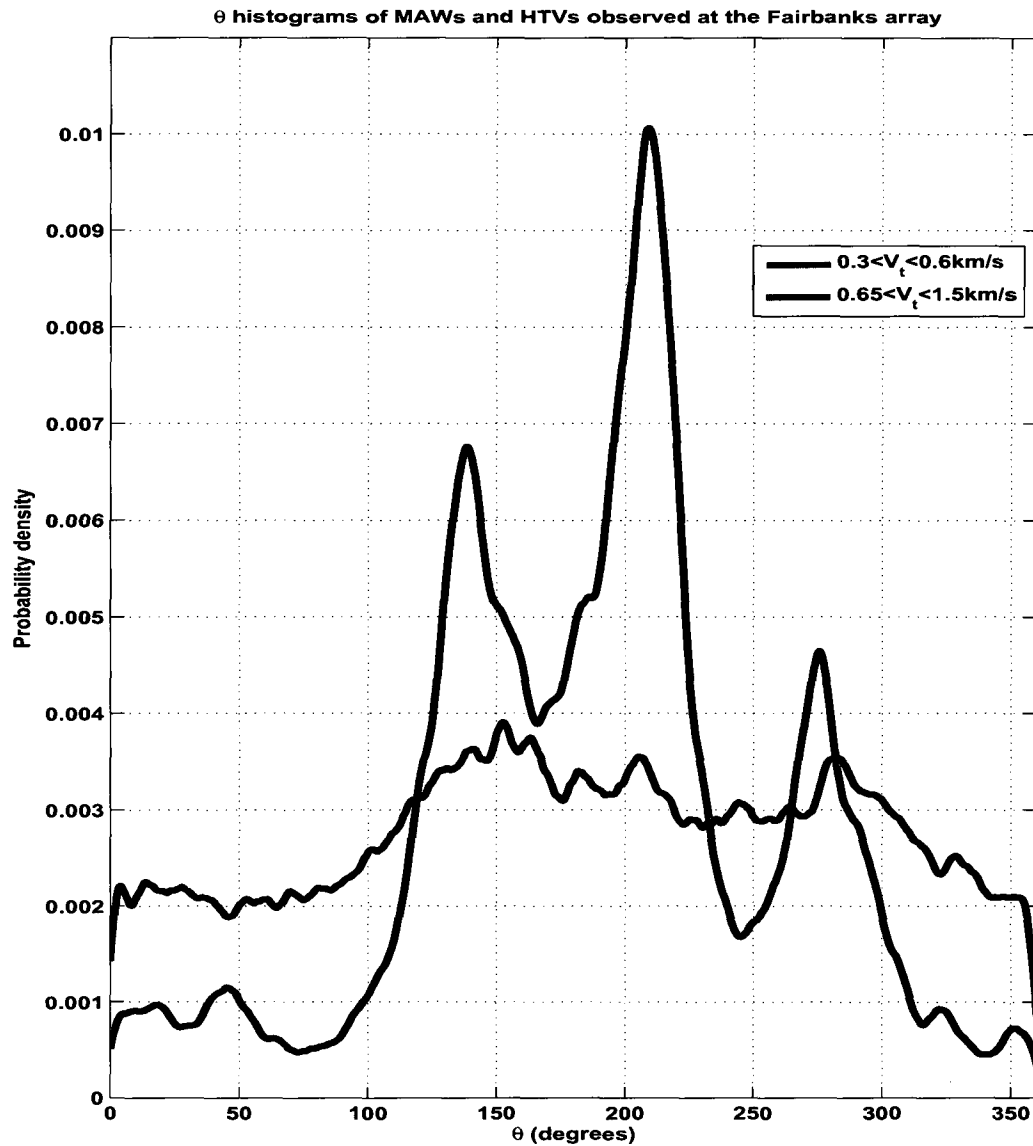


Figure 3.11. θ histograms of the MAW and HTV events at I53US. The red curve indicates MAWs, which coincide with the three mountain ranges in Alaska: the first two peaks correspond to the Saint Elias Range (110° - 150°) and Alaska and Aleutian Ranges (170° - 230°); we suspect that the third peak is from the Seward and Chukotsk Peninsulas (275° - 300°). The blue curve represents HTVs, which show negligible directional dependence, but there is some leakage in that it is possible that some detections are masquerading as the HTVs.

for all years except year 2007 (refer to Fig. 3.12). The red and blue curves indicate MAWs and HTVs, respectively. Strong MAW activity is observed only from the Alaska and Aleutian Ranges (170° - 230°). The unique shape could be due to the missed events (propagating in different paths), or no MAW activity from the Saint Elias Range (110° - 150°) and the Seward and Chukotsk Peninsulas (275° - 300°) during 2007. The HTV curve shows negligible directional dependence, but it is possible that some detections are masquerading as the HTVs due to some leakage.

Fig. 3.13 displays UT variations of the MAW and HTV activity observed at the Fairbanks array (see Fig. 3.11) for the period 2004-2007. The blue and red circles indicate the number of HTV and MAW events detected within each hour, respectively. There is a global peak around 15:00 UT for HTVs in all UT variations, and a similar pattern is consistently observed in each year between 2004 and 2007. HTV activity is most likely to occur between 5:00 and 18:00 UT. The analysis of the magnetic data from the CIGO also shows high magnetic activity during the same period (refer to Figs. 3.14 and 3.17). We observe no correlation between the magnetic activity and the MAW activity. Unlike the pattern of HTV activity, the MAW activity does not appear to have any patterns among the four UT variations.

CIGO, located near Fairbanks, Alaska, samples magnetic data in 3-dimension at 1 Hz. Fig. 3.14 illustrates variations in H, D, and Z magnetic components for a period of four years (2004-2007). The variations of the three components are obtained by taking the following steps: first, concatenating hour-long magnetic data sets to form a 24 hour-long data set; second, compute the standard deviation of a sliding window that is 600 points (spaced 10 seconds apart) long with 50 percent overlap; finally, plotting the sum of standard deviations as a function of time. The H-magnetic component has the largest variation, and most variations for three magnetic components occur between 5:00 and 18:00 UT. All three components have the largest variations around 10:00 UT. We also looked at the variations in the H, D, and Z magnetic components for days with the standard deviation of daily H magnetic component is greater than 500 nT. The resulting variations in the three magnetic

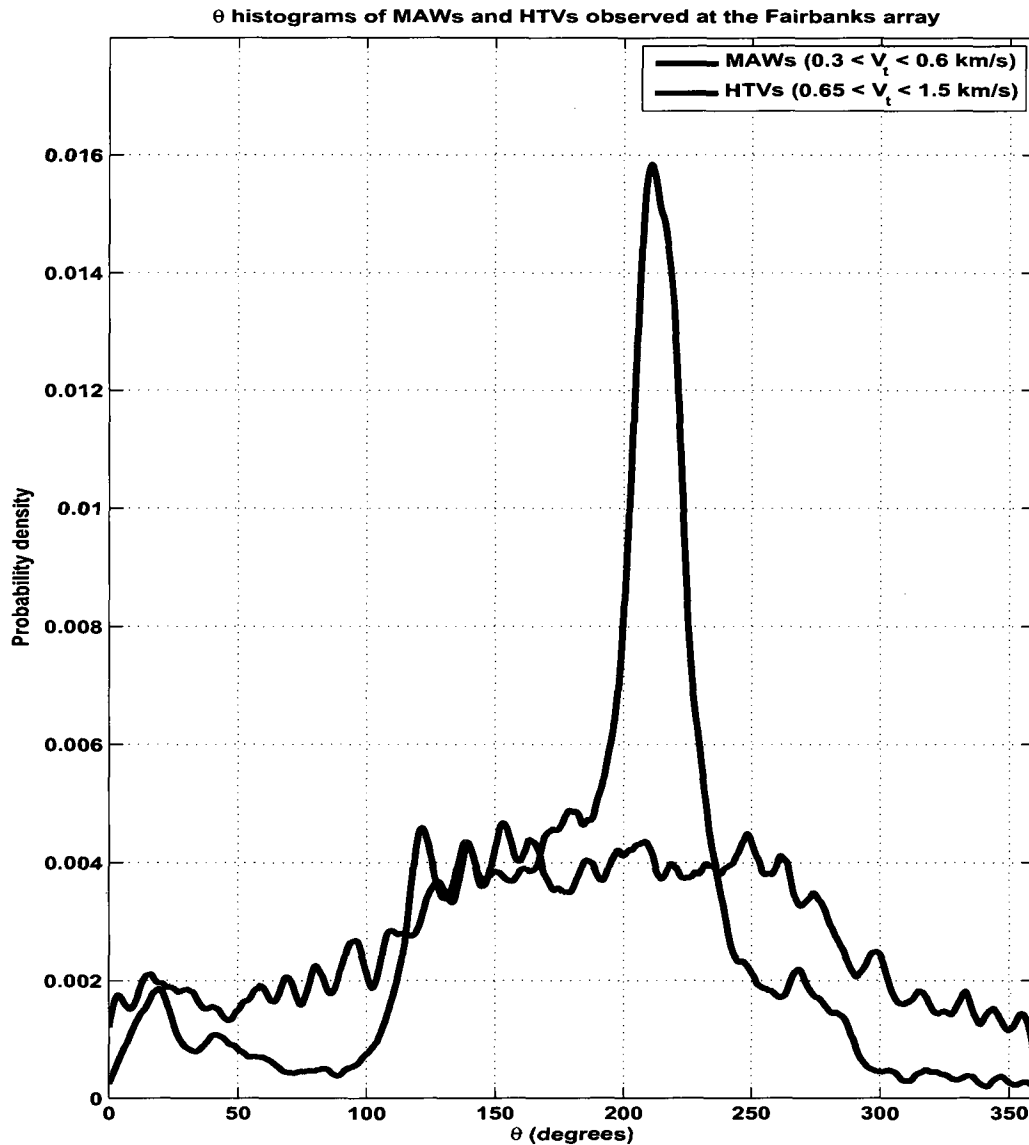


Figure 3.12. θ histograms of the MAW and HTV activity at I53US (2007). The red and blue curves indicate MAWs and HTVs, respectively. Strong MAW activity is observed only from the Alaska and Aleutian Ranges (170° - 230°). The HTV curve shows negligible directional dependence, but it is possible that some detections are masquerading as the HTVs due to some leakage.

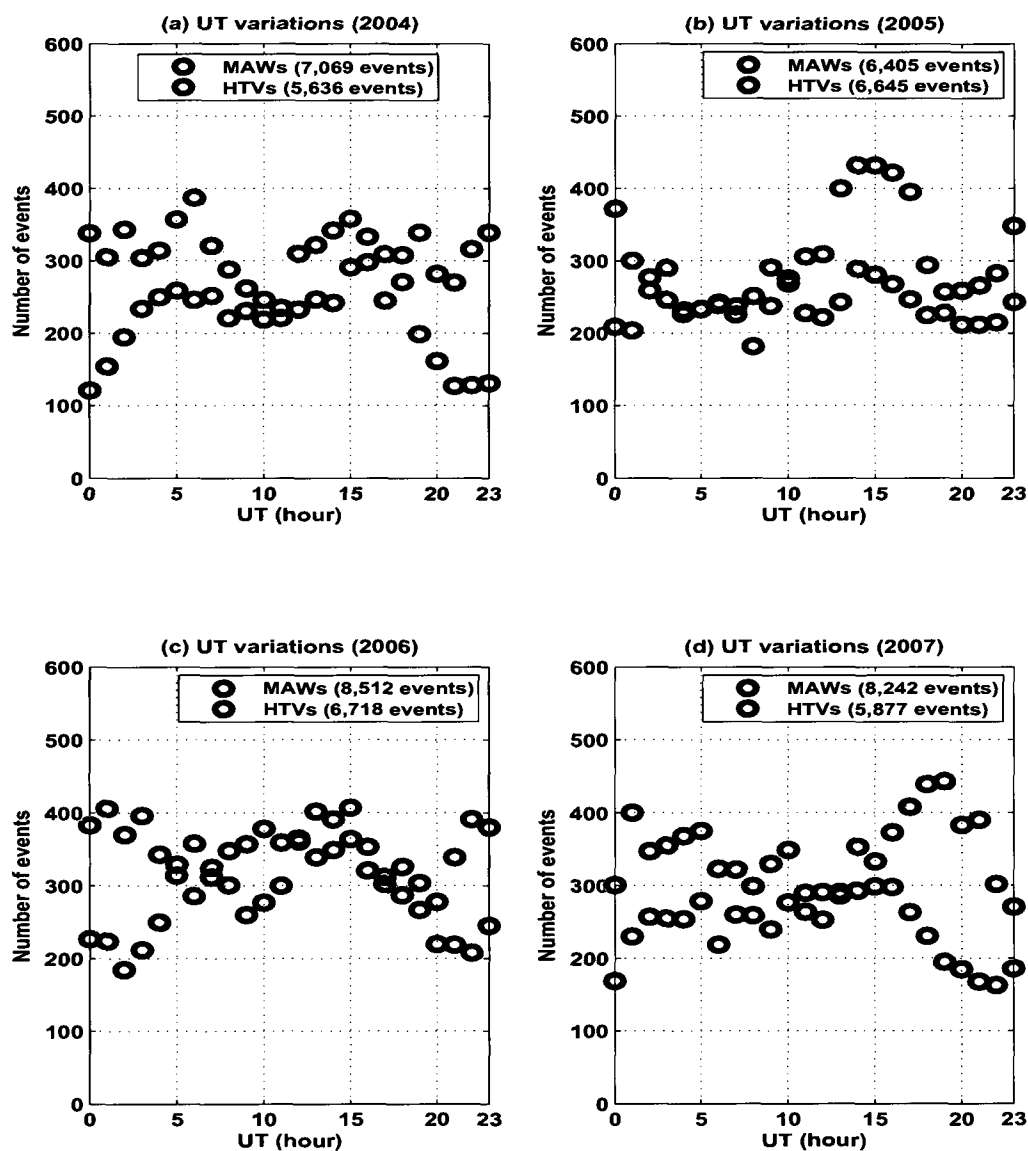


Figure 3.13. UT variations of the MAW and HTV activity at I53US (2004-2007). (a) year 2004, (b) year 2005, (c) year 2006, and (d) year 2007. In (a)-(d), the blue and red circles indicate the number of HTV and MAW events detected within each hour, respectively. There is a global peak around 15:00 UT for HTV activity in (a)-(d), and a similar pattern is consistently observed in each year between 2004 and 2007. HTV activity is most likely to occur between 5:00 and 18:00 UT. The MAW activity does not appear to have any patterns among the four UT variations.

components remain close to the original variations.

Fig. 3.15 depicts the quarterly azimuthal variations of the MAW and HTV activity observed at the Fairbanks array for the period 2004-2007. The blue and red curves represent the HTVs and MAWs, respectively. We observe MAWs from three mountain ranges in the plots of quarters one and four: the Saint Elias Range (110° - 150°), the Alaska and Aleutian Ranges (170° - 230°), possibly from the Seward and Chukotsk Peninsulas (275° - 300°). We do not observe any consistent patterns in the quarterly azimuthal variations for the HTVs.

Fig. 3.16 shows quarterly UT variations of the MAW and HTV activity observed at I53US for the period 2004-2007. The blue and red circles indicate the number of HTV and MAW events detected within each hour, respectively. Most HTV activity is observed around 15:00 UT in the quarters of two and three. The number of detected events are significantly less for both MAWs and HTVs during the second and third quarters. The MAWs and HTVs in the first and fourth quarters show negligible UT dependence. In the second and third quarters, the HTV and MAW activity resembles each other (possibly due to overlap between MAW and HTV events).

Fig. 3.17 depicts changes in H-, D-, and Z-component of magnetic data from CIGO as a function of UT for the period 2004-2007. The figure is generated as for Fig. 3.14. The H-components have the largest variation, and most variations from the three magnetic components roughly occur between 5:00 and 18:00 UT. The changes in B (ΔB_H , ΔB_D , and ΔB_Z) in the first and fourth quarters are much larger than those of the second and third quarters. As discussed before, the HTVs are active in the quarters of one and four, and quite in the quarters of two and three (refer to Fig. 3.16).

In summary, selected MAW and HTV events have $MCCM > 0.7$ (or $SSVR2 < 2.7$) and $\sigma_{\tau} < 3.5$ seconds. Both the MCCM and SSVR2 detectors produces similar results. The MAW events are separated from the HTV events using the trace velocity: $0.3 < V_t < 0.6$ Km/s for the MAW events and $0.65 < V_t < 1.5$ Km/s for the HTV events. Both the MAWs and HTVs are quite in the quarters of two and three, and active in the quarters of one and four. The azimuthal (including quarterly) histograms for a period of four years (2004-

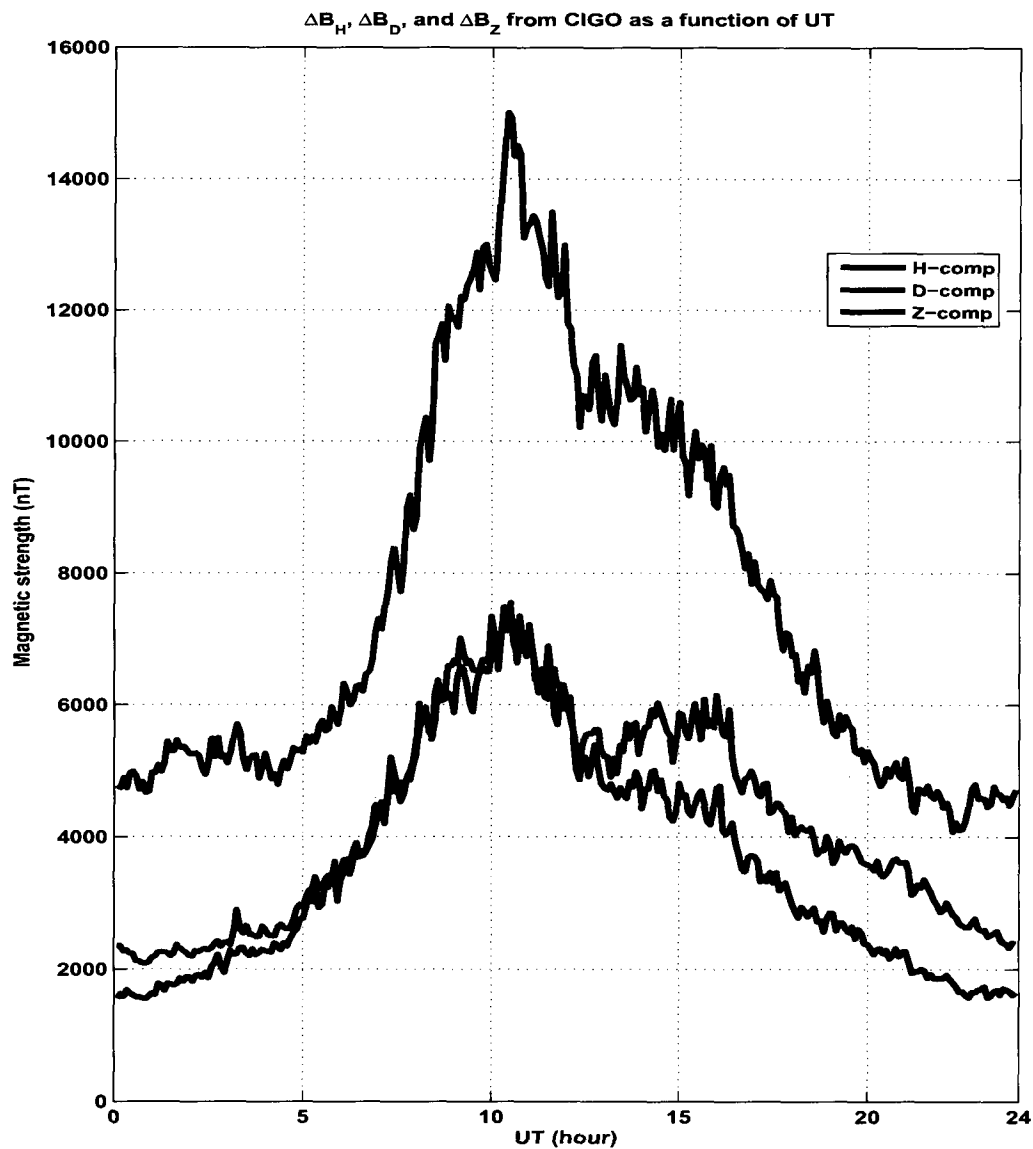


Figure 3.14. Variations of magnetic activity from CIGO as a function of UT. The H-magnetic component has the largest variation, and most variations for the three magnetic components occur between 5:00 and 18:00 UT. All three components have the largest variations around 10:00 UT. See text for details.

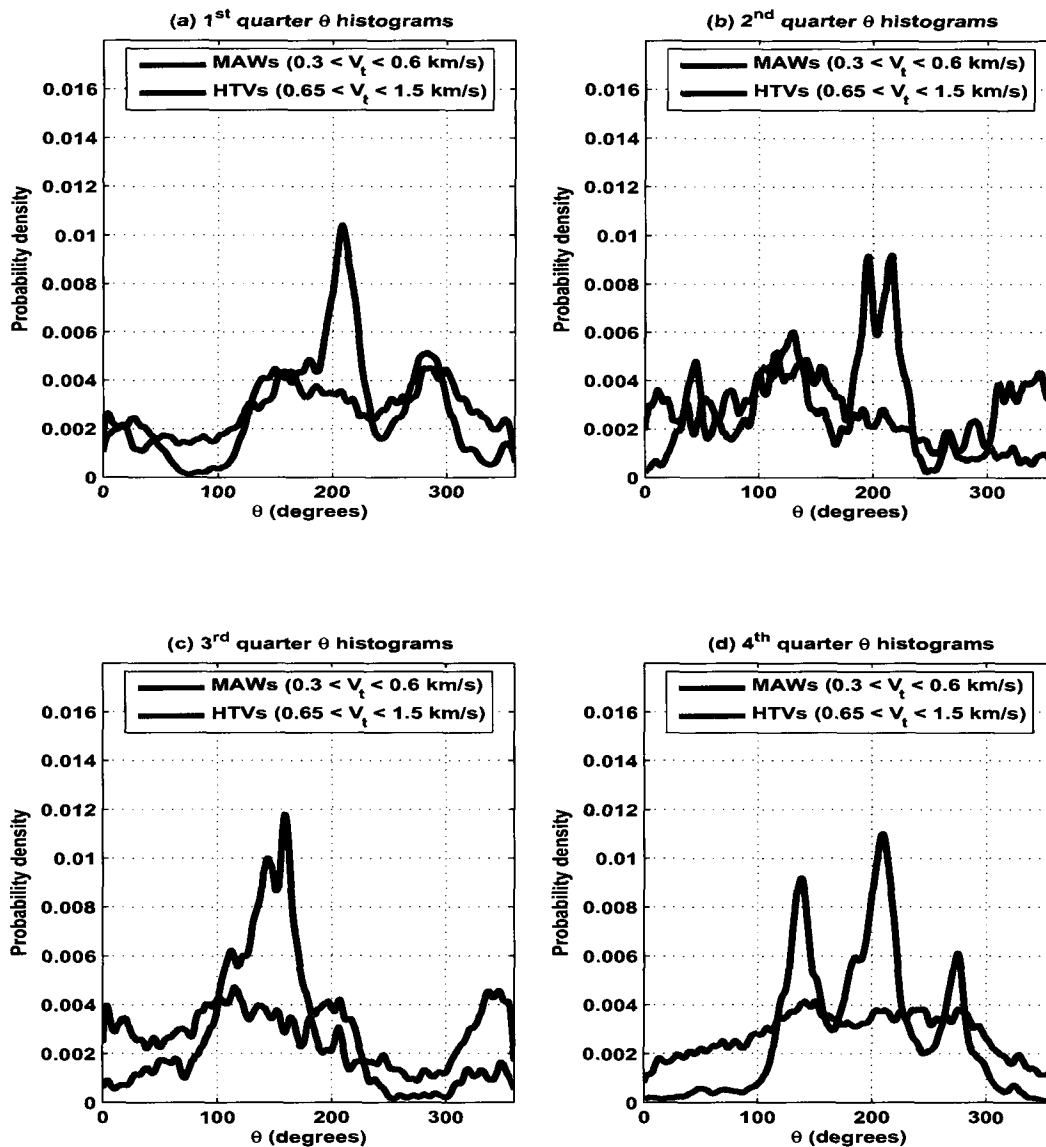


Figure 3.15. Quarterly θ histograms of the MAW and HTV activity at I53US. (a) first quarter, (b) second quarter, (c) third quarter and (d) fourth quarter. In (a)-(d), the blue and red curves represent the HTVs and MAWs, respectively. We see MAWs from three mountain ranges in the plots of quarters in (a) and (d). We do not observe any consistent patterns in the quarterly azimuthal variations for the HTVs. See text for details.

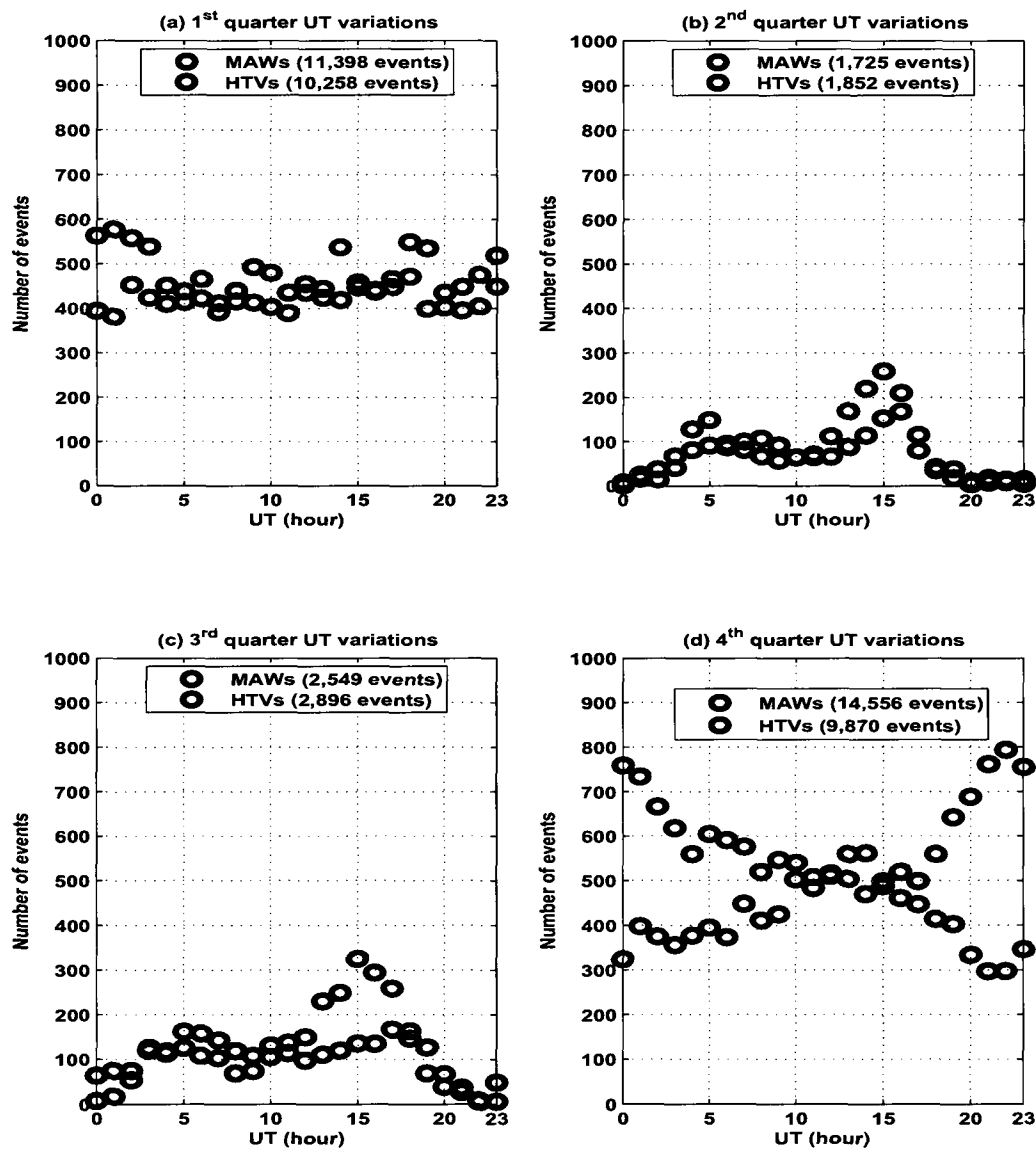


Figure 3.16. Quarterly UT variations of the MAW and HTV activity at I53US. (a) first quarter, (b) second quarter, (c) third quarter and (d) fourth quarter. In (a)-(d), the blue and red circles indicate the number of HTV and MAW events detected within each hour, respectively. Most HTV activity is observed around 15:00 UT in the quarters of two and three. The number of events are significantly less for both MAWs and HTVs during the second and third quarters. The MAWs and HTVs in the first and fourth quarters show negligible UT dependence.

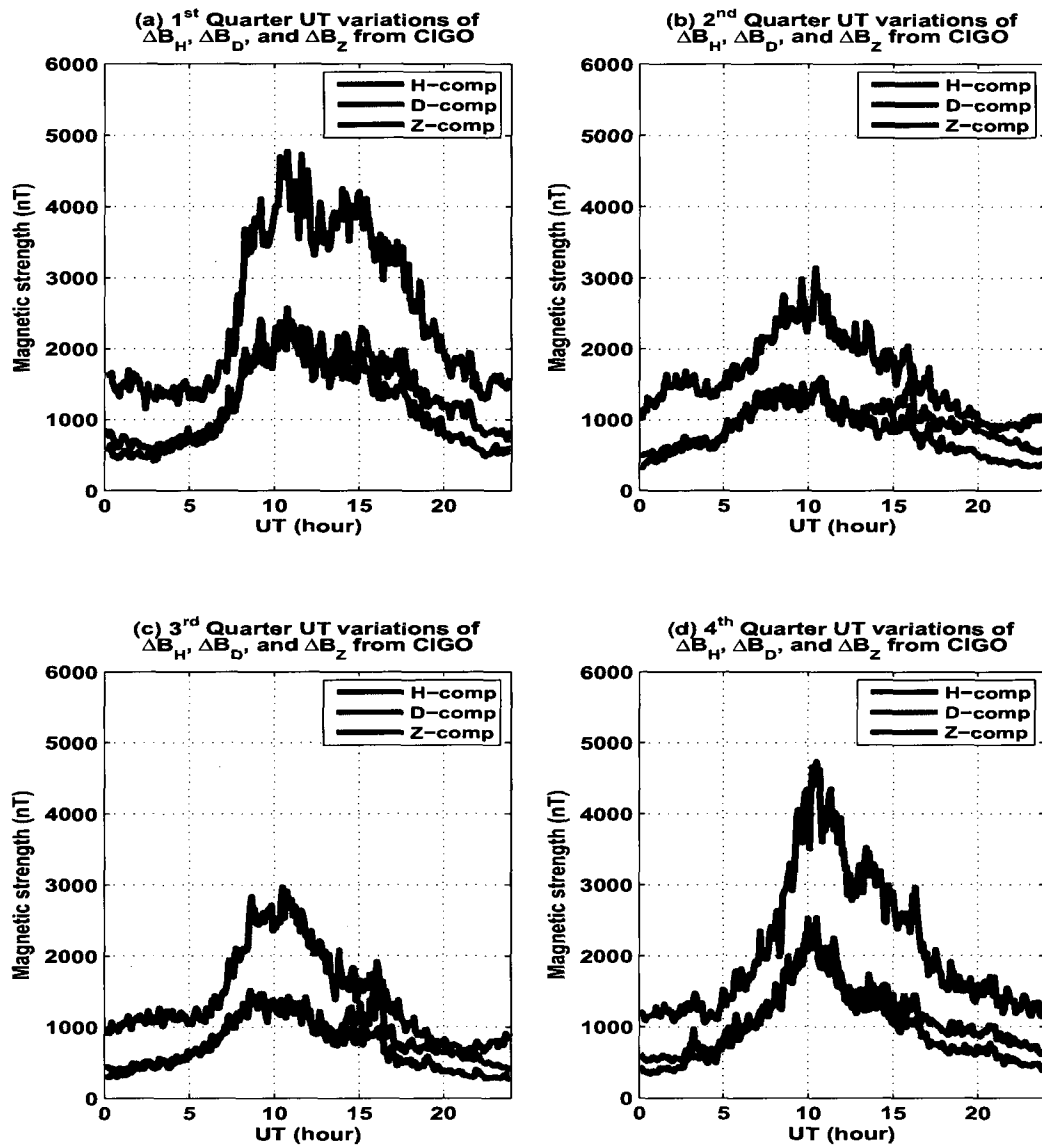


Figure 3.17. Quarterly UT variations of changes in magnetic activity from CIGO. (a) first quarter, (b) second quarter, (c) third quarter and (d) fourth quarter. In (a)-(d), the H-components have the largest fluctuations, and most variations from the three magnetic components roughly occur between 5:00 and 18:00 UT. The changes in B (ΔB_H , ΔB_D , and ΔB_Z) in the first and fourth quarters are much larger than those of the second and third quarters.

2007) suggests three mountain ranges for the MAWs: the Saint Elias Range (110° - 150°), the Alaska and Aleutian Ranges (170° - 230°), and possibly the Seward and Chukotsk Peninsulas (275° - 300°). There is no significant directional dependence for the HTVs in the azimuthal variations. In 2007, the MAWs from the Alaska and Aleutian Ranges dominated over other mountain ranges, which might be a result of missed events (propagating in different paths). From the UT (including quarterly) variations, the HTV activity is most likely to occur between 5:00 and 18:00 UT, and most variations in changes of magnetic activity also occur during the same period. We find no correlation between the MAW activity and changes in magnetic activity. Such an observation suggests that the auroral activity is the likely source of the HTVs.

3.4 Antarctic Array

Similar to the previous section, we first determine the thresholds for various characterization parameters for MAWs and HTVs observed at the Antarctic array (I55US) using the past four years of infrasound data (2004-2007). We then generate various plots (azimuthal, UT, and seasonal variations) for the MAWs and HTVs, and such plots are used to identify possible sources of the MAWs and HTVs.

Fig. 3.18 depicts histograms of estimated parameters (MCCM, SSVR2, V_t , and σ_{τ}) for all available infrasound data between January, 2004 and December, 2007 from the Antarctic array. Each parameter is estimated by taking the same steps used to produce Fig. 3.9. The thresholds are determined by finding a region of zero (or closest to zero) slope between the two distribution curves to minimize overlap of the two curves in each of the parameter histograms (refer to Section 3.3). The thresholds of parameters (except SSVR2) for the Antarctic array are same as those of parameters for the Fairbanks array. The threshold for the SSVR2 detector is set at 2.6. Unlike the SSVR2 histogram, we could not find the region of zero slope between the two distribution curves in the MCCM histogram. This may be due to positive skewness of the distribution curve for the signals of interest. Thus, the threshold is determined by finding an inflection point between the two distribu-

Table 3.2. Parameter selection criteria for the MAWs, HTVs and clutter at I55US.

MAWs	HTVs	clutter
MCCM > 0.7	MCCM > 0.7	MCCM < 0.7
SSVR2 < 2.6	SSVR2 < 2.6	SSVR2 > 2.6
$\sigma_\tau < 3.5$ s	$\sigma_\tau < 3.5$ s	$\sigma_\tau > 3.5$ s
$0.3 < V_t < 0.6$ Km/s	$0.65 < V_t < 1.5$ Km/s	$0 < V_t < 1.5$ Km/s

tion curves. In the σ_τ histogram, there is a small distribution curve ($3.5 < \sigma_\tau < 16$ seconds). These unknown signals have low correlation values (clustered around 0.6) and travel at sub-acoustic speed (clustered around 150 m/s). Since we do not know the source of these signals we exclude them in this thesis. From the MCCM and SSVR2 histograms, we see that only a small fraction of received signals are highly correlated across the array. We summarize the parameter selection criteria for the Antarctic array in Table 3.2. The table is as for Table 3.1.

We now search for events with parameters that exceed their thresholds from the Antarctic data (for the period 2004-2007) and construct a total of six histograms: azimuthal, UT, and seasonal variations based on the two detection algorithms. Plots in the left column of Fig. 3.19 are generated with $MCCM > 0.7$, $\sigma_\tau < 3.5$ seconds, and $0.3 < V_t < 1.5$ Km/s. Plots in the right column of the figure are produced with $SSVR2 < 2.6$, $\sigma_\tau < 3.5$ seconds, and $0.3 < V_t < 1.5$ Km/s. Based on the selection criteria, we expect to detect both MAWs and HTVs. The azimuthal variations show a single directional band (300° - 20°). There is a global peak around 5:00 UT in the UT variations, and the seasonal variations show that both MAWs and HTVs are active from October to February and quiet from March to September. Both MCCM and SSVR2 detectors produce similar results.

We can use the trace velocity to discriminate the HTVs from MAWs (see Fig. 3.20). The azimuthal variation of Fig. 3.19 (top left plot) is divided into MAWs and HTVs based on the V_t estimate. The red curve indicates the MAWs which come from the Alps Range of the

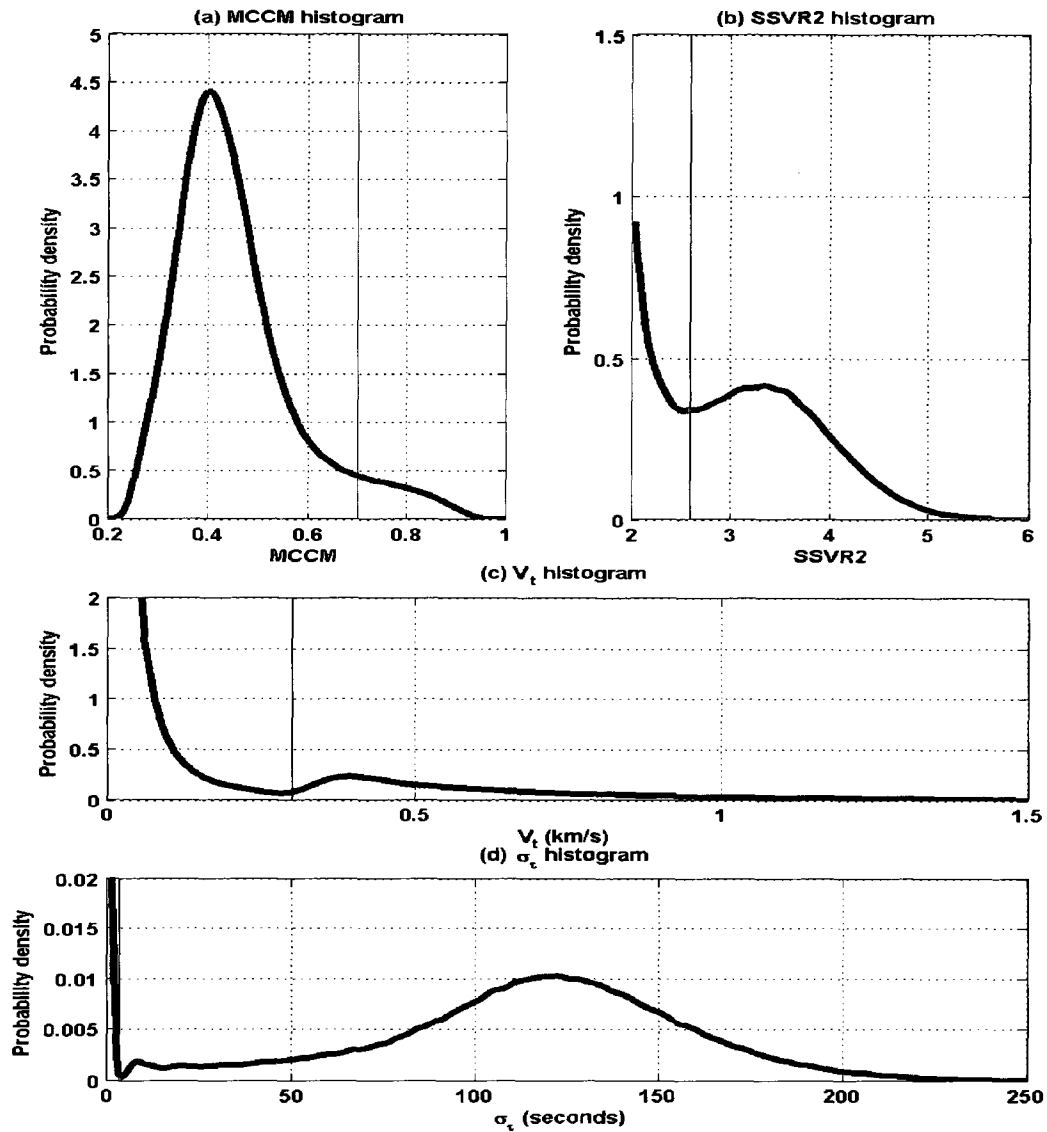


Figure 3.18. Histograms of characterization parameters at I55US (2004-2007). (a) MCCM histogram, (b) SSVR2 histogram, (c) V_t histogram and (d) σ_τ histogram. The shaded area represents the region of signal detection. From the MCCM and SSVR2 histograms, we see that only small fraction of received signals are highly correlated across the array. See text for details.

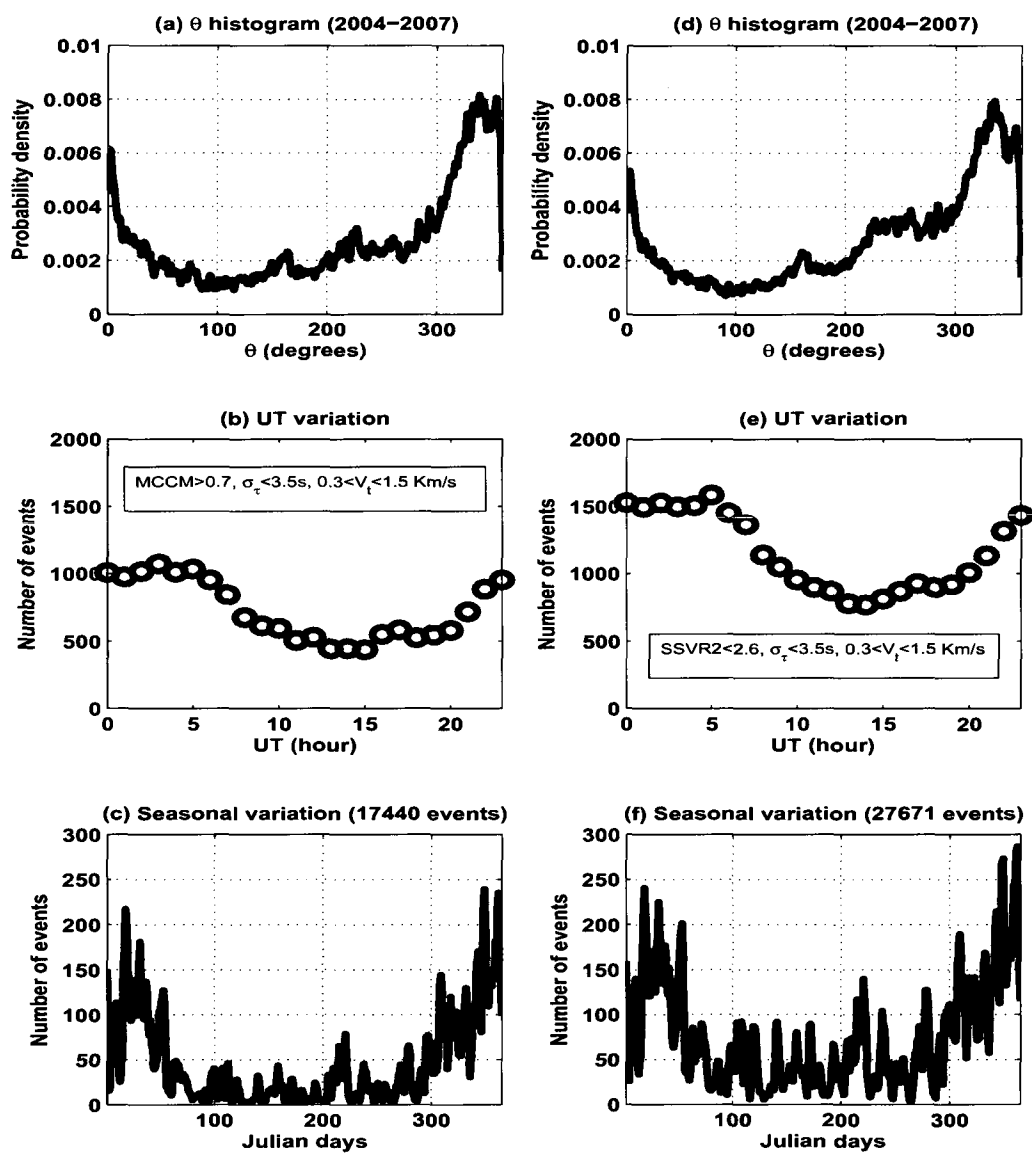


Figure 3.19. Variational plots of low-frequency signals detected at I55US. (a) θ histogram, (b) UT variation, (c) seasonal variation, (d) θ histogram, (e) UT variation and (f) seasonal variation. (a)-(c) are based on the MCCM detector and (d)-(f) are based on the SSVR2 detector. Notice that both MCCM and SSVR2 detectors produce similar results. The MAWs and HTVs are active from October to March and quiet from April to September. See text for details.

South Island, New Zealand (320° - 10°). The blue curve represents the HTVs, which seem to have a directional dependence: 270° - 30° . There is some leakage in that it is possible that some detections are masquerading as the HTVs.

We find that the azimuthal variations of MAWs have a similar directional dependence for all years except 2007 (see Fig. 3.21). The red and blue curves indicate the MAWs and HTVs, respectively. Strong MAW activity is observed from three directional bands: 140° - 190° , 220° - 300° , and 320° - 10° (the Alps Range of the South Island, New Zealand). The variation in shape could be due to the missed events (propagating along different paths) or changes in tropospheric wind flows. The HTV curve shows negligible directional dependence.

Fig. 3.22 shows UT variations of the MAW and HTV activity observed at the Antarctic array (see Fig. 3.20). The blue and red circles indicate the number of HTV and MAW events detected within each hour, respectively. There is a global peak around 5:00 UT for MAWs in all UT variations, and a similar pattern is consistently observed in each year between 2004 and 2007. The UT variations (for year 2006 and 2007) for the MAWs and HTVs resemble each other, suggesting that some detections are masquerading as the HTVs. The UT variations of the HTVs are less consistent than those of the MAWs. The number of detected events at the Antarctic array is much less than that at the Fairbanks array (refer to Fig. 3.13).

Fig. 3.23 depicts quarterly azimuthal variations of MAWs and HTVs detected at the Antarctic array for the period 2004-2007. The blue and red curves represent the HTVs and MAWs, respectively. We observe MAWs from the Alps Range of the South Island, New Zealand in the plots of quarters one and four. In the plots of quarters two and three, there are virtually no MAW and HTV activity in the azimuth between 0° and 140° . In the plot of quarter one, MAW activity is very quite between 50° and 190° . The azimuthal variations for the MAWs and HTVs show resemblance in all quarters, suggesting that some detections are masquerading as the HTVs.

Fig. 3.24 shows quarterly UT variations of the MAW and HTV activity observed at

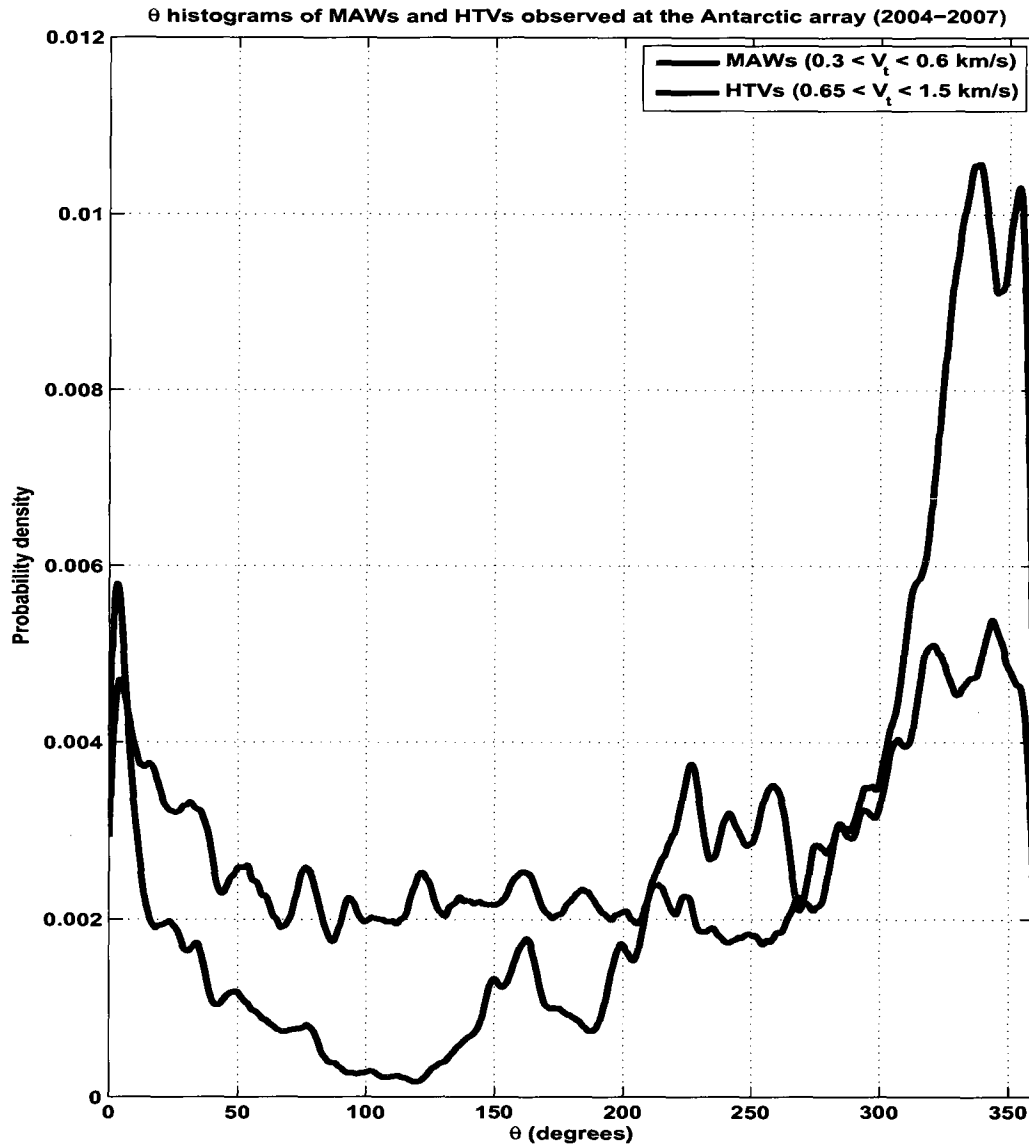


Figure 3.20. θ histograms of the MAW and HTV activity at I55US (2004–2007). The red and blue curves indicate the MAWs and HTVs, respectively. The MAWs come from the Alps Range of the South Island, New Zealand. The HTV curve seems to have a directional dependence: 270° – 30° . There is some leakage in that it is possible that some detections are masquerading as the HTVs.

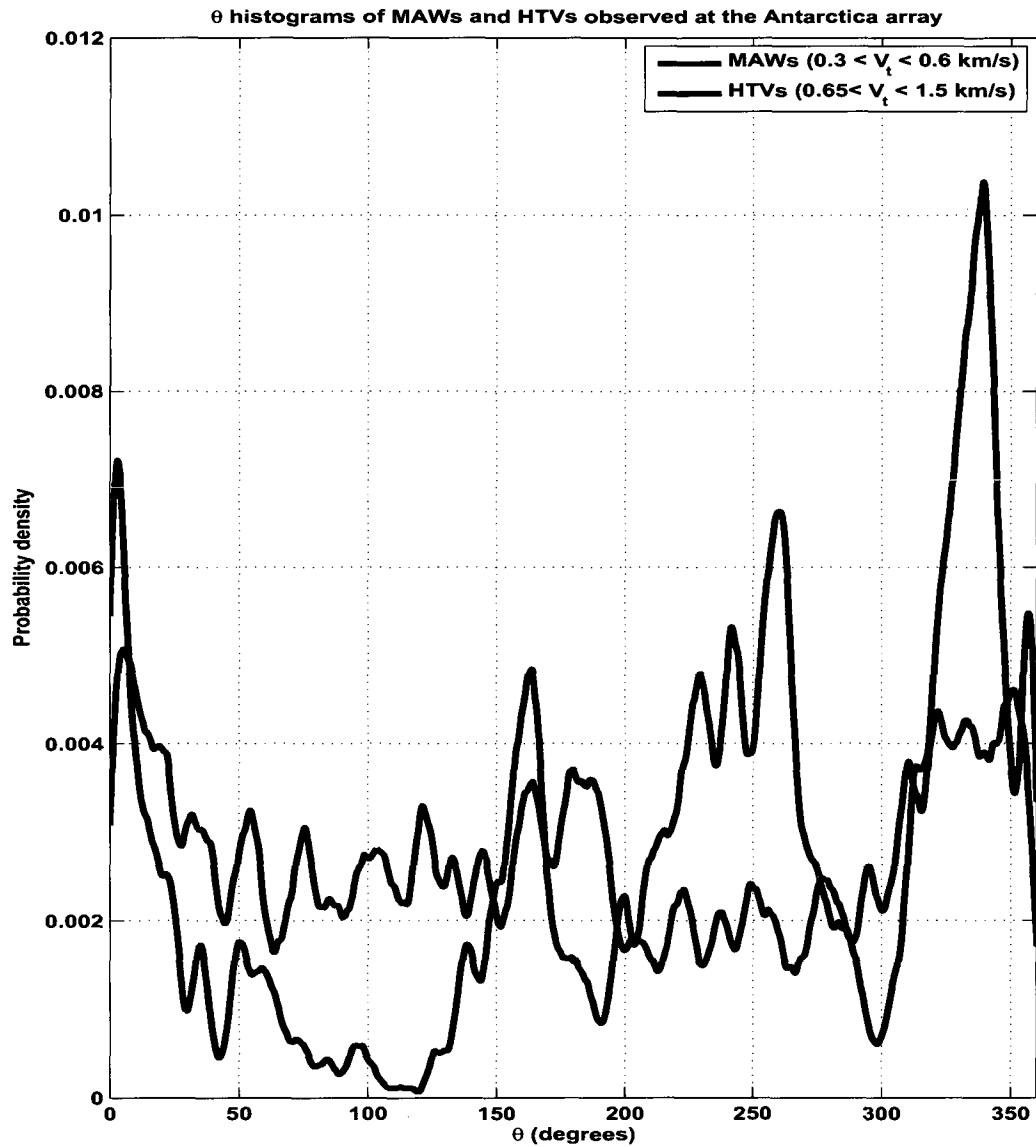


Figure 3.21. θ histograms of the MAW and HTV activity at I55US (2007). The red and blue curves indicate the MAWs and HTVs, respectively. Strong MAW activity is observed from three directional bands: 140° - 190° , 220° - 300° , and 320° - 10° (the Alps Range of the South Island, New Zealand). The HTV curve shows negligible directional dependence.

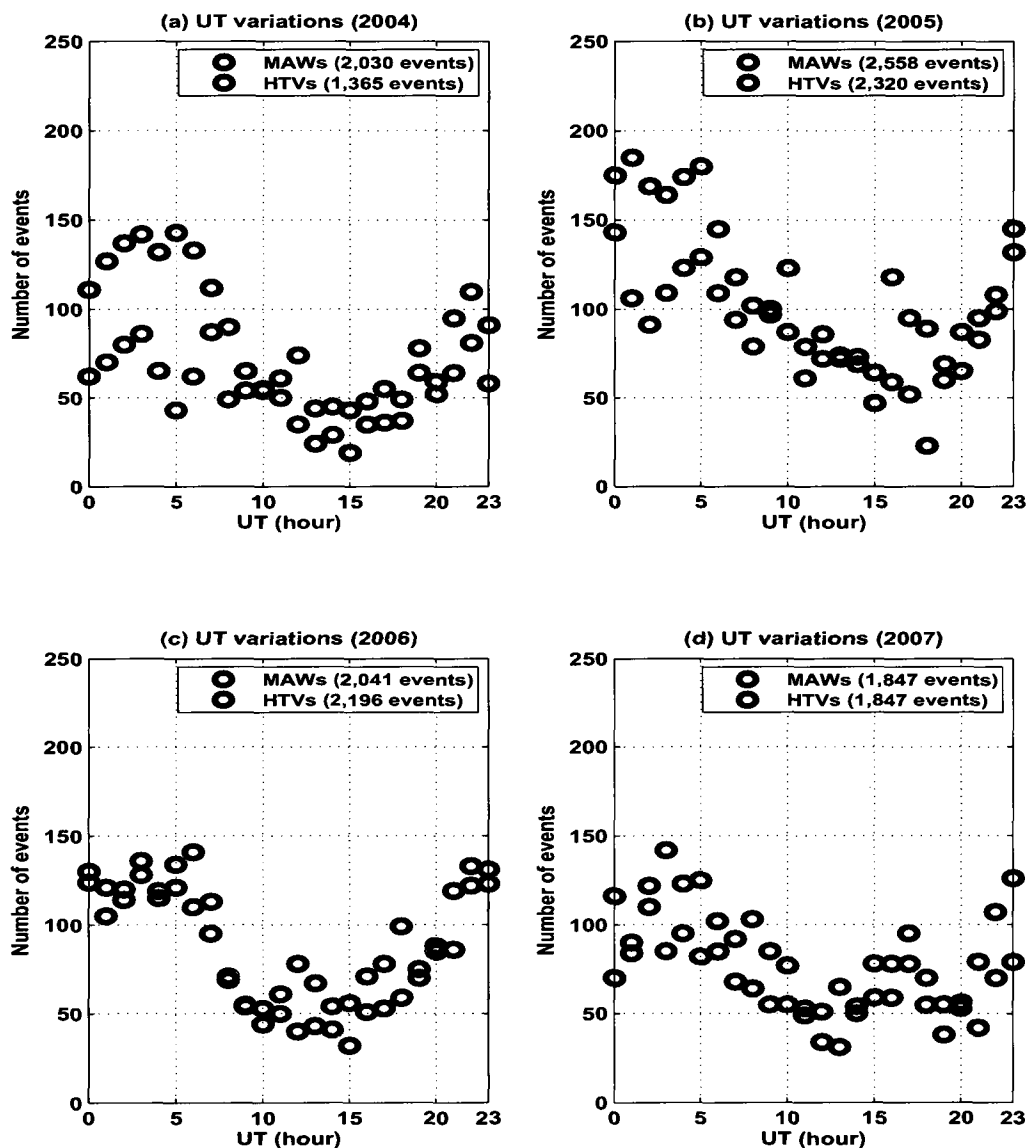


Figure 3.22. UT variations of the MAW and HTV activity at I55US (2004-2007). (a) year 2004, (b) year 2005, (c) year 2006 and (d) year 2007. In (a)-(d), the blue and red circles indicate the number of HTV and MAW events detected within each hour, respectively. In (a)-(d), there is a global peak around 5:00 UT for the MAWs, and a similar pattern is consistently observed in each year between 2004 and 2007. The UT variations (for year 2006 and 2007) for the MAWs and HTVs resemble each other, suggesting that some detections are masquerading as the HTVs. The UT variations of the HTVs are less consistent than those of the MAWs.

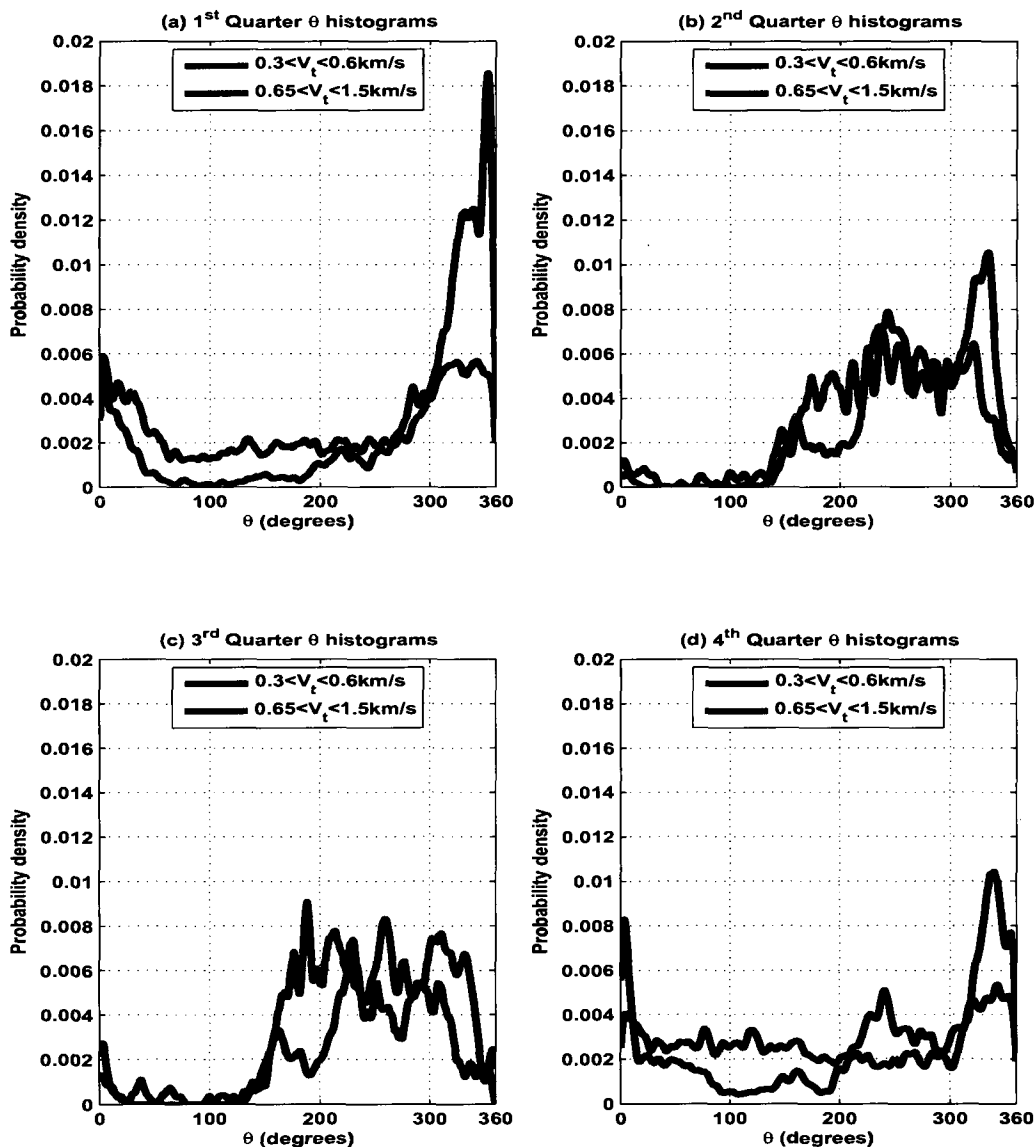


Figure 3.23. Quarterly θ histograms of the MAW and HTV activity at I55US. (a) first quarter, (b) second quarter, (c) third quarter and (d) fourth quarter. In (a)-(d), the blue and red curves represent the HTVs and MAWs, respectively. We observe MAWs from the Alps Range of the South Island, New Zealand in the plots of quarters one and four. See text for details.

I55US for the period 2004-2007. The blue and red circles indicate the number of HTV and MAW events detected within each hour, respectively. We observe a global peak around 5:00 UT for the MAWs in the plots of quarters one and four. The number of detected events are significantly less for both MAWs and HTVs during the second and third quarters. The UT variations for the MAWs and HTVs show resemblance in the plots of quarters one and four, suggesting that some detections are masquerading as the HTVs (or vice versa).

In summary, selected MAW and HTV events have $MCCM > 0.7$ (or $SSVR2 < 2.6$) and $\sigma_t < 3.5$ seconds. Both the MCCM and SSVR2 detectors produces similar results. The MAW events are separated from the HTV events using the trace velocity: $0.3 < V_t < 0.6$ Km/s for the MAW events and $0.65 < V_t < 1.5$ Km/s for the HTV events. Both the MAWs and HTVs are quite in the quarters of two and three, and active in the quarters of one and four. The azimuthal (including quarterly) histograms for a period of four years (2004-2007) suggests that a primary source of the MAWs is the Apls Range of the South Island, New Zealand (320° - 10°). The HTVs seem to have a directional dependence (270° - 30°). In 2007, we have two unknown directional bands (140° - 190° and 220° - 300°) for the MAWs. From the UT (including quarterly) variations, the MAW activity is most likely to occur at 5:00 UT, whereas the HTV activity is least like to occur between 10:00 and 15:00 UT.

3.5 Summary

In this chapter, we introduced two new detection algorithms (SSVR1 and SSVR2), and compared them with well known detection algorithms (MCCM and F-stat) using the receiver operating characteristics (ROC) curves. We use three types of infrasound signals (mine blasts for the high-frequency band, microbaroms, and MAWs for the low-frequency band) and two types of noise (Gaussian white and pink ($1/f$) noise). The Gaussian white noise (with flat power spectral density) best represents electronic noise whereas the pink noise (with f^{-2} power spectral density) best describes geophysical noise. It is, therefore, very important to test the performance of SSVR2 detector against both types of noise. The detector performance should be frequency independent.

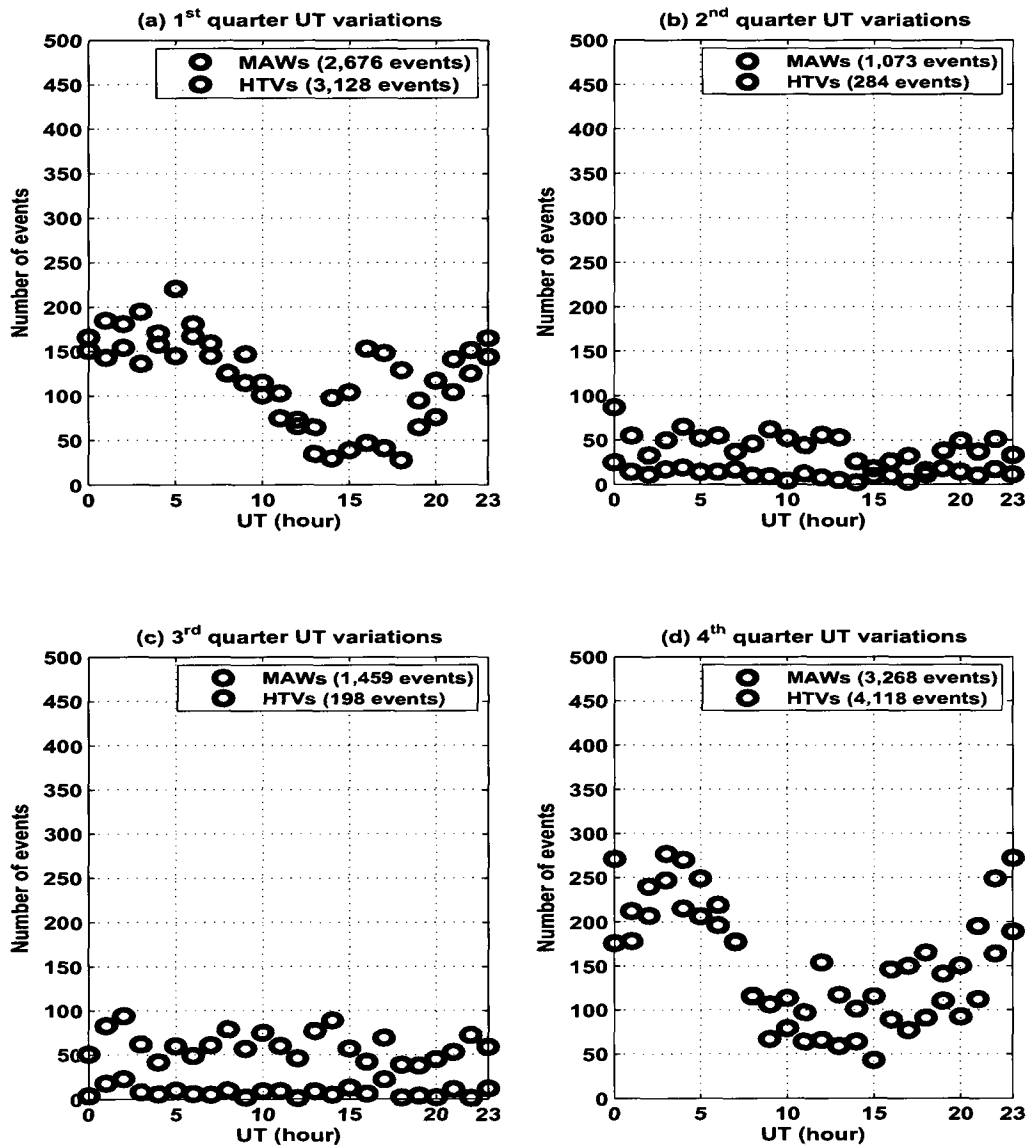


Figure 3.24. Quarterly UT variations of the MAW and HTV activity at I55US. (a) first quarter, (b) second quarter, (c) third quarter and (d) fourth quarter. In (a)-(d), the blue and red circles indicate the number of HTV and MAW events detected within each hour, respectively. In (a) and (d), the UT variations of the MAWs are similar, and we observe a global peak around 5:00 UT for the MAWs. The number of detected events are significantly less for both MAWs and HTVs in the quarters of two and three.

We find that the SSVR1 detector outperforms other three detectors for the mine blasts as the SNRs decrease for both types of noise. As the SNR of the mine blasts (against the white noise) decreases from -3 dB to -7 dB, for example, TP (%) of the four detectors at FP = 20% roughly decreases from 60% to 20% for F-stat, 100% to 50% for MCCM, 100% to 100% for SSVR1, and 100% to 65% for SSVR2 (refer to Fig. 3.1). As for pink noise, TP (%) of the four detectors at FP = 20% roughly decreases from 23% to 20% for F-stat, 97% to 60% for MCCM, 100% to 85% for SSVR1, and 60% to 30% for SSVR2, as the SNR of mine blasts decreases from -3 dB to -7 dB (see Fig. 3.4). For microbaroms and MAWs, the SSVR2 detector outperforms other three detectors as the SNR decreases for both types of noise. As the SNR of microbaroms (against the white noise) decreases from -3dB to -7dB, for example, TP (%) of the four detectors at FP = 20% roughly decreases from 47% to 20% for F-stat, 98% to 50% for MCCM, 92% to 40% for SSVR1, and 100% to 97% for SSVR2 (refer to Fig. 3.2). As for pink noise, TP (%) of the four detectors at FP = 20% roughly decreases from 30% to 20% for F-stat, 96% to 45% for MCCM, 55% to 20% for SSVR1, and 100% to 92% for SSVR2, as the SNR of microbaroms decreases from -3 dB to -7 dB (see Fig. 3.5). As for the MAWs, changes in TP at FP = 20%, as the SNR decreases from -3 dB to -7 dB, for both types of noise are similar to those of the microbaroms (refer to Figs. 3.3 and 3.6).

In addition, the SSVR based detectors are computationally very efficient compared to the MCCM detector, and they are independent of array size (e.g. number of sensors in an array). The execution time of SSVR2 detector for window size of 10000 points is approximately 10 times faster than that of the MCCM detector for an array consists of 10 sensors (see Fig. 3.7). The speed improvement increases exponentially, as the number of sensors increases. For the same window size and number of sensors, the F-stat detector is about 9 times faster than the SSVR2 detector. However, the SSVR based detectors are better choice than the F-stat detector if we consider the detector performance at low SNRs.

We use five estimated parameters (MCCM, SSVR2, V_i , θ , and σ_τ) to analyze infrasound data (for the period 2004-2007) from the Fairbanks and Antarctic arrays. Based on the parameter selection criteria for both the Fairbanks and Antarctic arrays (refer to Tables 3.1

and 3.2), we generate various plots (azimuthal, Universal time, and seasonal variations), and such plots are used to identify the possible sources of the MAWs and HTVs.

For the I53US array, the MAWs and HTVs are active in the first and fourth quarters, and quite in the second and third quarters (see Figs. 3.10 and 3.19). We use the trace velocity limits developed in Chapter 1 to separate the MAWs from the HTVs. Most MAWs observed at the Fairbanks array come from three mountain ranges: the Saint Elias Range (110° - 150°), the Alaska and Aleutian Ranges (170° - 230°), and possible the Seward and Chukotsk Peninsulas (275° - 300°). The HTVs seem to have no azimuthal dependence. The UT variations of HTVs have a global peak around 15:00 UT, and a similar pattern is consistently observed in each year between 2004 and 2007 (refer to Fig. 3.13). Unlike the UT variations of HTVs, we do not observe any patterns in the UT variations of MAWs. The HTV and the disturbances in magnetic activity are most likely to occur between 5:00 and 18:00 UT (refer to Figs. 3.13 and 3.14). We also find that the HTV and the variation in magnetic activities are strong in the first and fourth quarters, and quite in the second and third quarters (refer to Figs. 3.16 and 3.17).

For the I55US array, the MAW and HTV are active in the first and fourth quarters, and quite in the second and third quarters (see Figs. 3.19 and 3.24). The MAW activity is dominated by the Alps Range of the South Island, New Zealand (320° - 10°), and the HTV activity has a directional band similar to that of the MAWs (refer to Fig. 3.20). The UT variations of MAWs have a global peak around 5:00 UT, and a similar pattern is consistently observed in each year between 2004 and 2007 (see Fig. 3.22). Unlike the UT variations of MAWs, we do not observe any patterns in the UT variations of HTVs. The numbers of MAW and HTV events detected at the Fairbanks array are much higher than those detected at the Antarctic array.

In the next chapter we will use the parameter selection criteria from Table 3.1 and 3.2 to generate feature vectors, which will be used to train, validate, and test four neural networks. The trained networks will be used to automatically detect and classify three types of infrasound low-frequency signals (MAWs, HTVs, and clutter). The detection and clas-

sification of the three signal types are currently done by a human expert. Such a process is very slow and can produce operator-dependent results. The neural network approach, on the other hand, is robust, resistant to the operator's errors, and can thus produce unbiased results. The expert's time can be better used for detailed (or in-depth) studies of the MAWs and HTVs by placing the trained neural networks into use as a signal classifier.

Chapter 4

Neural Networks

4.1 Overview

The average human brain contains about 10 billion interconnected neurons. Each neuron receives and transmits electric signals to thousands of neighboring neurons. For over 50 years, scientists have been trying to create computational neural networks that simulate the behavior of a human brain. Recent advancements in computer technologies have made possible the creation of neural networks with applications ranging from function approximation, regression analysis, principle component analysis, time series prediction, pattern recognition, filtering, system identification, clustering, etc. [68, 69, 70]. Dr. Fred Ham [70, 71, 72] has been studying the separation and classification of infrasound signals using various types of neural networks. He primarily uses cepstral analysis [72], extensively used in voice recognition, to extract features from infrasound data sets. These features are used to train and test the networks.

There are two types of neural networks: one is a biological neural network, which is mainly used in cognitive science and tries to model real biological neurons to understand the behaviour of the central nervous system in a human brain; the other is an artificial neural network, which is used in many fields of general science and borrows on the idea of parallel processing from the human brain to solve complex problems. Artificial neural networks are divided into two subgroups: supervised and unsupervised neural networks. A supervised network learns from examples whereas an unsupervised network learns without any examples. The supervised networks include a perceptron, perceptron network, multi-layered perceptron (MLP) network, probabilistic network, learning vector quantization, and radial basis network [68, 69, 70]. An example of the unsupervised neural network is self organizing maps (SOMs) [68, 70]. A MLP network is a universal classifier and function estimator, and it is the most widely used and accepted neural network today.

The power of the supervised neural networks is their ability to extract the unknown relationships between input and target data sets. A perceptron, which is the simplest su-

pervised network, consists of a single input and output nodes. The dimensions of the input node are arbitrary and determined by the length of the input vector (column of the input data set). From the perspective of a biological neuron (refer to Fig. 4.1), the dimension of the input node is related to the number of neighboring neurons that are connected to the current neuron. The output signals from the neighboring neurons are delivered to the current neuron by travelling through connective tissues (e.g. dendrites). The job of dendrites in a biological neuron is to transfer electric signals between interconnected neurons but also change the strengths of electric signals (based on the strength of signal). In the computational neural network, the weight vector replaces the dendrites of the biological neuron. As we shall see, the weight vector plays an important role in the decision making process of the biological neuron.

When the cumulative sum of these signals enters the Soma (“the brain” of a biological neuron), the neuron decides to become active or inactive. There are different activation functions to model the behavior of the Soma, but the threshold based transfer function (e.g., a step function: the output of the Soma is equal to zero if the cumulative sum is less than zero and one otherwise) is widely accepted and used. In the neural network, the dot product between the weight and input vectors goes into the activation function, and so the weight vector, in essence, has the effect of changing threshold value of the activation function. The weight vector must have the same dimension as the input vector. The dimension of output node is equal to one, and the output value depends on the type of activation function. It can be binary (1 or 0), bipolar (-1 or 1) or linear.

In the supervised neural network, the user provides input and target data sets, and random numbers are used to initialize weights (elements of weight vectors) of the network (each neuron has its own weight vector). The initialized network is then trained to produce desired outputs for given input data set. The training (or adjusting weights) of the network is an iterative process, which depends on a residual error computed at each epoch. The residual error is a sum of squared differences in elements between the network outputs and target data sets, and an epoch defines one sweep of input-target (or training) data sets

through the network. The output data set must have the same size as the target data set. Generally speaking, the residual error decreases as the epoch number increases. When the residual error reaches some threshold (set by the user), we say that the network is properly trained (or learned the relationships between the input and target data sets).

For the network to be properly trained, we need to consider several important factors: first, the network should contain as few neurons (or perceptrons) as possible. Even though the network becomes more powerful and flexible by using more neurons, the network can be over-fitted, and this results in a poor generalization [73]. Therefore, it is important for the user to find the optimum number of neurons for the network by trial and error. Second, a training data set should thoroughly represent the input space. This ensures that the network performance is not biased towards a certain region of the input space [68, 70]. Other important factors include a learning rate, ranges of variables in the input data set, and minimum performance error. Such factors are discussed in more detail in the later part of this section.

In the next section, we introduce some basics (a brief history, similarity between the computer model and a biological neuron) and mathematical properties of a perceptron. Then, we introduce the more powerful and flexible perceptron network, and discuss how decision boundaries are generated by each perceptron (or neuron). In general, it is very difficult to determine theoretically the optimum number of neurons required to solve classification problems. This is especially true for problems involving non-linear classification. Fortunately, our classification problem was simple enough that it did not involve any non-linear classification. Thus, a perceptron network with two neurons are used in this thesis to classify three types of low-frequency infrasound signals (MAWs, HTVs, and clutter).

4.2 Perceptron vs. Perceptron Network

A perceptron is the simplest supervised neural network. It is a building block for a very popular multi-layered perceptron (MLP) network [68, 70]. The perceptron tries to model a biological neuron using the McCulloch-Pitts model [74]. The concept of perceptron was

developed by Rosenblatt in 1950s, and it was the first neural network capable of learning and performing classification [75, 76]. The idea is quite simple and easy to understand; however, it is not as powerful and flexible as the MLP network. Unlike the MLP network, it is only capable of solving linearly separable classification problems. Minsky and Papert demonstrated that the perceptron's inability to solve exclusive OR (XOR) problems [77]. Historically, this was a stumbling block that held up the neural network field for about 20 years. This problem was solved by introducing multiple neurons to form a perceptron network. Such a network is much more powerful and flexible than a single perceptron. As we shall see, the perceptron network with two neurons is sufficient to solve our infrasound classification problem. We will discuss more about the perceptron and perceptron network in a later part of this section.

Fig. 4.1 displays a simplified schematic of a biological neuron [78]. It has several components, but we only use some of these components (dendrites, soma, and terminal buttons) to model the neuron. Unlike the biological neuron, the perceptron has a single output node, and the number of dendrites in the neuron is determined by the dimension of an input vector. In the biological neuron, electrical signals from the neighboring neurons are transmitted to the current neuron, and they are summed and passed to the soma, where a decision (to become active or remain inactive), is made. If it becomes active, then electrical signals are sent out to neighboring neurons through axon branches. Similarly, when input vectors are entered to the perceptron, the activation function (e.g., the McCulloch-Pitts model) makes a decision to output one (to become active) or zero (to remain inactive).

Fig. 4.2 illustrates a neural network flow chart. The purpose of the neural network is to produce desired outputs for given inputs. This is done by training, which is an iterative process that tries to minimize the differences between outputs and targets for the given inputs. The residual error is defined as the sum of squared differences between the outputs and targets for all available input data. The training of the network is based on the residual error, and the network trains by adjusting weights. Since the training is an iterative process, the error and weights are a function of discrete time step k . We say that

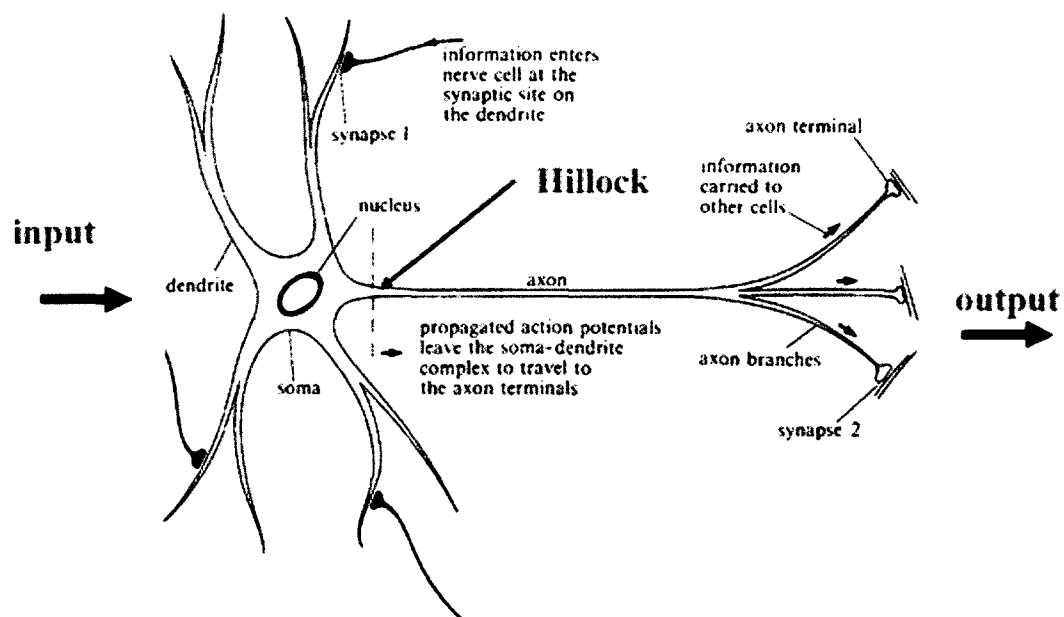


Figure 4.1. Cartoon of a biological neuron. In the biological neuron, electrical signals from the neighboring neurons are transmitted to the current neuron, and they are summed and passed to the Soma, where a decision (to become active or remain inactive), is made. If it becomes active, then electric signals are sent out to neighboring neurons through axon branches. We use some of these components (dendrites, soma, and axon terminals) to build a perceptron. Unlike the biological neuron, the perceptron has a single output node, and the number of dendrites in the neuron is determined by the dimension of an input vector.

the network is trained when the residual error falls below a threshold set by the user. We will discuss more about the threshold and residual error in the later part of this section.

The perceptron is only capable of distinguishing two linearly separable classes, and this severely limits its application to various classification problems. To resolve such a problem, multiple perceptrons are combined in a single layer to form a more powerful perceptron network (refer to Fig. 4.4). It has multiple input nodes, and the number of output nodes equals to the number of activation functions. The perceptron network is much more flexible in distinguishing a larger number of linearly separable classes than the perceptron can [79]. For example, a perceptron network with three output nodes can distinguish up to eight classes assuming they are linearly separable. We, therefore, increase the number of perceptrons in the network, as the number of classes increases. The network behavior depends on various factors; the dimension of the input vector, number of perceptrons, the type of activation function, learning rate, and error goal. We will discuss such factors and the effects of them in the network in the later part of this section.

Now, let us introduce some basic mathematics behind the concept of a perceptron. Consider a perceptron with a single input vector \vec{p} , output value a , bias term b , weight vector \vec{w} , and activation function f (refer to Fig. 4.3). The bias term adds an extra degree of freedom to the network, and the activation function, by definition, is a step function. The network is supplied with input-target data sets by the user, and the input data set, in general, is a matrix (each column vector is an example). The target data set is a row vector, and it has the same number of columns as the input data set. Once an example enters the network, the sum $(\vec{p} \cdot \vec{w} + b)$ is passed to the activation function. If the sum $(\vec{p} \cdot \vec{w} + b)$ is less than zero, the output (a) is zero, otherwise the output is one. So, the perceptron can divide the input data sets into two groups, assuming the data sets are linearly separable into two groups.

Before the network can be used for classification problems, first, it has to be trained. The user provided input-target data sets are used to compute a residual error, which are then fed back to the network for the training. This is an iterative process, which means

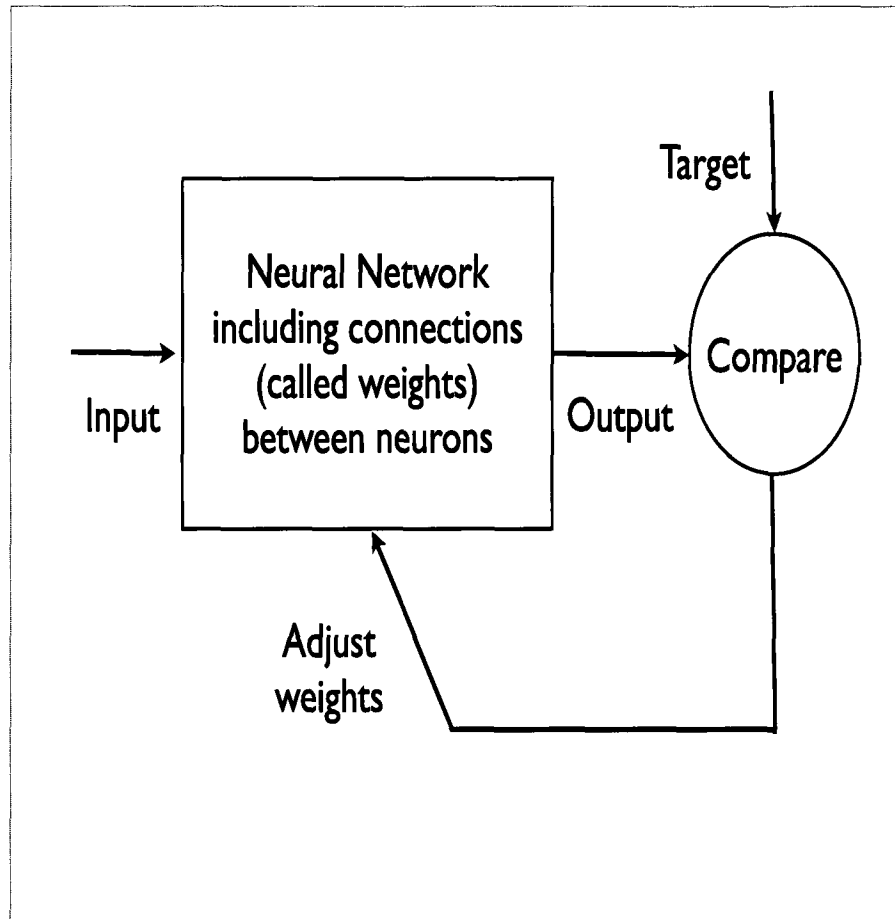


Figure 4.2. Neural network flow chart. The purpose of the neural network is to produce desired outputs for given inputs. The differences between outputs and targets for the given inputs are fed back to the network for training. The training is an iterative process, and it is based on the residual error. The network trains by adjusting weights, and we say that the network is trained when the residual error becomes less than some threshold set by the user.

that the error is computed at every epoch (or time step). When the error falls below a user selected value, the network is trained and ready for the classification. We will use a perceptron, as an example, to show how the network trains itself using user supplied data sets.

Now, suppose that the network in Fig. 4.3 is provided with input-target data sets. The input data set \mathbf{P} , which is a matrix, consists of N column vectors \vec{p} , and the target data set is a N element row vector. The i^{th} column vector \vec{P}_i is referred to as the i^{th} example of the input data set, and the error between the output and target values for the i^{th} example at the k^{th} time step, $E_i(k)$, is given by

$$E_i(k) = f(\vec{w}(k)^T \cdot \vec{P}_i) - t_i, \quad (4.1)$$

where a superscript T is a transpose operator, t_i is a target (or desired output) for the i^{th} example, and f is a step function. For simplicity, the bias term b is absorbed into the weight vector \vec{w} , and one is appended at the beginning of the input vector \vec{P}_i . Since we want the network to produce output values as close as possible to the target values for all available input data, the total error at time step $E(k)$ (or cost function $\epsilon(k)$) is defined as

$$\epsilon(k) = \frac{1}{2} \sum_{i=1}^N (E_i^2(k)). \quad (4.2)$$

The goal is then to find the optimum weight vector, $\vec{w}_{opt}(k)$, that minimizes the cost function $\epsilon(k)$. We apply the steepest gradient descent algorithm iteratively to find $\vec{w}_{opt}(k)$. The gradient is obtained by taking the derivative of the cost function with respect to the weight vector, and the result can be written as

$$\frac{\partial \epsilon(k)}{\partial \vec{w}(k)} = \sum_{i=1}^N E_i(k) \vec{P}_i. \quad (4.3)$$

The weight vector $\vec{w}(k)$ is moved in the direction of $-\sum_{i=1}^N E_i(k) \vec{P}_i$ to obtain a smaller value of $\epsilon(k)$. Similar to a step size in the steepest descent algorithm, a learning rate parameter (γ) is introduced to control the stability and convergence of the algorithm. The learning rate is a small positive number, and the user determines its value by means of trial and

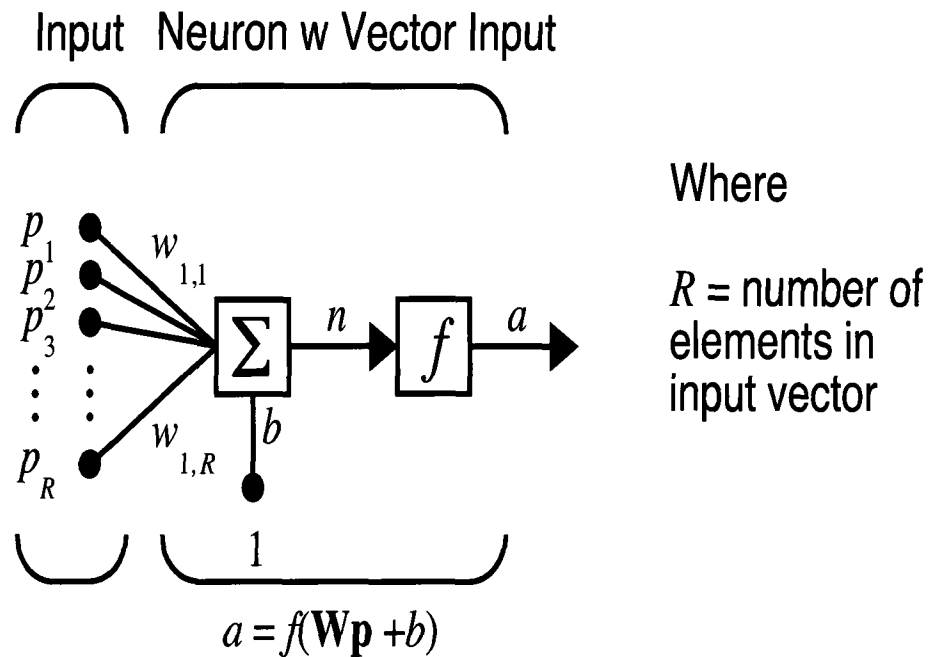


Figure 4.3. A perceptron structure. It including single input vector \vec{p} , output value a , bias term b , weight vector \vec{w} , and activation function f . The bias term adds an extra degree of freedom to the network, and the activation function, by definition, is a step function. The network is supplied with input-target data sets by the user, and the input data set, in general, is a matrix (each column vector is an example). The target data set is a row vector, and it has the same number of columns as the input data set. Once an example enters the network, the sum $(\vec{p} \cdot \vec{w} + b)$ is passed to the activation function. If the sum $(\vec{p} \cdot \vec{w} + b)$ is less than zero, the output (a) is zero, otherwise the output is one.

error: if the learning rate is too small the algorithm converges very slowly to a global minimum of the error function; if it is large, then the algorithm oscillates around the global minimum; if it exceeds some critical value, the algorithm becomes unstable (or diverges). It is generally recommended to use a larger learning rate at the beginning of the training process and exponentially decrease its value with increasing number of time steps [68, 70]. The perceptron uses the default learning rate (γ) of one. The updated weight vector at time step $k+1$, $\vec{w}(k+1)$, becomes

$$\vec{w}(k+1) = \vec{w}(k) - \gamma \left(\sum_{i=1}^N E_i(k) \vec{P}_i \right). \quad (4.4)$$

The weight vector, \vec{w} , is updated at every epoch (or time step). An epoch is a neural network training parameter and is defined as one sweep of the input-target (or training) data sets through the network. For example, 100 epochs imply that the training data sets are presented to the network 100 times, and as a result, the weight vector gets updated 100 times. The network learns hidden relationships between the input and target data sets through updating its weight vector. The training process continues until it satisfies any one of the stopping criteria: a maximum number of epochs, a minimum gradient ($\partial \vec{w}(k)$) change, or minimum performance error (see Eq. 4.5). The performance error at the time step k , $e(k)$, is simply obtained by normalizing the cost function, $\epsilon(k)$, by the total number of examples in the input data set, and it is given by,

$$e(k) = \frac{1}{N} \epsilon(k). \quad (4.5)$$

A decision boundary is created by the perceptron, and its dimensionality depends on the length of an input vector (or the length of an example in the input data set). As an illustration, suppose the length of input vector is two (p_1 and p_2), then the two possible outcomes (one or zero) of the network are determined by the value of the sum ($w_1 p_1 + w_2 p_2 + b$). The subscripts denote the elements of the input and weight vectors. From this, we can see that the 2-dimensional input space is divided into two regions. Depending on

the sign of the sum $(w_1p_1 + w_2p_2 + b)$, we find p_2 as

$$p_2 > -\frac{w_1p_1 - b}{w_2}, \quad (4.6)$$

$$p_2 < -\frac{w_1p_1 - b}{w_2}. \quad (4.7)$$

If we assume p_1 and p_2 are orthogonal axes, then the slope $-w_1/w_2$ and the intercept $-b/w_2$ form a boundary line. For the perceptron with an input vector of length R , the R -dimensional input space is dissected by an R -dimensional hyperplane into two regions.

Until now we have discussed the basic structures and mathematical properties of the perceptron. From now on, we focus our attention on the perceptron network in Fig. 4.4. It consists of S perceptrons (or neurons) in a single layer, and each input node takes an input vector of length R . There are S bias terms and S weight vectors. Each perceptron has its own weight vector, which is R -elements long. Such a network is much more flexible than the perceptron because it divides R -dimensional input space into 2^S regions by S sets of R -dimensional hyperplanes. For linearly separable classes, the number of output nodes (or number of perceptrons) in the network determines the maximum number of classes we can classify. Suppose a perceptron network has two neurons and each input node takes an input vector of length 3. This means that the 3-dimensional space is divided into 4 regions by 2 sets of 3-dimensional hyperplane. Since we have multiple neurons in the network, new subscript j is used to refer a particular perceptron. The variables a_j and b_j in the figure represent the output and bias of the j^{th} neuron, respectively. In the perceptron network, we have a weight matrix rather than a weight vector because each neuron has its own weight vector. The weight matrix (\tilde{W}) has R rows and S columns. If we supply the network with N input-target data pairs, then the input data set (\tilde{P}) has R rows and N columns, and the target data set (\tilde{T}) has S rows and N columns. The error between output and target values of the j^{th} -perceptron for the i^{th} -example at time step k , $E_{j,i}(k)$, is given by

$$E_{j,i}(k) = f\left(\sum_{l=1}^R w_{j,l}(k)p_{l,i} - t_{j,i}\right), \quad (4.8)$$

where $w_{j,l}$, $p_{l,i}$, and $t_{j,i}$ are elements of matrices \tilde{W} , \tilde{P} , and \tilde{T} , respectively. The cost function,

$\varepsilon(k)$, at time step k is written as

$$\varepsilon(k) = \frac{\sum_{j=1}^S \sum_{i=1}^N E_{j,i}^2}{2}. \quad (4.9)$$

We apply the steepest gradient algorithm, as before, to find the optimum weight matrix, \tilde{W}_{opt} by taking the derivative of the cost function with respect to the weight matrix. The weight matrix at time step $k+1$ is then given by

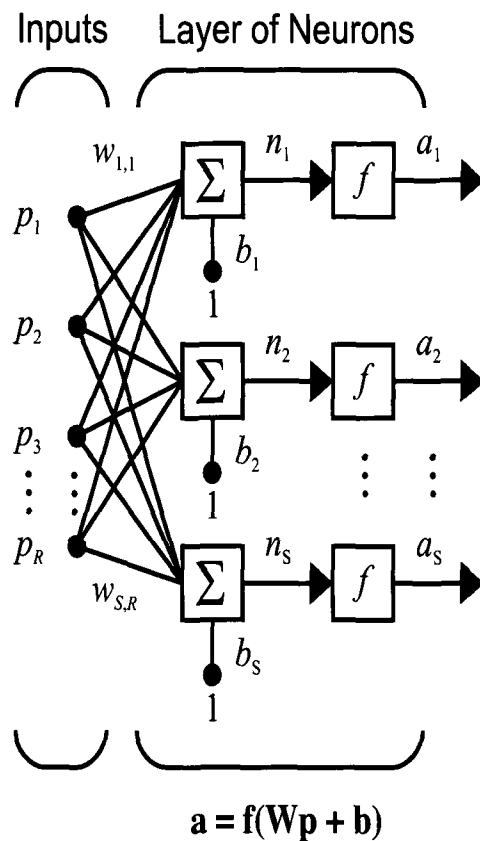
$$\tilde{W}(k+1) = \tilde{W}(k) - \gamma(\tilde{P}(\tilde{W}^T \tilde{P} - \tilde{T})^T). \quad (4.10)$$

In general it is recommended to use as few neurons (or perceptrons) as possible to avoid over-fitting of the network, but it is also possible to under-fit the network by using too few neurons [68, 70]. In both cases, the result is a poor generalization, therefore it is very important for the user to determine an optimum number of neurons by trial and error, and then use that number of neurons (or perceptrons) to construct a perceptron network.

We want to use an exclusive OR (XOR) function, as an example, to show a limitation of the perceptron. The XOR function is represented by the input matrix (P) and target row vector (T):

$$P = \begin{bmatrix} 0 & 1 & 0 & 1 \\ 0 & 0 & 1 & 1 \end{bmatrix}, \quad T = [0 \quad 1 \quad 1 \quad 0],$$

where 0 and 1 in the vector T are type 1 and 2 classes, respectively. Fig. 4.5 shows a graphical representation of the XOR function (A.U. \equiv artificial units). The red and blue circles denote the type one and type two classes, respectively. The two black lines are one set of many possible solutions to solve the XOR function. As we mentioned before, the perceptron can divide the 2-dimensional input space into only two regions by a single decision boundary, and thus it cannot solve this problem. There are two ways to solve the problem: One way is to use a perceptron network, consisting of two perceptrons; the other way is to modify the input matrix by introducing a third element, which is a product of two previous elements, in each of the input vectors. The latter solution will create a decision plane rather than a decision line, and the latter one is recommended over the first one because it uses fewer neurons (or perceptrons) to solve the problem.



Where

R = number of
elements in
input vector

S = number of
neurons in layer

Figure 4.4. A perceptron network. It consists of S perceptrons (or neurons) in parallel structure, and each input node takes an input vector of length R . There are S bias terms and S weight vectors. Each perceptron has its own weight vector, which is R -elements long. Such a network is much more flexible than a perceptron because it divides R -dimensional input space into 2^S regions by S sets of R -dimensional hyperplanes. See text for details.

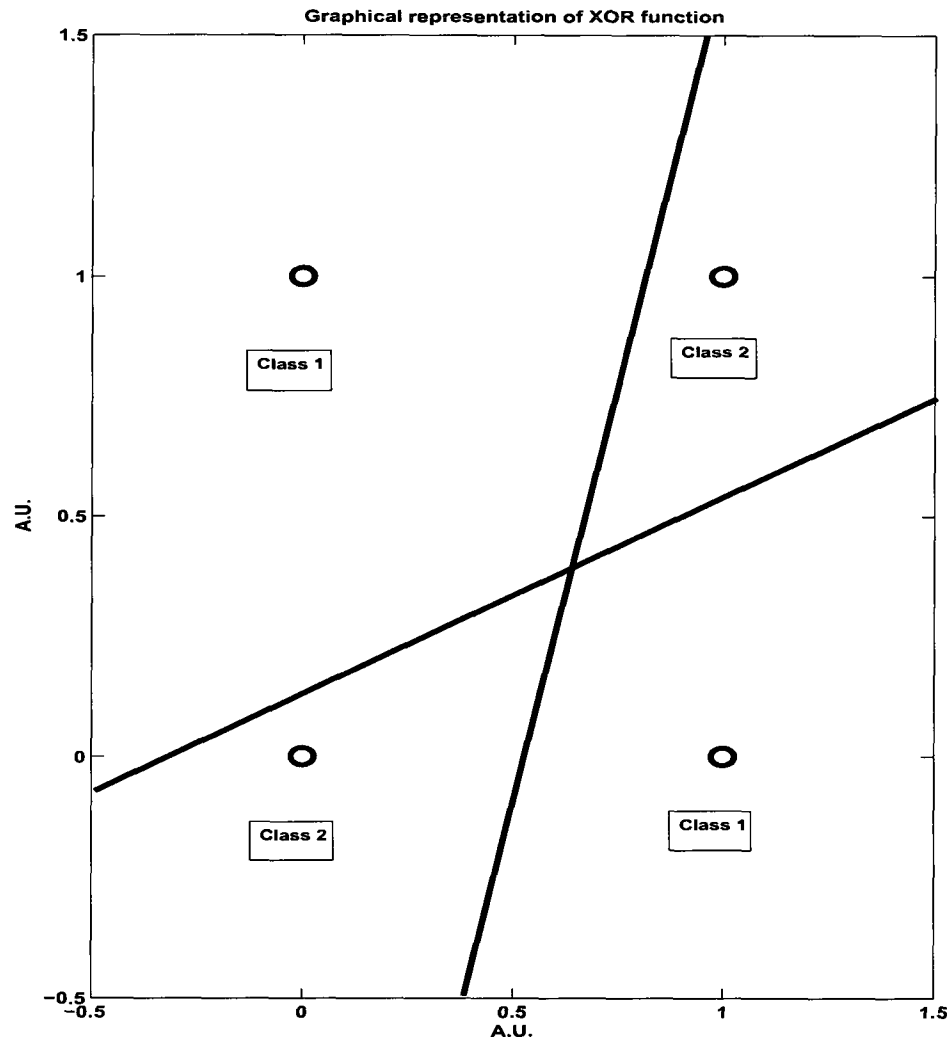


Figure 4.5. Graphical representation of XOR function. The red and blue circles denote the type one and type two classes, respectively. The two black lines are one set of many possible solutions to solve the XOR function. As discussed before, the perceptron can divide the 2-dimensional input space into only two regions by a single decision boundary, and thus it cannot solve this problem. A.U. \equiv artificial units.

4.3 Training and Validation of perceptron networks using Infrasound Data

The purpose of this thesis is to train a perceptron network to classify three classes of low-frequency signals: MAWs, HTVs, and clutter (anything not MAW or HTV, but having similar classification parameters). A proposed perceptron network consists of two perceptrons in a single layer, and each perceptron takes an input vector that is a three-elements long. The network is trained with a total of four data sets: MCCM- and SSVR2-based data sets for each of the Fairbanks and Antarctic arrays. Each column of the MCCM- and SSVR2-based data sets is a three-element feature vector (MCCM or SSVR2, V_t , and σ_τ), which represents a signal. The training data sets thoroughly represent the the input space, and we randomly selected examples from each class: 100 examples from MAWs and HTVs; 200 examples from clutter. Thus, each of the four data sets has 3 rows and 400 columns. Each variable in the input space is mapped between -1 and 1 to avoid a biased response of the network toward a particular variable. The columns of input data sets are randomly permuted to improve the learning process of the four networks. There are many ways to assign target vectors, but we choose to assign them as,

$$MAW \equiv \begin{bmatrix} 1 \\ 1 \end{bmatrix}, HTV \equiv \begin{bmatrix} 0 \\ 1 \end{bmatrix}, clutter \equiv \begin{bmatrix} 0 \\ 0 \end{bmatrix}.$$

We use the MATLABTM Neural Network Toolbox [80] to create, train, and validate the perceptron networks. The Toolbox implements Eq. 4.10 to train the network (or update the weight matrix \tilde{W}). We tried assigning different values to the target vectors and varied the maximum number of epochs to train the networks. We did not observe much of a difference in the network performance. Fig. 4.6 shows the performance error plots of the four perceptron networks as a function of epoch number. All four sub-plots are produced with the default learning rate (γ) of one, performance error goal of zero, maximum epoch number of 1,000, and minimum gradient change of zero. The training of the four perceptron network stops if any of the stopping criteria are met: a performance error goal and a maximum number of epochs, and a minimum gradient change. Plots in the left column of the figure are produced with the MCCM-based data sets, and plots in the right column

Table 4.1. Performance summary of the perceptron networks for I53US.

Detector	MCCM		SSVR2	
	CRs(%)	Events	CRs(%)	Events
MAWs	99.5	200	98.5	200
HTVs	97.5	200	100.0	200
clutter	94.0	400	100.0	400
Performance error	0.0225		0	

Table 4.2. Performance summary of the perceptron networks for I55US.

Detector	MCCM		SSVR2	
	CRs(%)	Events	CRs(%)	Events
MAWs	99.5	200	100.0	200
HTVs	92.5	200	100.0	200
clutter	95.0	400	100.0	400
Performance error	0.0175		0.0075	

of the figure are generated with the SSVR2-based data sets. The panels in top and bottom rows are created with the Fairbanks and Antarctic data sets, respectively. The SSVR2-based networks have lower performance errors than the MCCM-based networks.

The validation data sets exclude signals that are used for creating the training data sets, and they are generated in the same way the training data sets are produced. Tables 4.1 and 4.2 summarize the performance of four trained networks (MCCM- and SSVR2-based networks for the Fairbanks and Antarctic array) in terms of classification rates (CRs). The SSVR2-based networks have lower performance errors and have slightly higher classification rates than the MCCM-based networks. However, classification rates of all four networks are greater than 92%.

As the dimension of the input vector increases, it becomes harder to visualize the de-

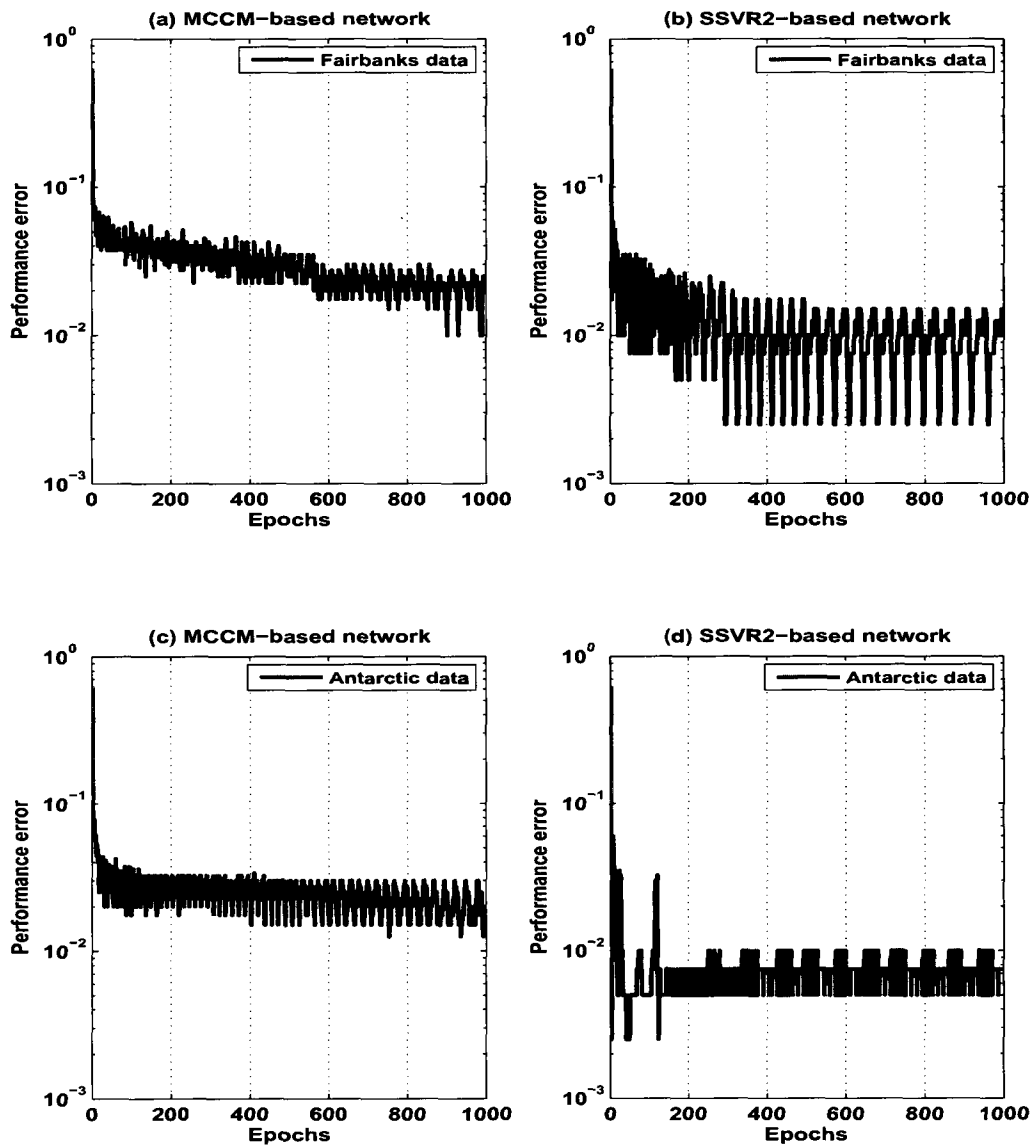


Figure 4.6. Performance error plots of four trained perceptron networks. (a) MCCM-based network, (b) SSVR2-based network, (c) MCCM-based network and (d) SSVR2-based network. (a)-(d) are produced with the default learning rate (γ) of one, performance error goal of zero, maximum epoch number of 1,000, and minimum gradient change of zero. (a) and (b) are produced with the Fairbanks data sets, and (c) and (d) are generated with the Antarctic data sets. The SSVR2-based networks have lower performance errors than the MCCM-based networks.

cision boundary created by each neuron in the perceptron network. In our problem, the input space is 3-dimensional, and so the decision boundary created by each neuron is a plane. Since our network has two neurons, the network will create four regions in the input space using two planes. We can visualize these four regions created by the perceptron network as a function of σ_τ . Figs. 4.7 and 4.8 illustrate the decision boundaries created by the MCCM- and SSVR2-based networks for the Fairbanks array. Each sub-plot is generated with outputs of the network, and such outputs are produced by feeding a three-element long feature vectors (MCCM or SSVR2, V_t , and σ_τ) to the networks. The MCCM, SSVR2, and V_t values are incremented by 0.01, 0.01, and 0.01 Km/s. Four different colored regions indicate areas occupied by different types of signals. The unknown signals are classified as the network outputs that do not belong to any of the assigned target vectors. It is important to realize that the true distribution of features for each class do not necessarily cover the whole region. The unknown regions for the SSVR2-based networks are much smaller than those of the MCCM-based networks.

4.4 Summary

We introduced a perceptron with its structure, mathematical properties, and limitations. Since the perceptron is only capable of distinguishing two linearly separable classes, a more advanced network is needed to classify our three low-frequency signals: MAWs, HTVs, and clutter. The proposed network is a perceptron network consisting of two perceptrons in parallel, and each perceptron takes an input vector that is three-elements long. A total of four perceptron networks are trained and validated based on the type of detection algorithm (MCCM or SSVR2) and data source (Fairbanks or Antarctica).

We use the parameter selection criteria defined in Tables 3.1 and 3.2 to create training and validation input data sets, and each data set consists of three-elements long feature vectors (MCCM or SSVR2, V_t , and σ_τ). The validation data sets exclude signals that are used for creating the training data sets. The target vectors for the training and validation data sets are assigned by the user. These data sets are then used to train and validate four

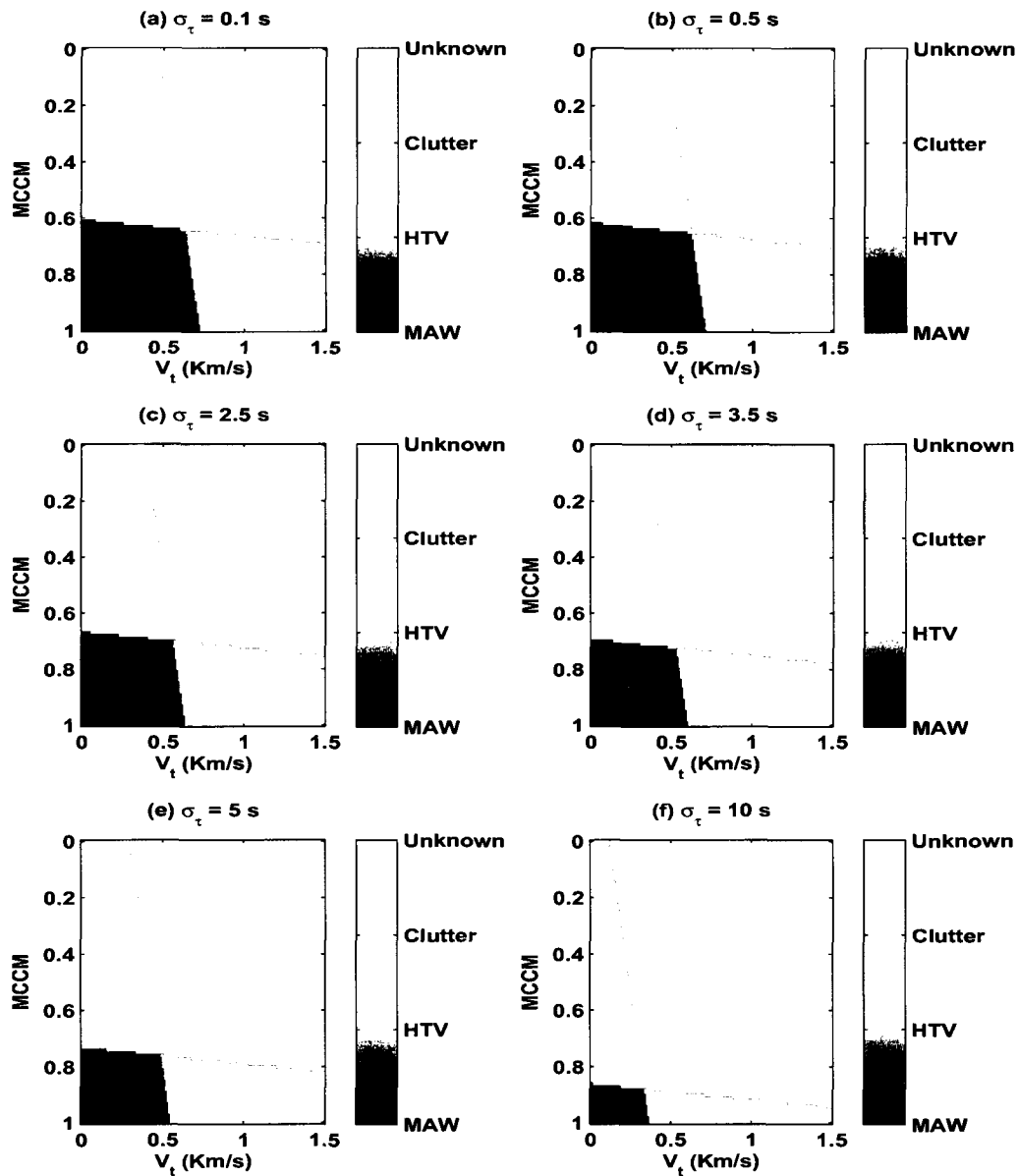


Figure 4.7. Decision boundaries of the MCCM-based network for I53US. (a) $\sigma_\tau = 0.1$ s, (b) $\sigma_\tau = 0.5$ s, (c) $\sigma_\tau = 2.5$ s, (d) $\sigma_\tau = 3.5$ s, (e) $\sigma_\tau = 5$ s, (f) $\sigma_\tau = 10$ s. (a)-(f) is generated by feeding a three-element long feature vectors (MCCM, V_t , and σ_τ) to the networks. The MCCM and V_t values are incremented by 0.01 and 0.01 Km/s, respectively. Four different colored regions indicate areas occupied by different types of signals. The unassigned network outputs are classified as unknown signals. Notice that the detection areas for the MAWs and HTVs reduce with increasing planarity (σ_τ) values.

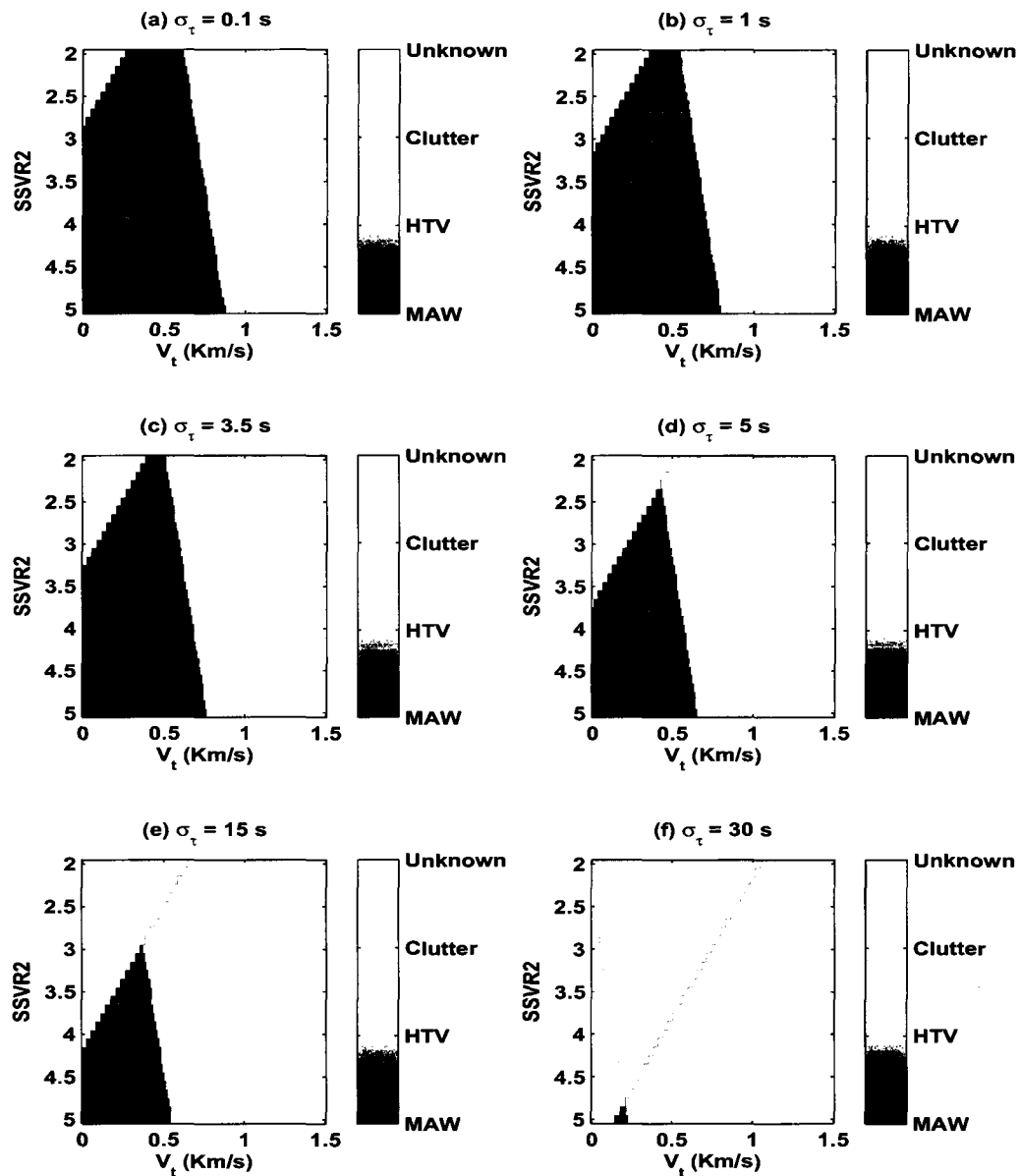


Figure 4.8. Decision boundaries of the SSVR2-based network for I53US. (a) $\sigma_\tau = 0.1$ s, (b) $\sigma_\tau = 1.0$ s, (c) $\sigma_\tau = 3.5$ s, (d) $\sigma_\tau = 5.0$ s, (e) $\sigma_\tau = 15$ s, (f) $\sigma_\tau = 30$ s. (a)-(f) is generated by feeding a three-element long feature vectors (SSVR2, V_t , and σ_τ) to the networks. The SSVR2 and V_t values are incremented by 0.01 and 0.01 Km/s, respectively. Four different colored regions indicate areas occupied by different types of signals. The unassigned network outputs are classified as unknown signals. Notice that the detection area for the clutter increases with increasing planarity (σ_τ) values, and the unknown regions in the figure are much smaller than those in Fig. 4.7.

perceptron networks: MCCM- and SSVR2-based networks for the Fairbanks and Antarctic arrays. Following training parameters are applied to the all four networks: learning rate (γ) is one; performance error goal is zero; maximum epoch number is 1,000; minimum gradient change is zero. The training data sets thoroughly represent the the input space, and we randomly selected examples from each class: 100 examples from MAWs and HTVs; 200 examples from clutter. The SSVR2-based networks train faster (refer to Figs. 4.6(b) and 4.6(d)) than the MCCM-based networks (see Figs. 4.6(a) and 4.6(c)) with smaller performance errors. Tables 4.1 and 4.2 show validation results of the four trained networks, and classification results of them are greater than 92%.

Figs. 4.7 and 4.8 illustrate decision boundaries created by the trained networks for the Fairbanks array as a function of σ_τ . The unassigned network outputs are classified as unknown signals. The unknown regions of the MCCM-based networks are much larger than those of SSVR2-based networks. It is important to realize that the true distribution of feature space for each class do not necessarily cover the whole region depicted in both figures.

In the next chapter, we will compare the outputs of our trained networks against the expert analysis of Prof. Charles. R. Wilson using 2008 Fairbanks data. These data sets were not used to train our perceptron networks. We will present the comparison results in graphical form, using modified detection summary plots.

Chapter 5

Neural Networks: Comparison

5.1 Abstract

In this chapter we test the trained networks developed in Chapter 4 against the expert Prof. Charles R. Wilson, who has been studying the MAWs and HTVs for decades. He selected seven days of high MAW activity and six days of high HTV activity from the 2008 Fairbanks data to create comparison data set. Note that the data set is not used for the training or validating our neural networks. The comparison is made in a graphical form using modified detection summary plots.

5.2 Comparison of Perceptron Network Classification against Human Expert Classification

Prof. Charles R. Wilson, who is considered to be an expert in the study of MAWs and HTVs, exclusively uses the infrasound detection summary plots and the magnetic disturbance data from CIGO to identify possible sources of low-frequency signals. The Detection summary plot (described in Chapter 2) is modified to include outputs from the MCCM- and SSVR2-based networks for easier comparison. We first present seven days of high MAW activity (Figs. 5.1-5.7) followed by six days of high HTV activity (Figs. 5.8-5.13) from the 2008 Fairbanks data.

Fig. 5.1, for example, displays modified detection summary plot of low-frequency signals observed at the Fairbanks array on January 6, 2008. The data were band-pass filtered from 0.015 to 0.1 Hz, and 10,000 points (or 500 seconds) window was used to estimate characterization parameters. The top two sub-plots in the figure depict histograms of the MCCM and SSVR2 detectors with thresholds indicated by red lines. Based on the statistical studies performed in Chapter 3, thresholds for the MCCM and SSVR2 for the Fairbanks array are determined to be 0.7 and 2.7, respectively. Next five panels show SSVR2, MCCM, V_t , θ , and σ_τ as a function of time. In each of the five panels, a blue “x” represents an estimated parameter for the window size. In the SSVR2 plot, the threshold is

indicated by a red line, and events with SSVR2 value less than 2.7 are enclosed by green circles. In the other four panels, events with an MCCM value greater than 0.7 are enclosed by red circles. The bottom two panels show outputs from the MCCM- and SSVR2-based perceptron networks. The network outputs are converted to numbers between one and four, and different colors are used to display them: the green, blue, black, and red “×”s indicate MAWs, HTVs, clutter, and unknown signal, respectively. Strong MAW activity is observed throughout the day with an azimuth directed toward the Alaska and Aleutian Ranges (250° to 300°), and the V_t values are clustered around 0.5 Km/s. We also observe occasional HTV activity throughout the day. The changes in magnetic activity is divided into four groups: quiet if the peak-to-peak disturbance of H, D, and Z magnetic components are all under 50 nT; weak if the peak-to-peak disturbance of H magnetic component is greater than 50 nT but less than 250 nT; intermediate if the peak-to-peak disturbance of H magnetic component is greater than 250 nT but less than 1,000 nT; strong if peak to peak disturbance of H magnetic component is greater than 1,000 nT. The CIGO recorded intermediate magnetic disturbances from 08:00 to 16:00 UT on January 6, 2008. The rest of modified detection summary plots (Figs. 5.1-5.13) are produced by taking the same steps used to generate Fig. 5.1.

Our neural networks make their decisions based on the characterization parameters (MCCM or SSVR2, V_t , and σ_τ). Since the classification of the MAWs from HTVs is based on the V_t value, our network outputs are as good as the accuracy of V_t estimate. Unfortunately, there is a relatively large amount of uncertainty associated with the V_t estimation. For example, a signal with estimated trace velocity value of 800 m/s (and $\sigma_\tau = 0.3$ s) can have an error as much ± 350 m/s (ref to Fig. 1.6). The uncertainty becomes larger, as the V_t and σ_τ increases. As a result, it is possible to classify signals as HTVs when they are actually MAWs, and vice versa. Therefore, we should utilize other known features (e.g., persistence in azimuth for MAWs) of these signals whenever we can. When analysing the modified detection summary plots, we should keep such possibilities in mind.

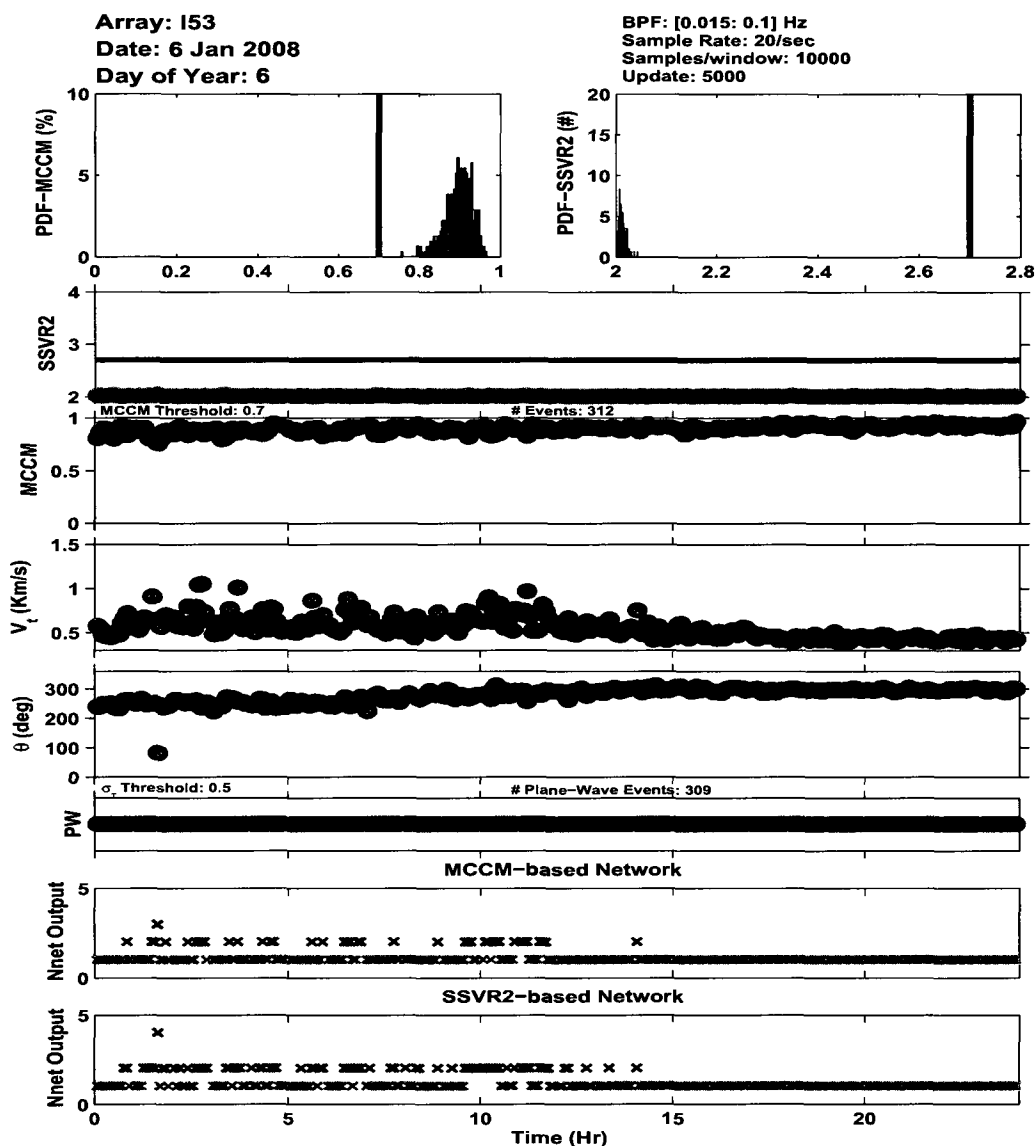


Figure 5.1. MAW detection using MCM- and SSVR2-based networks (case 1). The expert determined that MAW activity is present all day on January 6, 2008 with an azimuth directed toward the Alaska and Aleutian Ranges (250° to 300°). Outputs from the MCM- and SSVR2-based networks show that strong MAW activity (green "x"s) is present all day with occasional HTV activity (blue "x"s). Intermediate magnetic disturbances were recorded from 08:00 to 16:00 UT at CIGO College.

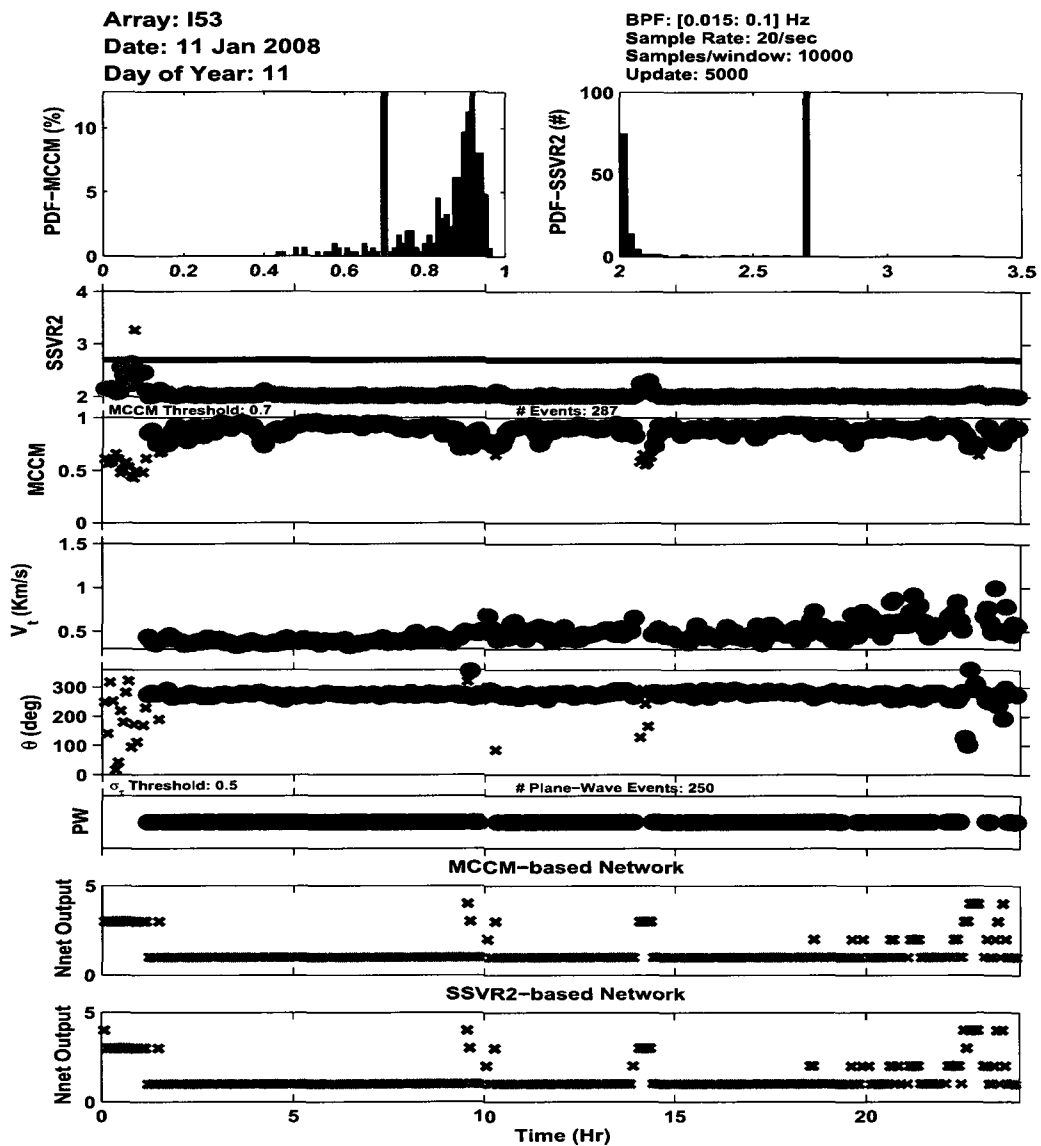


Figure 5.2. MAW detection using MCCM- and SSVR2-based networks (case 2). The expert determined that MAW activity is present from 01:00 to 23:00 UT on January 11, 2008 with an azimuth directed toward the Alaska and Aleutian Ranges (250° to 300°). Outputs from the MCCM- and SSVR2-based networks show that strong MAW activity (green "x"s) is present all day with very little HTV activity (blue "x"s). Magnetic disturbances were quiet all day at CIGO College.

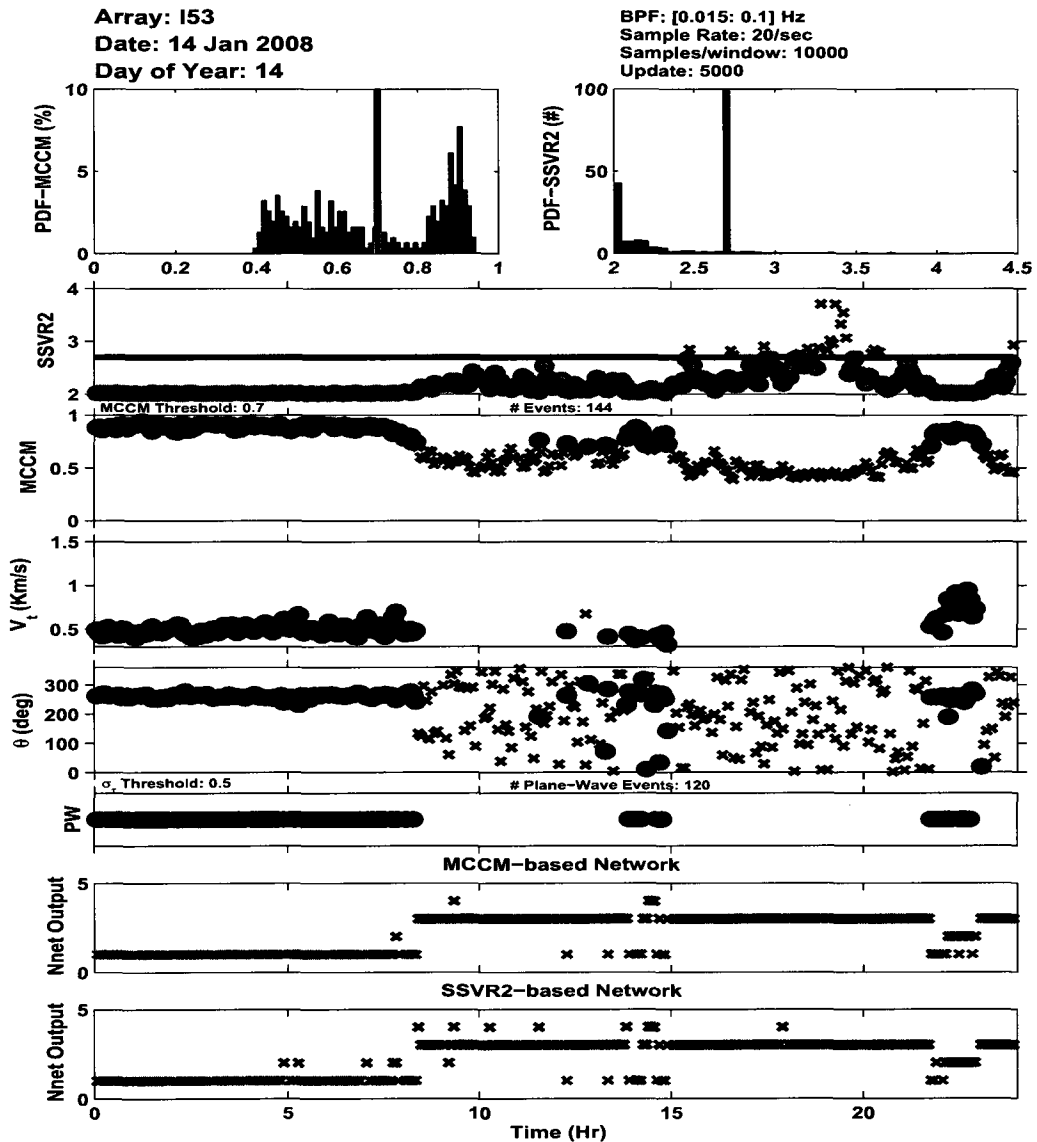


Figure 5.3. MAW detection using MCCM- and SSVR2-based networks (case 3). The expert determined that MAW activity is present from 00:00 to 08:00 UT on January 14, 2008 with an azimuth directed toward the Alaska and Aleutian Ranges (250° to 300°). Outputs from the MCCM- and SSVR2-based networks show the presence of strong MAW activity (green "x"s) during the same time period with occasional HTV activity (blue "x"s). Strong magnetic disturbances were recorded from 08:00 to 20:00 UT at CIGO College.

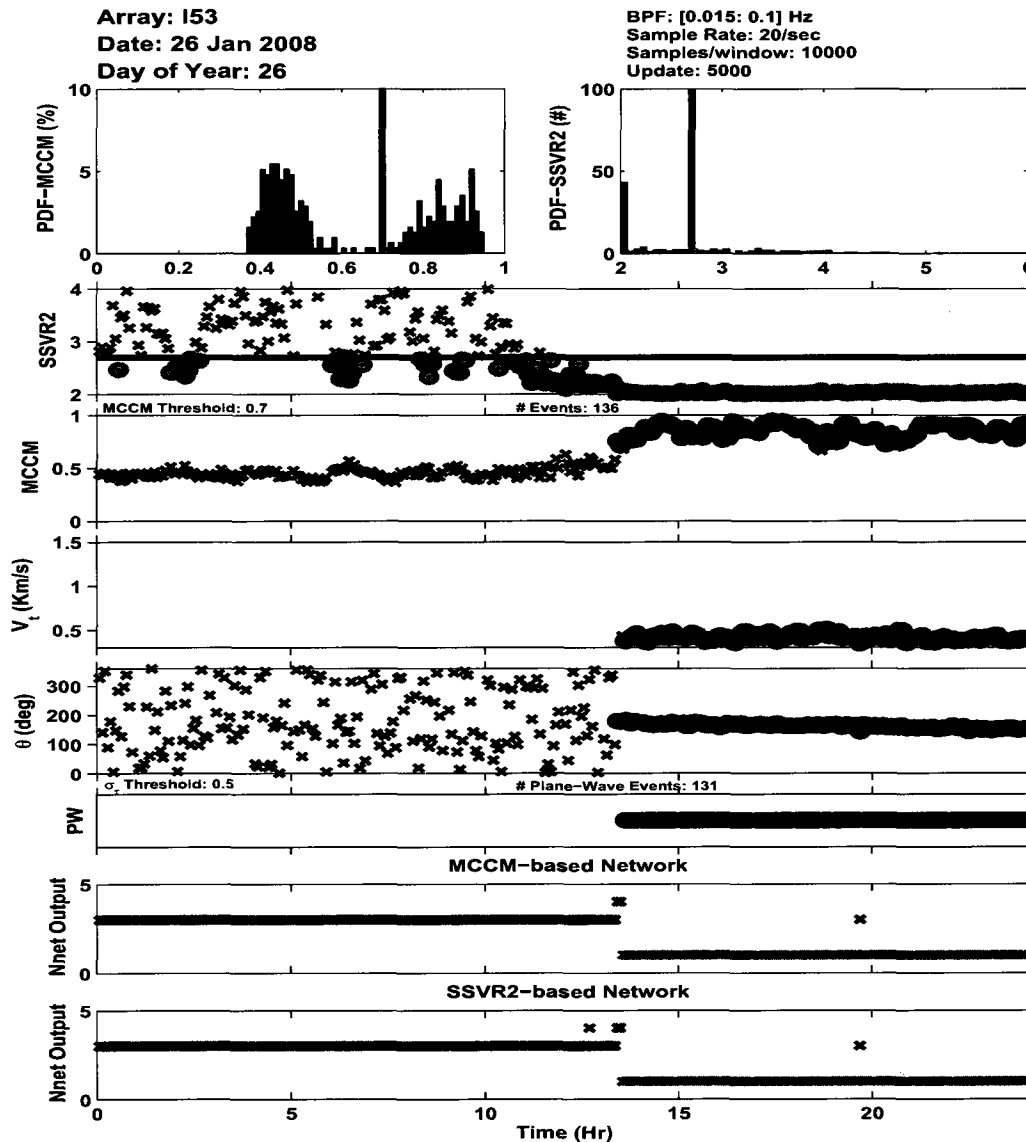


Figure 5.4. MAW detection using MCCM- and SSVR2-based networks (case 4). The expert determined that MAW activity is present from 14:00 to 24:00 UT on January 26, 2008 with an azimuth drifting from 180° to 150° . Outputs from the MCCM- and SSVR2-based networks show the presence of strong MAW activity (green "x"s) during the same time period with no HTV activity (blue "x"s). Weak magnetic disturbances were recorded from 09:00 to 14:00 UT at CIGO College.

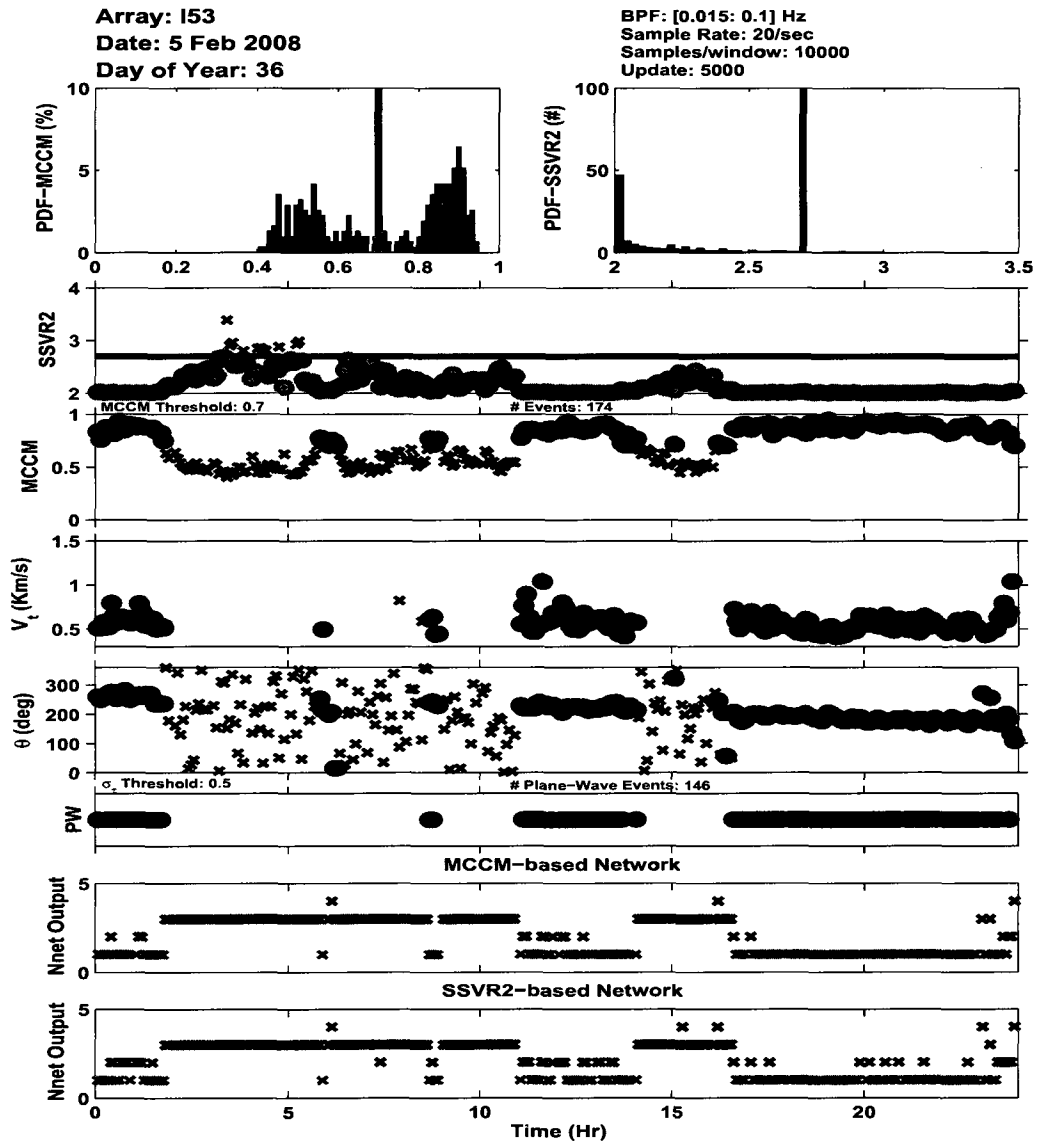


Figure 5.5. MAW detection using MCCM- and SSVR2-based networks (case 5). The expert determined that MAW activity is present from 00:00 to 02:00 UT, from 11:00 to 14:00 UT, and from 17:00 to 24:00 UT on February 5, 2008 with an azimuth drifting from 280° to 180° . Outputs from the MCCM- and SSVR2-based networks show the presence of strong MAW activity (green "x"s) during the same time period with occasional HTV activity (blue "x"s). Magnetic disturbances were quiet all day at CIGO College.

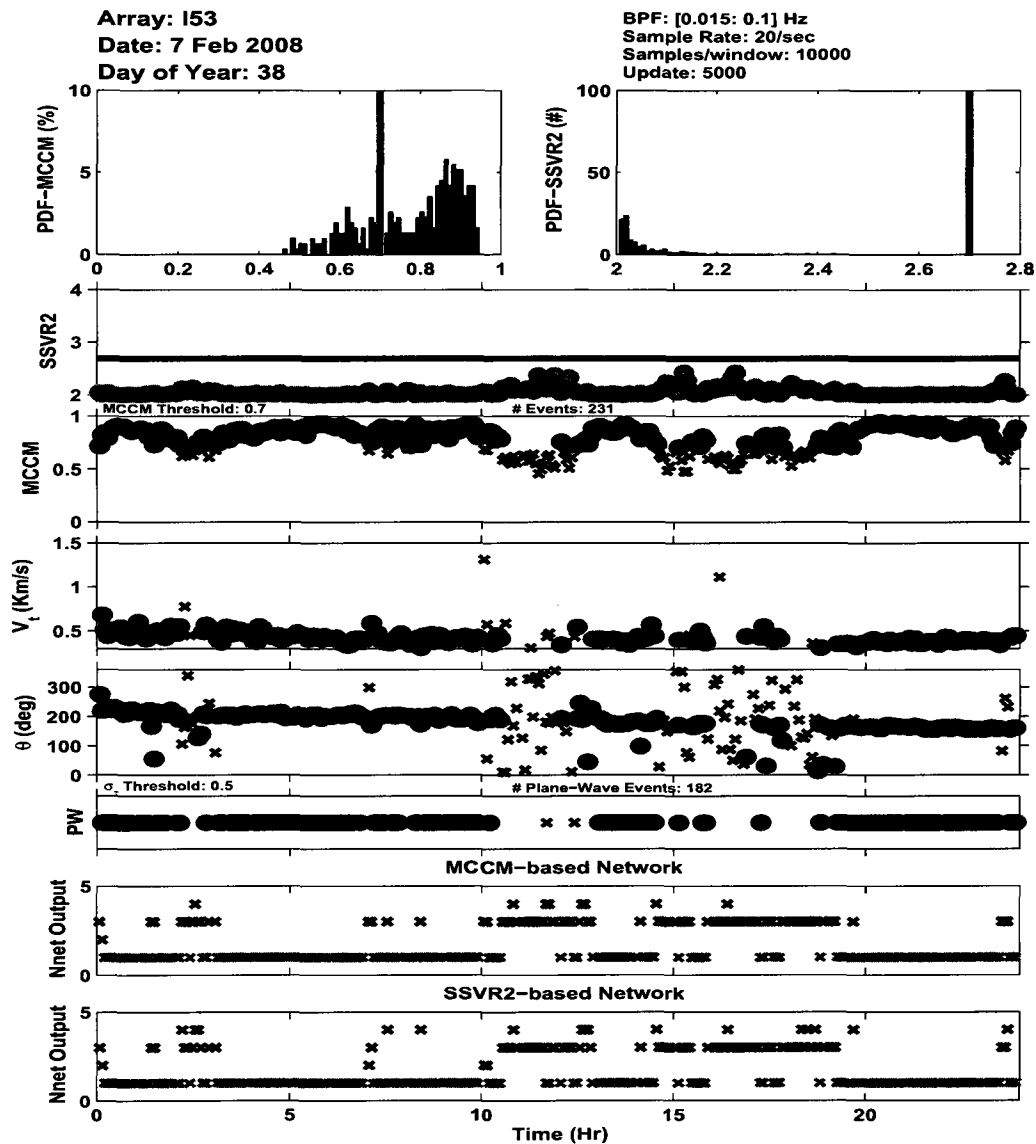


Figure 5.6. MAW detection using MCCM- and SSVR2-based networks (case 6). The expert determined that MAW activity is present all day on February 7, 2008 with an azimuth directed toward the Alaska and Aleutian Ranges (250° to 300°). Outputs from the MCCM- and SSVR2-based networks show that strong MAW activity (green "x"s) is present throughout the day with little HTV activity (blue "x"s). Weak magnetic disturbances were recorded from 16:00 to 18:00 UT at CIGO College.

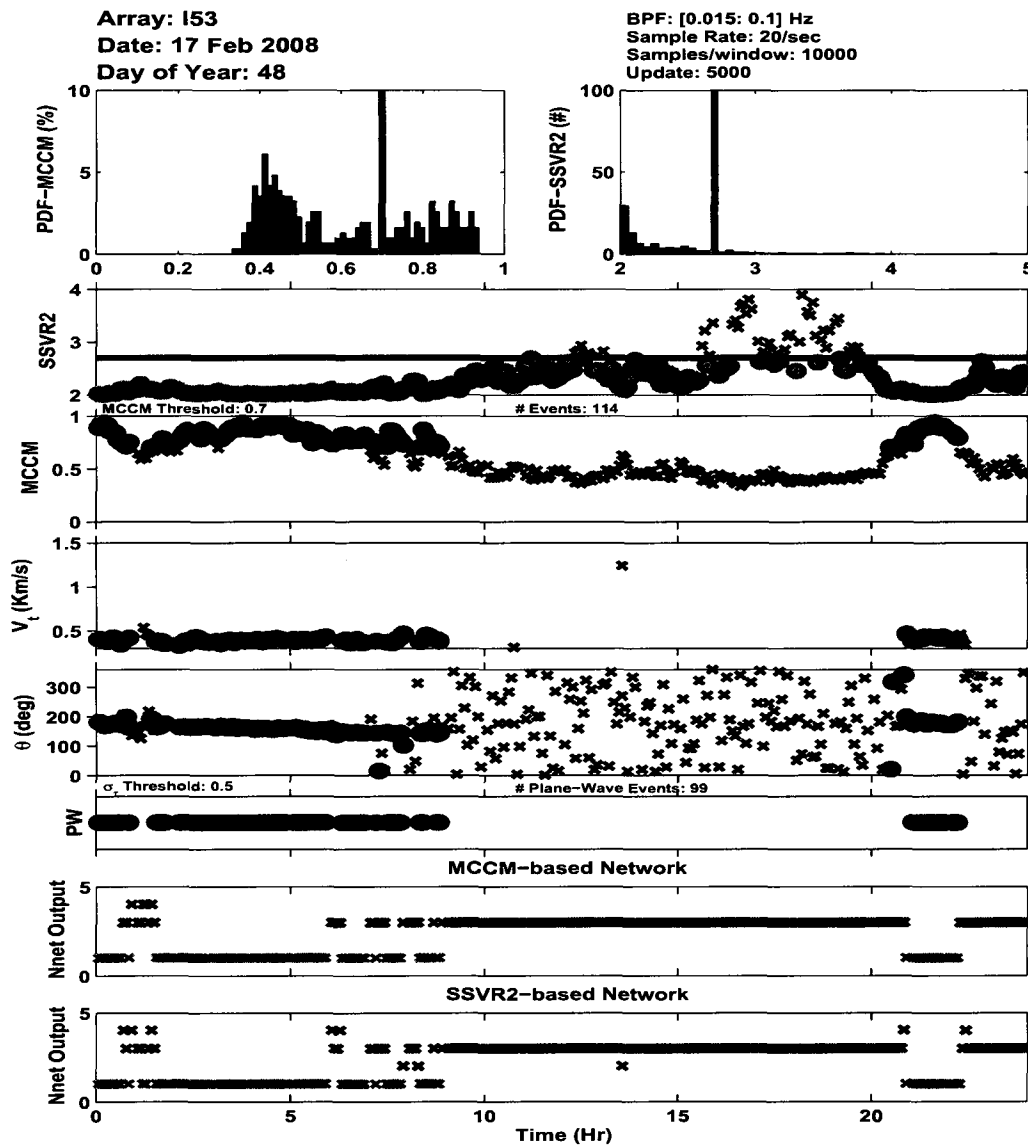


Figure 5.7. MAW detection using MCCM- and SSVR2-based networks (case 7). The expert determined that MAW activity is present from 00:00 to 08:00 UT, and from 21:00 to 23:00 UT on February 17, 2008 with an azimuth drifting from 180° to 150° . Outputs from the MCCM- and SSVR2-based networks show the presence of strong MAW activity (green "x"s) during the same time period with very little HTV activity (blue "x"s). Weak magnetic disturbances were recorded from 08:00 to 16:00 UT at CIGO College.

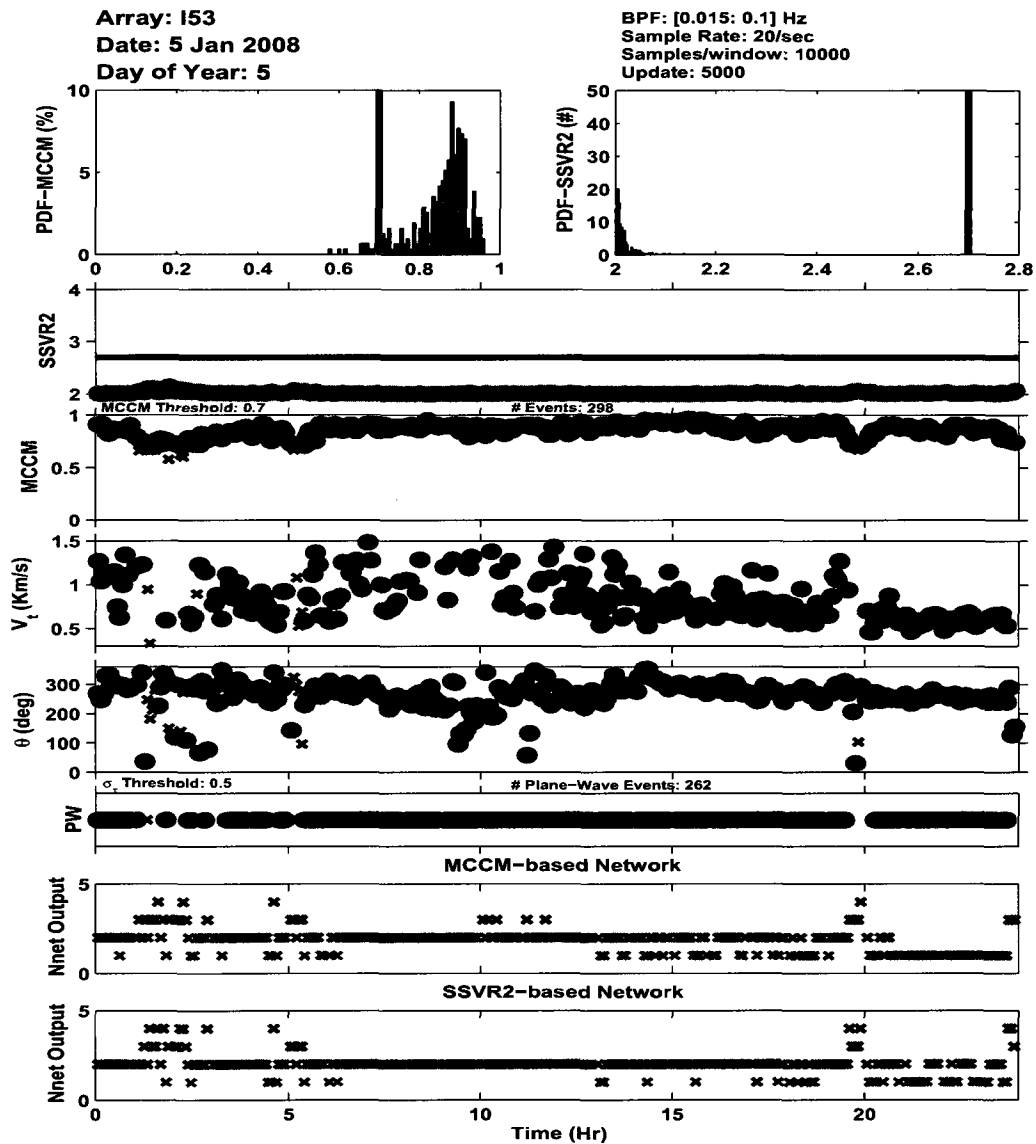


Figure 5.8. HTV detection using MCCM- and SSVR2-based networks (case 1). The expert determined that HTV activity is present from 00:00 to 20:00 UT on January 5, 2008 with scattered azimuth. Outputs from the MCCM- and SSVR2-based networks show the presence of strong HTV activity (blue "x"s) during the same time period with occasional MAW activity (green "x"s). Strong magnetic disturbances were recorded from 09:00 to 16:00 UT at CIGO College.

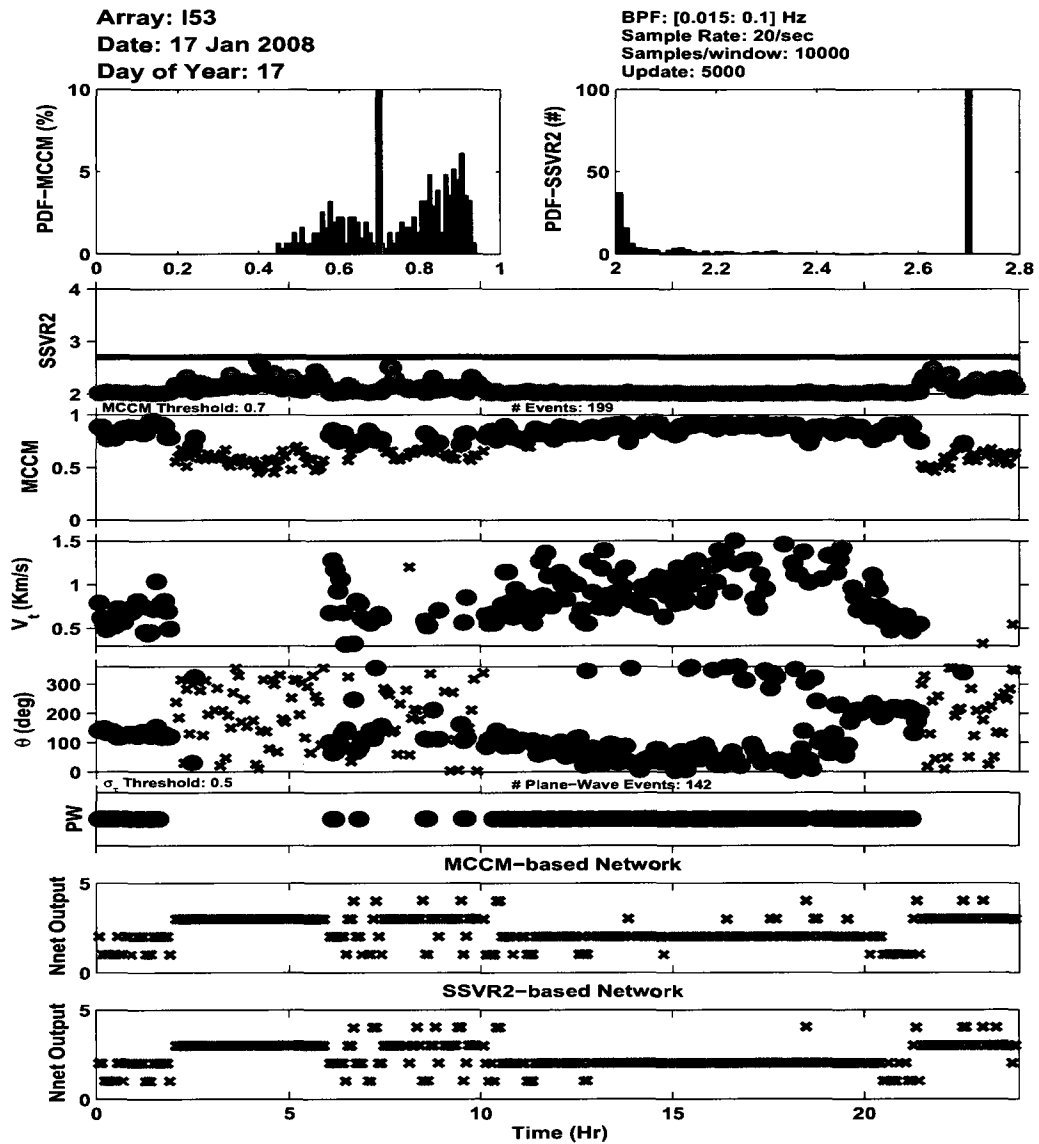


Figure 5.9. HTV detection using MCCM- and SSVR2-based networks (case 2). The expert determined that HTV activity is present from 00:00 to 02:00 UT and from 10:00 to 22:00 UT on January 17, 2008 with scattered azimuth. Outputs from the MCCM- and SSVR2-based networks show the presence of strong HTV activity (blue "x"s) during the same time period with occasional MAW activity (green "x"s). Intermediate magnetic disturbances were recorded from 00:00 to 02:00 UT and from 10:00 to 22:00 UT at CIGO College.

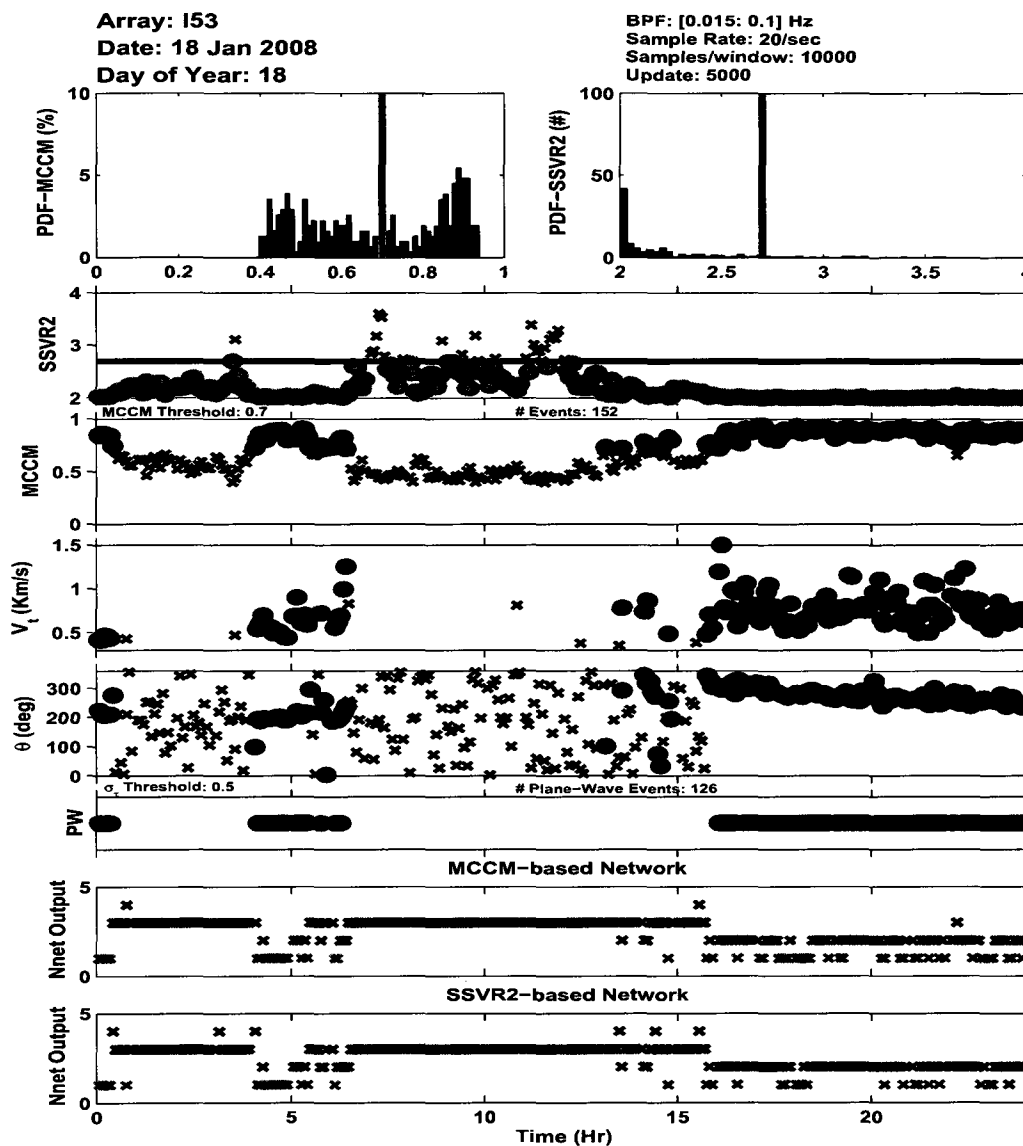


Figure 5.10. HTV detection using MCCM- and SSVR2-based networks (case 3). The expert determined that HTV activity is present from 16:00 to 24:00 UT on January 18, 2008 with scattered azimuth. Outputs from the MCCM- and SSVR2-based networks show the presence of strong HTV activity (blue "x"s) from 16:00 to 24:00 UT with occasional MAW activity (green "x"s). Intermediate magnetic disturbances were recorded from 08:00 to 20:00 UT at CIGO College.

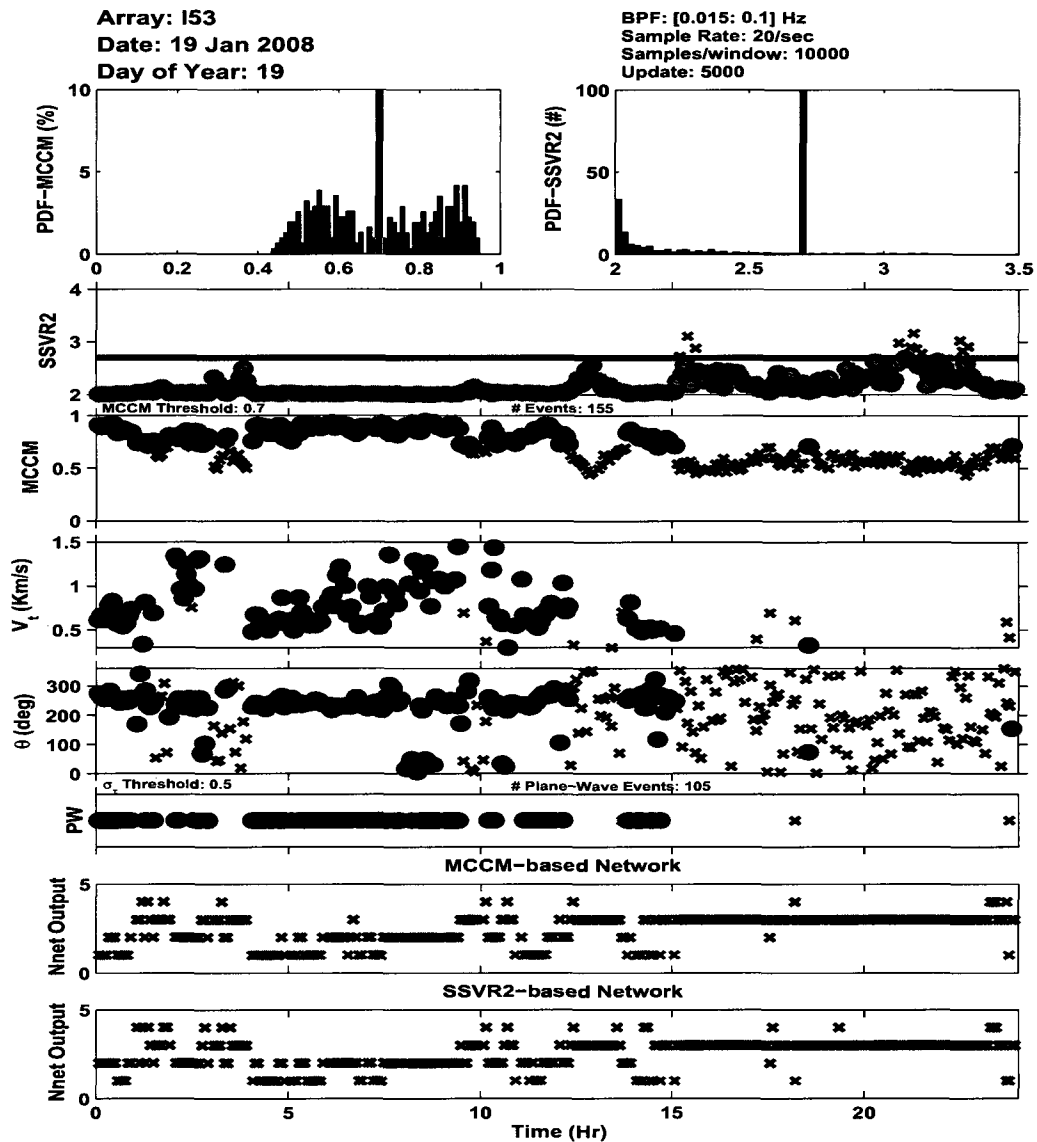


Figure 5.11. HTV detection using MCCM- and SSVR2-based networks (case 4). The expert determined that HTV activity is present from 00:00 to 13:00 UT on January 19, 2008 with scattered azimuth. Outputs from the MCCM- and SSVR2-based networks show the presence of HTV activity (blue "x"s) during the same time period with occasional MAW activity (green "x"s). Strong magnetic disturbances were recorded from 06:00 to 20:00 UT at CIGO College.

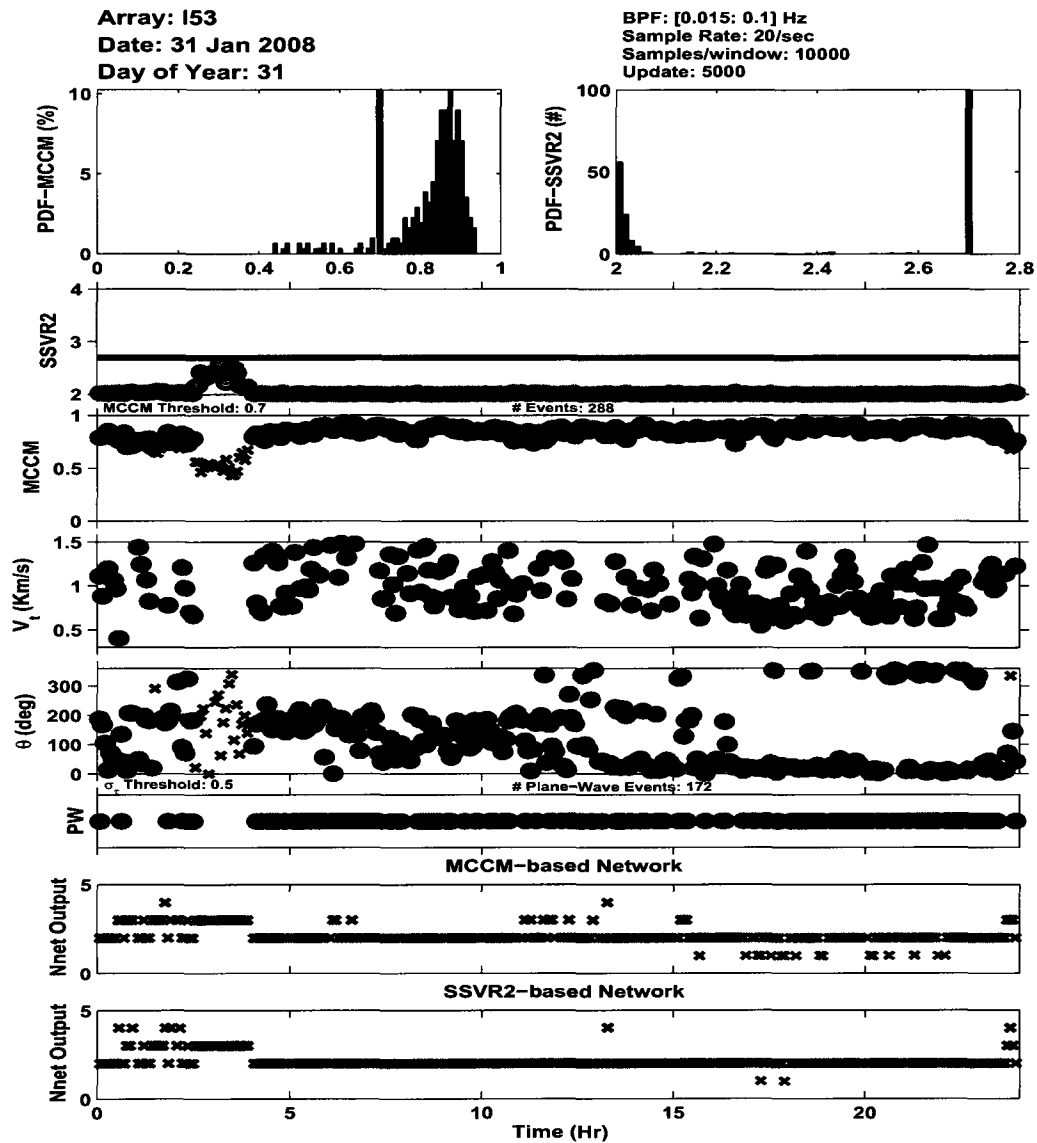


Figure 5.12. HTV detection using MCCM- and SSVR2-based networks (case 5). The expert determined that HTV activity is present from 04:00 to 24:00 UT on January 31, 2008 with scattered azimuth. Outputs from the MCCM- and SSVR2-based networks show the presence of strong HTV activity (blue "x"s) during the same time period with very little MAW activity (green "x"s). Magnetic disturbances were quiet all day at CIGO College.

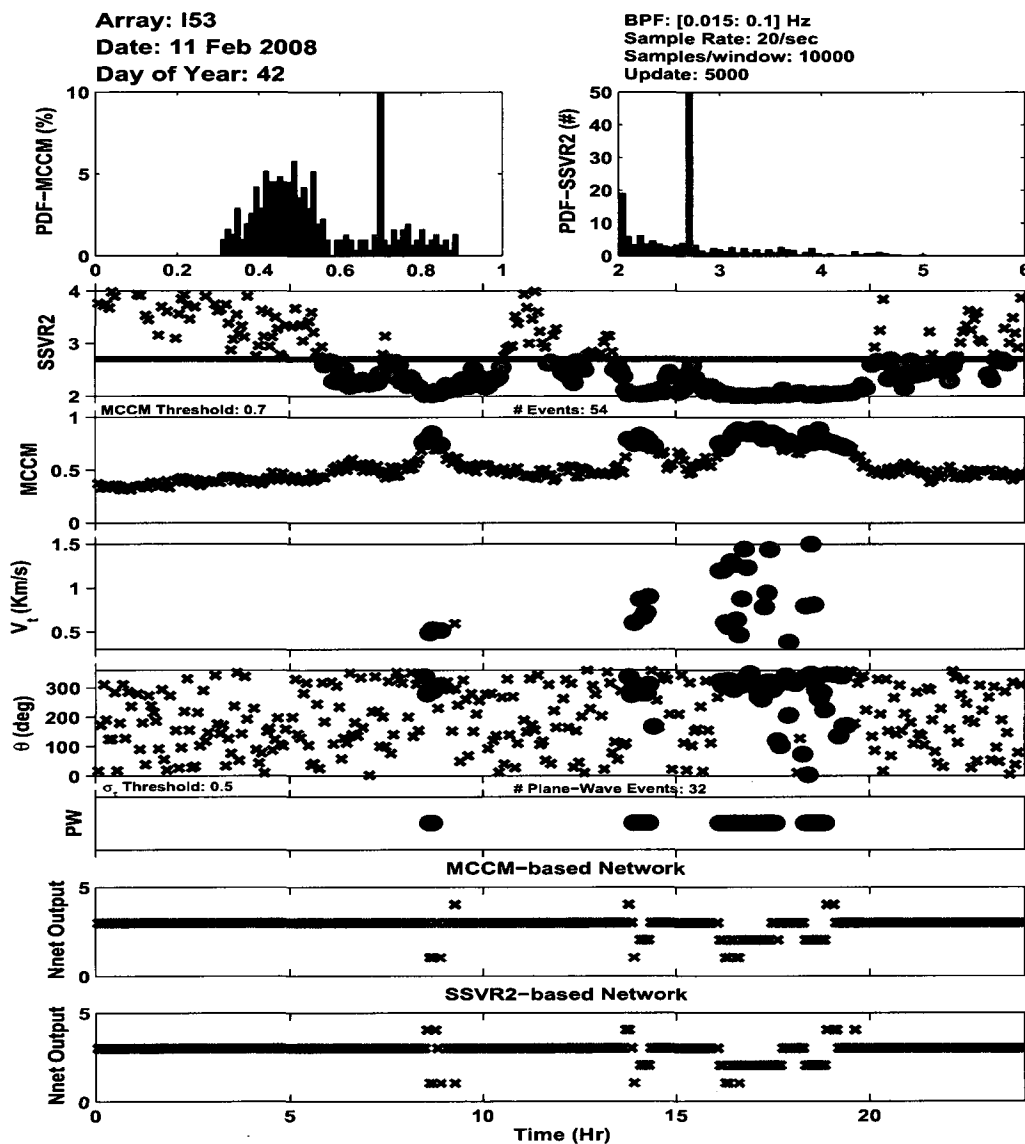


Figure 5.13. HTV detection using MCCM- and SSVR2-based networks (case 6). The expert determined that HTV activity is present from 14:00 to 18:00 UT on February 11, 2008 with scattered azimuth. Outputs from the MCCM- and SSVR2-based networks show the presence of HTV activity (blue "x"s) during the same time period with little MAW activity (green "x"s). Strong magnetic disturbances were recorded from 08:00 to 18:00 UT at CIGO College.

5.3 Summary

Prof. Charles R. Wilson selected seven days of high MAW activity and six days of high HTV activity from the 2008 Fairbanks data. These data sets were new to our neural networks. The trained MCCM- and SSVR2-based networks were tested against the expert analysis (refer to captions in Figs. 5.1-5.13). Expert identified MAW and HTV events are comparable to the outputs by the MCCM- and SSVR2-based networks. Colors and numbers are assigned to the network outputs: green and one for MAWs; blue and two for HTVs; black and three for clutters; red and four for unknown signals. The SSVR2 detector is far more sensitive than the MCCM detector and selects far more events. However, these events have large σ_τ values and low V_t values, and the SSVR2-based network successfully classified them as clutter and unknowns. Few unknown outputs are produced by our networks, and they can be reduced by adding more examples to the training data sets in order to cover the input space more thoroughly. Overall, the network outputs are comparable to the expert analysis, and outputs from both networks are very similar to each other. Therefore, we conclude that it is possible to automate our classification problem at the accuracy of expert level using our neural networks. These networks have several advantages over the human operator: first, they are robust; second, they are resistant to human errors; finally, they produce consistently unbiased results.

Chapter 6

Conclusions

6.1 Summary

We can summarize the main objective of this dissertation in two brief sentences. We can separate mountain associated waves (MAWs) from high trace velocity signals (HTVs) using the trace velocity (V_t). We can use neural networks to automate the classification of three low-frequency infrasound signals (MAWs, HTVs, and clutter) at the expert level.

We developed new detection algorithms (SSVR1 and SSVR2) that are based on principle component analysis. For high-frequency signal with white noise and SNR of -5 dB, for instance, the F-stat, MCCM, SSVR1, and SSVR2 detectors reach 100% TP roughly at 100%, 70%, 0%, and 40% FP (refer to Fig. 3.1). With pink noise and SNR of -5 dB, the F-stat, MCCM, SSVR1, and SSVR2 detectors reach 100% TP roughly at 100%, 90%, 30%, and 100% FP (see Fig. 3.4). Thus, the SSVR1 detector outperforms the other three detectors for the high frequency signal, as the SNR decreases. For low-frequency signals with white noise and SNR of -5 dB, for example, the F-stat, MCCM, SSVR1, and SSVR2 detectors reach 100% TP roughly at 100%, 90%, 95%, and 0% FP (refer to Fig. 3.3). With pink noise and SNR of -5 dB, the F-stat, MCCM, SSVR1, and SSVR2 detectors reaches 100% TP roughly at 100%, 95%, 100%, and 5% FP (see Fig. 3.6). We observe similar detector behaviors for microbaroms as those of the low-frequency signals (refer to Fig. 3.2 and 3.5). For microbaroms and low-frequency signals, the SSVR2 detector outperforms the other three detectors, as the SNR decreases. In addition, the SSVR-based detectors are computationally very efficient. For instance, speed improvement of MCCM detector to SSVR2 detector increases exponentially, as the number of sensors increases (see Fig. 3.7). This has implications for planned deployments of arrays with large numbers of sensors. On the other hand, the speed improvement of F-stat detector to SSVR2 detector roughly remains the same, as the number of sensors increases.

The two detection algorithms (MCCM and SSVR2) are compared with each other using infrasound data from both the Fairbanks and Antarctic arrays for a period of four

years (2004-2007). We find that the two detection methods produce similar results (refer to Figs. 3.10 and 3.19). The analysis of the Fairbanks data for the past four years (2004-2007) suggests that three dominant mountain ranges for the MAW sources in Alaska include the Saint Elias Range, the Alaska and Aleutian Ranges, and possibly the Seward and Chukotsk Peninsulas (see Fig. 3.11). The analysis of the Antarctic array data for the past four years (2004-2007) indicates the dominant MAW source is the Alps Range of the South Island, New Zealand (refer to Fig. 3.20).

We observe a global peak around 15:00 UT in the UT variations of the HTVs at the Fairbanks array, and such a peak is consistently observed in each year between 2004 and 2007 (see Fig. 3.13). However, we do not observe any patterns in the UT variations of the MAWs at the Fairbanks array. In contrast, we observe a global peak around 5:00 UT in the UT variations of the MAWs at the Antarctic array, and such a peak is consistently observed in each year between 2004 and 2007 (refer to Fig. 3.22). We do not observe any patterns in the UT variations of the HTVs at the Antarctic array. The MAWs and HTVs are active in the first and fourth quarters and quite in the second and third quarters for both the Fairbanks and Antarctic arrays (see Figs. 3.16 and 3.24).

Both the HTV activity at the Fairbanks array and the disturbances in magnetic activity recorded at CIGO College are most likely to occur between 5:00 and 18:00 UT (refer to Figs. 3.13, 3.14 and 3.17). We detect far more HTV activity at the Fairbanks array than at the Antarctic array because of the higher magnetic latitude of the Antarctic array (77° South Vs. 64° North). We also detect much less MAW activity at the Antarctic array than at the Fairbanks array. This is possibly due to fewer close-by mountain ranges near Windless Bight, Antarctica, where the array is located.

We constructed four perceptron networks, each consisting of two neurons (or perceptrons) in a single layer. Each input node takes a three-element long feature vector (MCCM or SSVR2, V_t , and σ_t). A total of four perceptron networks (the MCCM- and SSVR2-based networks for the Fairbanks and Antarctic arrays) were trained and validated. The input data sets used for training and validating the networks consisted of several examples (or

feature vectors) and they were chosen based on the selection criteria listed in Tables 3.1 and 3.2. The target vectors were assigned by the user, and Fig. 4.6 shows the training process of the four networks, as a function of epoch number. The MCCM- and SSVVR2-based networks were tested using the validation data sets, and all four networks yield the classification rates higher than 92% (refer to Tables 4.1 and 4.2). Figs. 4.7 and 4.8 display the decision boundaries created by the MCCM- and SSVR2-based networks for the Fairbanks array. Unknown regions in the SSVR2-based networks are smaller than those in the MCCM-based networks.

Prof. Charles R. Wilson, who is considered to be an expert in the study of MAWs and HTVs, selected seven days of high MAW activity and six days of high HTV activity using the 2008 Fairbanks data. These data sets were never used for training or validating our neural networks. The two trained networks were tested against the expert analysis, and the comparisons were presented in graphical forms using the modified detection summary plots (refer to Figs. 5.1-5.13). The MAWs and HTVs identified by trained networks closely resemble those identified by the expert. This allows us to conclude that it is possible to automate our classification problem at the expert level using our trained networks. These networks have several advantages over the human operator: first, they are robust; second, they are resistant to human errors; finally, they produce consistently unbiased results. By introducing the neural network as a signal classifier, the expert can devote more time focusing on the detailed analysis of the MAWs and HTVs.

6.2 Future Directions

We have shown the correlation between the changes in magnetic (or auroral) activity and the HTVs observed at the Fairbanks array. One can do the same for the Antarctic array since we now have an operating station that measures magnetic activity near the location of our Antarctic array.

In this dissertation, we used a perceptron network to classify three linearly separable low-frequency signals. These signals are linearly separable in the computed parameters'

space (or features). We can expand the number of signals we want classify (e.g., include high-frequency signals and microbaroms) or increase the dimension of our feature space to improve the distinguishability of these signals. As a result, we may require much more complicated neural networks capable of non-linear classification. For instance, persistence of the azimuth can be added to the feature space in order to improve the distinguishability of the MAWs and HTVs. The neural network outputs depend on our parameter estimation, and we have shown that the uncertainty of V_t increases, as V_t and σ_τ increase (refer to Figs. 1.6 and 1.7). As a result, it is possible for the trained networks to classify the MAWs and HTVs incorrectly due to errors in our parameter estimation. This misclassification would form the basis for another ROC study.

Finally, we ignored the effect of coincidence detections on our parameters' estimation. The effect on the parameter estimation and likelihood of such events may be significant. If so, we may be to develop a variable that measures the coincidence detection and incorporate into our feature space. The performance of neural networks may improve, as we increase the size of features and the complexity of the neural networks.

Bibliography

- [1] "Preparatory Commission for the Comprehensive Nuclear-Test-Ban Treaty Organization (CTBTO) 2008, Vienna, Austria, accessed on 8 August 2010", <<http://www.ctbto.org>>.
- [2] A. L. Pichon, E. Blanc, and A. Hauchecorne, eds., *Infrasound Monitoring for Atmospheric Studies*, chapter 2, 1st edition (Springer, London, New York, 2010).
- [3] A. L. Pichon, E. Blanc, and A. Hauchecorne, eds., *Infrasound Monitoring for Atmospheric Studies*, chapter 3, 1st edition (Springer, London, New York, 2010).
- [4] "Infrasound Research Group, Fairbanks, Alaska, USA, accessed on 8 August 2010", <<http://www.gi.alaska.edu/infrasound>>.
- [5] A. L. Pichon, E. Blanc, and A. Hauchecorne, eds., *Infrasound Monitoring for Atmospheric Studies*, chapter 6, 1st edition (Springer, London, New York, 2010).
- [6] A. L. Pichon, E. Blanc, and A. Hauchecorne, eds., *Infrasound Monitoring for Atmospheric Studies*, chapter 1, 1st edition (Springer, London, New York, 2010).
- [7] R. E. Berg and D. G. Stork, *The Physics of Sound*, 3rd edition (Prentice Hall, Englewood Cliffs, NJ, 1982).
- [8] A. D. Pierce, *Acoustics: An Introduction to Its Physical Principles and Applications* (J. Acoust. Soc. Am., Melville, New York, 1989).
- [9] A. P. Dowling and J. E. F. Williams, *Sound and Sources of Sound* (Ellis Horwood, Chichester, New York, 1983).
- [10] E. M. Salomons, *Computational Atmospheric Acoustics*, 1st edition (Springer, London, New York, 2001).
- [11] R. N. Bracewell, *The Fourier Transform and Its Applications*, 3rd edition (McGraw-Hill, Boston, MA, 2000).

- [12] D. H. Johnson and D. E. Dudgeon, *Array Signal Processing: Concepts and Techniques* (Prentice Hall, Englewood Cliffs, NJ, 1993).
- [13] A. E. Gill, *Atmosphere-Ocean Dynamics*, volume 30 (Academic Press, New York, 1982).
- [14] "University of Wyoming, Department of Atmospheric Science, Upperair Air Data, Wyoming, USA, accessed on 10 February 2008", <<http://weather.uwyo.edu/upperair/sounding.html>>.
- [15] "GODDARD SPACE FLIGHT CENTER, Space Physics Data Facility, Atmosphere Models, Greenbelt, Maryland, USA, accessed on 15 March 2008", <<http://modelweb.gsfc.nasa.gov/atmos/msise.html>>.
- [16] J. W. Reed, "Attenuation of blast waves by the atmosphere", *J. Geophys. Res.* **77**, 1616–1622 (1972).
- [17] "International Organization for Standardization (ISO) 2010, Geneva 20, Switzerland, accessed on 1 August 2010", <<http://www.iso.org/iso/home.html>>.
- [18] A. L. Pichon, E. Blanc, and A. Hauchecorne, eds., *Infrasound Monitoring for Atmospheric Studies*, chapter 5, 1st edition (Springer, London, New York, 2010).
- [19] T. M. Georges and W. H. Beasley, "Refraction of infrasound by upper-atmospheric winds", *J. Acoust. Soc. Am.* **61**, 28–34 (1977).
- [20] W. G. Elford, "A study of winds between 80 and 100 km in medium latitudes", *Planet. Space Sci.* **1**, 94–101 (1959).
- [21] V. H. George, J. M. Young, and R. K. Cook, "Infrasound observations of the may 16, 1963, volcanic explosion on the island of bali", *J. Geophys. Res.* **70**, 6017–6022 (1965).
- [22] D. P. Drob, J. M. Picone, and M. Garces, "Global morphology of infrasound propagation", *J. Geophys. Res.* **108** (D21) (2003).

- [23] D. P. Drob, "Atmospheric specifications for infrasound calculations", *Inframatics* 5, 6–13 (2004).
- [24] A. L. Pichon, E. Blanc, and A. Hauchecorne, eds., *Infrasound Monitoring for Atmospheric Studies*, chapter 17, 1st edition (Springer, London, New York, 2010).
- [25] L. E. Kinsler, A. R. Frey, A. B. Coppens, and J. V. Sanders, *Fundamentals of Acoustics*, 4th edition (Wiley, New York, 2000).
- [26] "Chaparral Physics, A Division of the Geophysical Institute of the University of Alaska, Fairbanks, Alaska, USA, accessed on 2 August 2010", <<http://www.gi.alaska.edu/chaparral/InfrasoundPS.html>>.
- [27] B. Alcoverro, P. Martysevich, and Y. Starovoit, "Mechanical sensitivity of microbarometers mb2000 (dase, france) and chaparral5(usa) to vertical and horizontal ground motion", *Inframatics* 9 (2005).
- [28] G. H. Dunteman, *Principal Components Analysis* (Sage Publications, Newbury Park, CA, 1989).
- [29] M. H. Hayes, *Statistical Digital Signal Processing and Modelling* (Wiley, New York, 1996).
- [30] P. J. Brockwell and R. A. Davis, *Introduction to Time Series and Forecasting*, 2nd edition (Springer, New York, 2002).
- [31] J. V. Olson and C. A. L. Szuberla, "The least squares estimation of the azimuth and velocity of plane waves", *Inframatics* 6, 8–12 (2004).
- [32] P. M. Dirac, *The principles of Quantum Mechanics*, 4th edition (Oxford University Press, Clarendon, Oxford, 1982).
- [33] C. R. Rao, *Linear Statistical Inference and Its Applications*, 2nd edition (Wiley, New York, 2001).

- [34] S. M. Kay, *Fundamentals of Statistical Signal Processing: Estimation Theory*, 1st edition (Prentice Hall, Upper Saddle River, NJ, 1993).
- [35] C. A. L. Szuberla and J. V. Olson, "Uncertainties associated with parameter estimation in atmospheric infrasound arrays", *J. Acoust. Soc. Am.* **115**, 253–258 (2004).
- [36] W. H. Press, S. A. Teukolsky, and W. T. V. B. P. Flannery, *Numerical Recipes in C: The Art of Scientific Computing*, 2nd edition (Cambridge University Press, New York, 1992).
- [37] C. R. Wilson, "Infrasound waves from moving auroral electrojets", *Planet. and Space Sci.* **17**, 1107–1120 (1969).
- [38] C. R. Wilson, "Auroral infrasound waves", *J. Geophys. Res.* **74**, 1812–1836 (1969).
- [39] C. R. Wilson, "Infrasound from auroral electrojet motions at i53us", *Inframatics* **10**, 1–13 (2005).
- [40] M. G. Kivelson and C. T. Russell, *Introduction to Space Physics*, 1st edition (Cambridge University Press, New York, 1995).
- [41] C. R. Wilson, "Auroral infrasound at fairbanks, alaska as observed at ctbt infrasound array i53us", *Inframatics* **2**, 10–18 (2003).
- [42] C. R. Wilson and J. V. Olson, "Frequency domain coherence between high trace-velocity infrasound signals at i53us and video data from pulsating aurora", *Inframatics* **9**, 27–30 (2005).
- [43] "College International Geophysical Observatory (CIGO) 2002, Fairbanks, Alaska, USA, accessed on 20 February 2008", <<http://www.gi.alaska.edu/admin/operations/CIGO/CIGO.html>>.
- [44] C. R. Wilson and J. V. Olson, "Mountain associated waves at i53us and i55us in alaska and antarctica in the frequency passband from 0.015 to 0.10 hz", *Inframatics* **3**, 6–10 (2003).

- [45] K. M. A. Jr., C. R. Wilson, J. V. Olson, and C. A. L. Szuberla, "Infrasound associated with mt. stellar avalanche", *Inframatics* **12**, 4–7 (2005).
- [46] S. J. Arrowsmith, D. P. Drob, M. A. H. Hedlin, and W. Edwards, "A joint seismic and acoustic study of the washington state bolide: Observations and modeling", *J. Geophys. Res.* **112**,D09304 (2007).
- [47] T. M. Georges, "Infrasound from convective storms: Examining the evidence", *Rev. Geophys.* **11**, 571–594 (1973).
- [48] A. L. Pichon, E. Blanc, and A. Hauchecorne, eds., *Infrasound Monitoring for Atmospheric Studies*, chapter 16, 1st edition (Springer, London, New York, 2010).
- [49] R. W. Ramirez, *the FFT: Fundamentals and Concepts* (Prentice Hall, Upper Saddle River, NJ, 1984).
- [50] A. V. Oppenheim, R. W. Schaffer, and J. R. Buck, *Discrete-Time Signal Processing*, 2nd edition (Prentice Hall, Upper Saddle River, NJ, 1999).
- [51] G. M. Jenkins and D. G. Watts, *Spectral Analysis and its Applications* (Emerson-Adams Press, Boca Raton, FL, 1998).
- [52] P. Stoica and R. L. Moses, *Introduction to Spectral Analysis* (Prentice Hall, Upper Saddle River, NJ, 1997).
- [53] The MathWorksTM, 3 Apple Hill Dr., Natick, MA, *Signal Processing ToolboxTM: User's Guide*, <<http://www.mathworks.com>>.
- [54] A. L. Pichon, E. Blanc, and A. Hauchecorne, eds., *Infrasound Monitoring for Atmospheric Studies*, chapter 7, 1st edition (Springer, London, New York, 2010).
- [55] A. L. Pichon, E. Blanc, and A. Hauchecorne, eds., *Infrasound Monitoring for Atmospheric Studies*, chapter 8, 1st edition (Springer, London, New York, 2010).

- [56] J. V. Olson and C. A. L. Szuberla, "Distribution of wave packet sizes in microbarom wave trains observed in alaska", *J. Acoust. Soc. Am.* **117**, 1032–1037 (2005).
- [57] A. L. Pichon, E. Blanc, and A. Hauchecorne, eds., *Infrasound Monitoring for Atmospheric Studies*, chapter 23, 1st edition (Springer, London, New York, 2010).
- [58] C. R. Wilson, "Infrasound observed at i53us from large alaskan earthquakes in 2002", *Inframatics* **3**, 11–14 (2003).
- [59] A. L. Pichon, P. Henry, P. Mialle, J. Vergoz, N. Brachet, M. Garces, D. Drob, and L. Ceranna, "Infrasound associated with 2004-2005 large sumatra earthquakes and tsunami", *Geophys. Res. Lett.* **32**, L19802 (2005).
- [60] A. L. Pichon, E. Blanc, and A. Hauchecorne, eds., *Infrasound Monitoring for Atmospheric Studies*, chapter 10, 1st edition (Springer, London, New York, 2010).
- [61] C. R. Wilson, J. V. Olson, D. L. Osborne, and A. L. Pichon, "Infrasound from erebus volcano at i55us in antarctica", *Inframatics* **4**, 1–8 (2003).
- [62] C. R. Wilson and J. V. Olson, "I53us and i55us signals from manam volcano", *Inframatics* **9**, 31–35 (2005).
- [63] C. R. Wilson, J. V. Olson, C. A. L. Szuberla, S. McNutt, G. Tytgat, and D. P. Drob, "Infrasound array observations at i53us of the 2006 augustine volcano eruptions", *Inframatics* **13**, 11–25 (2006).
- [64] A. L. Pichon, E. Blanc, and A. Hauchecorne, eds., *Infrasound Monitoring for Atmospheric Studies*, chapter 13, 1st edition (Springer, London, New York, 2010).
- [65] A. L. Pichon, E. Blanc, and A. Hauchecorne, eds., *Infrasound Monitoring for Atmospheric Studies*, chapter 12, 1st edition (Springer, London, New York, 2010).
- [66] S. M. Kay, *Fundamentals of Statistical Signal Processing: Detection Theory*, 1st edition (Prentice Hall, Upper Saddle River, NJ, 1998).

- [67] J. V. Olson, "Infrasound signal detection using the fisher f-statistic", *Inframatics* **6**, 1–7 (2004).
- [68] S. Haykin, *Neural Networks: A Comprehensive Foundation*, 2nd edition (Prentice Hall, Upper Saddle River, NJ, 1998).
- [69] F.-L. Luo and R. Unbehauen, *Applied Neural Networks For Signal Processing* (Cambridge University Press, New York, 1999).
- [70] F. M. Ham and I. Kostanic, *Principles of Neurocomputing for Science and Engineering* (McGraw-Hill, Boston, MA, 2001).
- [71] F. M. Ham, T. A. Leeney, H. M. Candy, and J. C. Wheeler, "An infrasonic event neural network classifier", volume 6, 3768–3773 (Neural Networks, 1999. IJCNN '99 International Joint).
- [72] C. H. Chen, ed., *Signal and Image Processing for Remote Sensing*, chapter 3, 1st edition (CRC Press, 2006).
- [73] T. Masters, *Signal and Image Processing with Neural Networks: A C++ Sourcebook* (Wiley, New York, 1994).
- [74] W. S. McCulloch and W. Pitts, "A logical calculus of the ideas immanent in nervous activity", *Bull. Math. Biophys.* **5**, 115–133 (1943).
- [75] F. Rosenblatt, "The perceptron: A probabilistic model for information storage and organization in the brain", *Psychol. Rev.* **65**, 386–408 (1958).
- [76] F. Rosenblatt, *Principles of Neurodynamics: Perceptrons and the Theory of Brain Mechanisms* (Spartan Books, 1962).
- [77] M. L. Minsky and S. A. Papert, *Perceptrons*, 1st edition (MIT Press, Cambridge, MA, 1969).

- [78] S. Barber, "Neural Networks, AI: Neural Network for beginners (Part 1 of 3), accessed on 2 August 2010", <<http://www.codeproject.com/KB/recipes>>.
- [79] H. Abdi, D. Valentin, and B. Edelman, eds., *Neural Networks*, 1st edition (Sage Publications, 1998).
- [80] H. Demuth, M. Beale, and M. Hagan, *Neural Network ToolboxTM 6: User's Guide*, The MathWorksTM, 3 Apple Hill Dr., Natick, MA.